2012-09-06

Development of Novel Garnet-Type Solid Electrolytes for Potential Application in Li Ion Batteries

Narayanan, Sumaletha

UNIVERSITY OF CALGARY

Development of Novel Garnet-Type Solid Electrolytes for Potential Application in Li Ion Batteries

by

Sumaletha Narayanan

A THESIS

SUBMITTED TO THE FACULTY OF GRADUATE STUDIES

IN PARTIAL FULFILMENT OF THE REQUIREMENTS FOR THE

DEGREE OF MASTER OF SCIENCE

DEPARTMENT OF CHEMISTRY

CALGARY, ALBERTA

AUGUST, 2012

The undersigned certify that they have read, and recommend to the Faculty of Graduate Studies, The University of Calgary, for acceptance the thesis entitled, "Development of Novel Garnet-Type Solid Electrolytes for Potential Application in Li Ion Batteries" submitted by Sumaletha Narayanan in partial fulfillment of the requirements for the degree of Master of Science.

Supervisor, Dr. Venkataraman Thangadurai, Department of Chemistry

---

Dr. Todd Sutherland, Department of Chemistry

Dr. Yujun Shi, Department of Chemistry

External Examiner, Dr. Christopher Clarkson, Department of Geoscience

---

Date

Abstract

The development of promising solid electrolytes having a garnet-like structure has been successfully achieved through solid state (ceramic) method. Various approaches to improve the Li ion conductivity were employed. The first approach involved creating oxide ion vacancies into the crystal structure of parent garnet-like oxide, $Li_5La_3Nb_2O_{12}$ to create a novel family of compounds with nominal composition, $Li_5La_3Nb_{2-x}Y_xO_{12-\delta}$ ($0 \leq x \leq 1$). The second approach was Li stuffing into the garnet-like oxides to develop a series of Li stuffed novel $Li_{5+2x}La_3Nb_{2-x}Y_xO_{12}$ ($0.05 \leq x \leq 0.75$) and $Li_{6.5}La_{2.5}Ba_{0.5}ZrTaO_{12}$.

Powder X-ray diffraction (PXRD), thermo gravimetric analysis (TGA), scanning electron microscopy (SEM), electron probe microanalysis (EPMA) coupled with a wavelength-dispersive spectrometer (WDS), ^{7}Li nuclear magnetic resonance (Li-NMR), and AC impedance spectroscopy were employed to characterize the structure, morphology, elemental composition, Li ion sites, and Li ion conductivity. Studies have shown that $Li_{5+2x}La_3Nb_{2-x}Y_xO_{12}$ have turned out to be promising solid electrolytes with high Li ion conductivity (10^{-4} Scm^{-1} at ambient temperatures). In addition, all families of garnets are found to be chemically stable with Li cathode materials ($Li_2MMn_3O_8$, where M = Fe, Co) up to 400 ^oC in air. The developed electrolyte materials have the potential to be used in all-solid-state Li ion batteries.

Acknowledgements

First, I would like to express my sincere thanks to Dr. Venkataraman Thangadurai, my research supervisor, for his invaluable support and constant encouragement. This work would not have been possible without his compassion. Dr. Thangadurai has been a supporting mentor throughout my career at University of Calgary. I am thankful to Dr. Todd Sutherland, for all his support in accessing the FTIR instrument and data analysis. I would also like to express my thanks to Dr. Yujun Shi and "internal" external, Dr. Christopher Clarkson. I am indebted to all the moral support and encouragement provided by Dr. Viola Birss, especially during my initial days at Calgary.

I would like to extend my gratitude to Dr. Farshid Ramezanipour for all his contributions to my work. All the collaborative work with Dr. Martin Wilkening, and Viktor Epp from Graz University of Technology, Austria is gratefully acknowledged.

I specially thank Lina Truong and James Colter for their effort in reading my thesis. My appreciation also goes to all my friends in both Dr. Thangadurai's and Dr. Birss' groups, and other friends I cherish my days in school. I also extend my gratitude to the present and past members in both groups for all their help.

I gratefully acknowledge Mark Toonen (glass shop), Mike and Keith (electronic shop), Robert Marr (Department of Geoscience, EPMA technique) for all their help. I would like to thank Bonnie, Jan, and other staffs in the Chemistry office for all their administrative support throughout my career.

Finally, I express my deep sense of gratitude to my family for all their constant love, encouragement, and motivation to overcome any difficult situations.

Table of Contents

List of Tables

List of Figures and Illustrations

List of Symbols

Symbol	Value	Unit	Description
$V_o^{\bullet\bullet}$			Oxygen ion vacancy
δ			Oxygen ion vacancy
ρ		Ohm cm	Resistivity
σ		S cm^{-1}	Conductivity
R	8.314	J K^{-1} mol^{-1}	Gas constant
R		Ohm	Resistance
k	1.38×10^{-23}	J K^{-1}	Boltzmann constant
N_A	6.022×10^{23}	Mol^{-1}	Avogadro's number
χ^2			Goodness of fit
$Z^{/}$		Ohm	Real component of impedance
$Z^{//}$		Ohm	Imaginary component of impedance
Z		Ohm	Impedance
F	9.65×10^4	C mol^{-1}	Faraday constant
E		V	Potential
I		Amp	Current
f		Hz	Frequency
ω		Rads s^{-1}	Radial frequency
θ		Degree	Phase angle
C		F	Capacitance
E_a		eV	Activation energy
V_{oc}		V	Open circuit voltage
l		cm	Length
A		cm^2	Area
Q			Constant phase element

List of Abbreviations

AC	Alternating current
CNT	Carbon nanotubes
CPE	Constant phase element
DC	Direct current
EC	Ethylene carbonate
EIS	Electrochemical impedance spectroscopy
EPMA	Electron probe microanalysis
FTIR	Fourier transform infrared spectroscopy
JCPDS	Joint committee on powder diffraction standards
LIB	Lithium ion battery
LLT	Lithium lanthanum titanate
LLTF	Lithium lanthanum titanate/fluoride
LLTO	Lithium lanthanum titanate
LTP	Lithium titanium phosphate
MAS	Magic angle spinning
NASICON	Sodium super ionic conductors
NMR	Nuclear magnetic resonance
PC	Propylene carbonate
PEO	Ploy ethylene oxide
PXRD	Powder X-ray diffraction
SEM	Scanning electron microscopy
TGA	Thermo gravimetric analysis
VTNMR	Variable temperature NMR
WDS	Wavelength dispersive spectrometer

Chapter One: **Introduction**

1.1 Background

Increase in population, global warming, and depletion of fossil fuels are the driving forces to seek alternative renewable energy sources to meet the ever-ending energy thirst of today's society. A sustainable energy system can ensure a continuous supply of energy for the rising needs. This in turn increases the importance of research on finding environmentally benign alternative energy production and storage devices. Electrochemical devices such as batteries and fuel cells are considered as better candidates for high energy systems.

Lithium ion batteries (LIBs) are attaining significant attention for various applications ranging from portable electronics to electric vehicles because of their high energy density. They are widely considered as storage devices for renewable energy systems. Despite their promising applications, LIBs suffer from a few disadvantages mainly due to the currently employed liquid electrolyte. Even though the liquid electrolytes provide high ionic conductivity and high contact area with the electrodes, they raise a few safety issues. These include high flammability, leakage problem, explosion and rapid self-discharge. In order to overcome the limitations associated with current liquid electrolyte, it must be replaced with a safe solid-state electrolyte.

Solid-state electrolytes possess a number of advantages over liquid electrolytes such as high physical and chemical stability, non-flammability, low self-discharge, and high energy density. The comparatively lower ionic conductivity of solid electrolytes is an issue faced by LIB researchers. The aim of this thesis is to develop new solid-state

electrolytes with promising Li ion conductivity, which can be used for all-solid-state battery fabrication.

1.2 Research objectives

The main objective of this thesis was to synthesize new solid-state electrolytes having garnet-like structure and understand the Li ion conduction mechanism using AC impedance and physical spectroscopy methods such as Li NMR. Two approaches were made to increase the Li ion conductivity of the materials. The first approach was creating oxide ion vacancies while keeping the Li concentration constant and the second approach was Li-stuffing into the garnet-structure.

Another objective was to understand the change in Li ion conductivity of garnet-like compounds with temperature and also to study their chemical compatibility with temperature, water and various electrode components. An attempt to understand the conduction mechanism was also carried out by employing the solid-state ^{6}Li and ^{7}Li MAS NMR (magic angle spinning nuclear magnetic resonance) spectroscopy.

1.3 Thesis organization

This thesis is organized into seven chapters. Chapter 1 deals with the importance, motivation, and overview of this thesis work. In addition to the background information on LIBs and the materials used for their application, experimental techniques used throughout this research is also covered in Chapter 2. The specific descriptions of experimental procedures and characterization methods used are explained in Chapter 3. Three result chapters (Chapters 4-6) are included in this thesis. All these chapters include

a general overview, results and discussion, and conclusion sections. All relevant references for each chapter are listed at the end of this thesis.

Chapter 4 results are published in the peer-reviewed journals: (i) Narayanan, S.; Thangadurai, V. “Effect of Y substitution for Nb in $Li_5La_3Nb_2O_{12}$ on Li ion conductivity of garnet-type solid electrolytes” J. Power Sources **2011**, *196*, 8085-8090, and (ii) Narayanan, S.; Thangadurai, V. "Fast lithium ion conducting garnet-like electrolytes for potential application in lithium ion batteries" *ECS Trans.* **2011**, *35* (32), 125-131. This chapter studies the effect of Y-doping onto the parent garnet-like $Li_5La_3Nb_2O_{12}$ creating oxide ion vacancies in the crystal structure. AC impedance spectroscopy and scanning electron microscopy were used to study the oxide ion effect on Li ion conductivity, and morphology. The chemical compatibility with high-voltage cathode materials was also studied. Chapter 5 (a part of this work has been submitted to J. Phys. Chem. C) provides a detailed analysis of the new class of garnet-like electrolytes having nominal composition, $Li_{5+2x}La_3Nb_{2-x}Y_xO_{12}$ ($0.05 \leq x \leq 0.75$) using AC impedance spectroscopy, *in-situ* powder X-ray diffraction (PXRD) studies, and electron probe microscopic techniques.

Chapter 6 is an extensive study of the transport properties of a promising garnet-like solid electrolyte, $Li_{6.5}La_{2.5}Ba_{0.5}ZrTaO_{12}$. Both macroscopic and microscopic analysis was carried out using AC impedance, and NMR spectroscopy. A part of this work has already been published in RSC Advances (Narayanan, S.; Epp, V.; Wilkening, M.; Thangadurai, V. “Macroscopic and microscopic Li^+ transport parameters in cubic garnet-type $Li_{6.5}La_{2.5}Ba_{0.5}ZrTaO_{12}$ as probed by impedance spectroscopy and NMR” *RSC Adv.* **2012**, *2*, 2553-2561). This work is reproduced by permission of The Royal Society of

Chemistry and the link to the paper on the Royal Society of Chemistry's website is http://pubs.rsc.org/en/content/articlelanding/2012/ra/c2ra01042a. Finally, Chapter 7 summarizes the conclusions for each result chapter (Chapters 4-6) and future directions on this research.

Chapter Two: **Background and experimental techniques**

2.1 Introduction

Rechargeable lithium-ion batteries (LIBs) are being considered as powerful energy storage systems for fulfillment of the energy needs of today's world[1-8]. Compared to lead-acid, nickel-cadmium and nickel-metal hydride batteries, commercially available lithium-ion batteries are characterized by a much higher volumetric and gravimetric energy density of 650 Whl^{-1} and 150 $Whkg^{-1}$, respectively[1-4]. Therefore, Li-ion cells are becoming increasingly popular for use in various portable electronic devices. In addition, secondary Li-ion batteries are being considered for use in hybrid electric vehicles, in combination with an internal combustion engine[1-6]. Motivation for development of this technology is driven by the rapid depletion of fossil fuels and growing environmental concerns. The realization of electric powered vehicles undoubtedly requires the development and precise investigation of new clean energy storage materials. These materials are necessary to further improve the storage capacity, safety, and rate (power) capability of Li-ion batteries, which are the most promising energy storage systems in the medium run.

2.2 Li-ion batteries

Batteries are electrochemical energy conversion devices which convert chemical energy into electrical energy via electrochemical redox reactions. The key components of a battery include the electrolyte (ionic conductor), anode (negative electrode), and

cathode (positive electrode). In general, batteries can be classified into two groups: (i) primary (non-rechargeable) and (ii) secondary (rechargeable) batteries. Rechargeable lithium-ion batteries have been commercialized by Sony Corporation in 1991[9]. The evaluation of LIBs is done based on their energy density ($Whkg^{-1}$or Whl^{-1}) and power density (Wkg^{-1} or Wl^{-1}). A comparison of energy storage capacities for different commercial batteries is shown in Figure 2.1[8]. Both the weight and size decreases with increase in gravimetric and volumetric energy density, respectively. LIBs are light weight and provide high working voltage (~ 3.6 V), and have longer charge retention (> 5 years)[10].

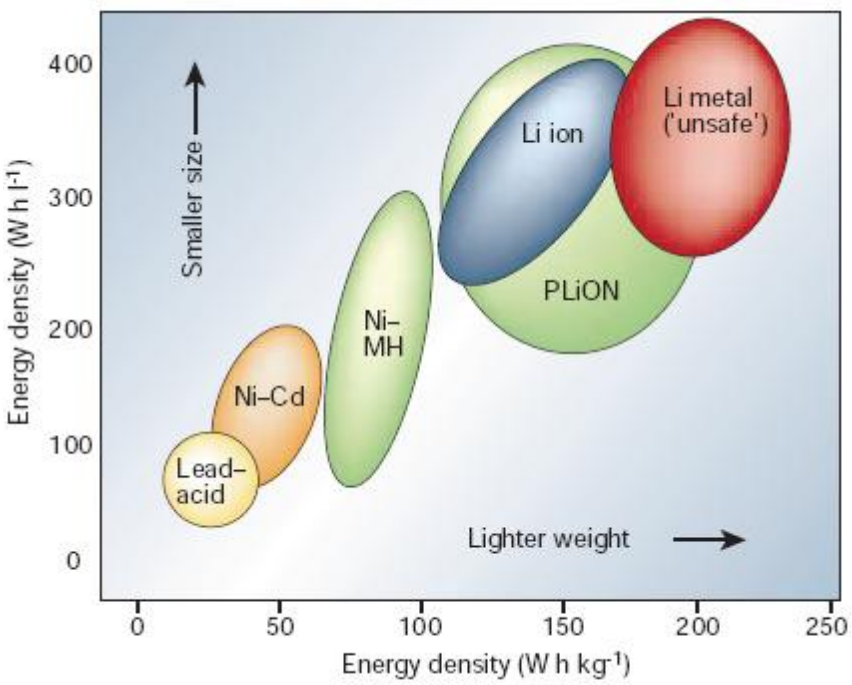

Figure 2. 1 Gravimetric and volumetric energy densities of different commercial batteries[1].

The open circuit voltage (V_{oc}) of a LIB can be calculated as the difference in chemical potential between the electrodes as shown in equation [2.1][11].

$$V_{oc} = \frac{\mu_{Li(c)} - \mu_{Li(a)}}{F} \qquad [2.1]$$

Where $\mu_{Li(c)}$ is the chemical potential at cathode, $\mu_{Li(a)}$ is the chemical potential at anode, and F is Faraday's constant (96485 $Cmol^{-1}$).

The three main functional components of current LIBs include $LiPF_6$ dissolved in organic solvents as the commonly used electrolyte, $LiCoO_2$ as a positive electrode, and generally graphitic carbon or any other intercalation compounds as a negative electrode[12]. Both these electrodes are supported on current collectors. During charging and discharging, lithium ions move back and forth between the electrodes and hence, LIBs are known as 'rocking-chair' batteries. In the charge-discharge process, Li ions are intercalated (inserted) or de-intercalated (extracted) from the interstitial space in the atomic layers within the electrode components. The schematic representation of a Li ion cell indicating the electrochemical processes during charging and discharging is provided in Figure 2.2. Equations [2.2]-[2.4] represent the corresponding electrochemical reactions at the cathode, anode, and overall reaction, respectively[13].

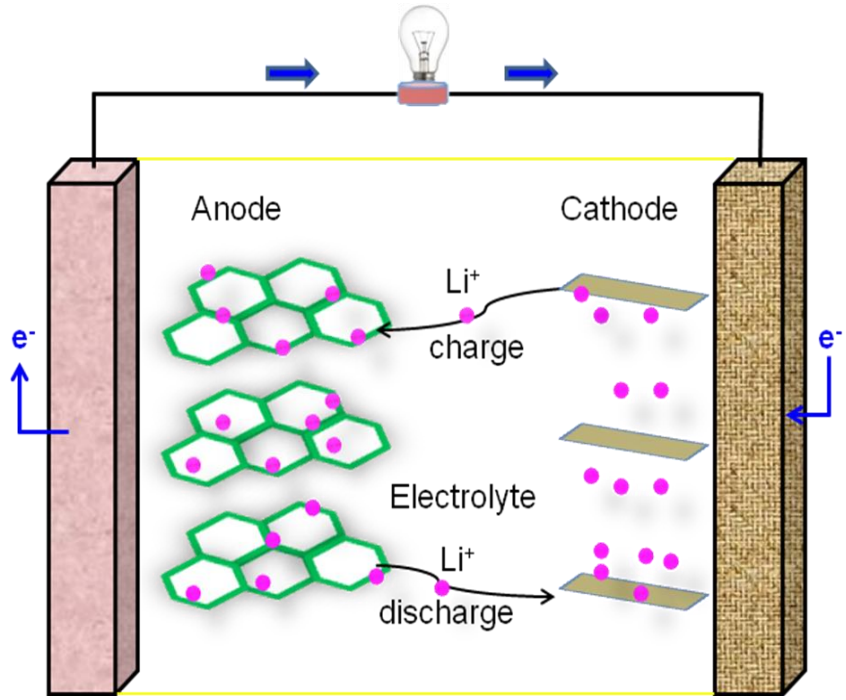

Figure 2. 2 Schematic representation of charge and discharge process of a Li ion battery[13].

Cathode: $$LiCoO_2 \underset{\text{Discharge}}{\overset{\text{Charge}}{\rightleftharpoons}} Li_{1-x}CoO_2 + xLi^+ + xe^{-1} \quad [2.2]$$

Anode: $$C + xLi^+ + xe^{-1} \underset{\text{Discharge}}{\overset{\text{Charge}}{\rightleftharpoons}} Li_xC \quad [2.3]$$

Overall: $$LiCoO_2 + C \underset{\text{Discharge}}{\overset{\text{Charge}}{\rightleftharpoons}} Li_{1-x}CoO_2 + Li_xC \quad [2.4]$$

Current LIBs are perfect match for transportation and energy storage; however, the safety threats are still problematic. The flammable organic solvent based electrolyte possesses poor chemical stability which can cause explosion[14]. As a result, present-day battery research is focussed on finding non-flammable next-generation materials for LIBs, which is the motivation behind this thesis.

2.3 Electrolyte materials for LIBs

An ideal electrolyte material should exhibit mainly ionic conductivity with null electronic conduction, stays inert with both electrode components, and be low in cost. Having significant ionic (Li^+) transport and negligible electron transport for an electrolyte avoids the self–charge and discharge. In the case of liquid and polymer electrolytes, the electron path could be through Li dendrites, but in the case of solid state ceramic electrolytes, Li dendrites do not form, and so the electron paths could be through grain-boundaries, pores, or cracks[11]. The two types of electrolytes used for LIBs can be categorized as liquid electrolytes, and solid electrolytes.

Liquid electrolytes exhibit the highest ionic conductivity of 10^{-2} Scm^{-1} at ambient conditions. Liquid electrolytes are comprised of Li salts such as $LiPF_6$, $LiBF_4$, $LiCF_3SO_3$ and $LiN(CF_3SO_2)_2$, dissolved in organic solvents such as ethylene carbonate (EC) and propylene carbonate (PC). In liquid based LIBs, the dendrite formation on the electrode may result due to continuous cycling and cause electrical short circuits, sparks, and finally, explosion of the battery. Solid polymer electrolytes are used to avoid the problem of leakage and dendrite formation, albeit their ionic conductivity is much lower than that of liquid electrolytes. The use of liquid solvent to improve the conductivity of solid polymers is still problematic.

2.4 Solid Li ion electrolytes

In order to overcome the problems related to liquid/organic electrolytes, solid state electrolytes are being developed for LIBs. The advantages of solid electrolytes over liquid electrolytes are their wide electrochemical window (up to about 6V/Li), high

chemical and physical stability, and long shelf life. The basic requirements for a solid state Li ion conductor for their application in Li-ion batteries include[5,15]:

1) High total lithium ion conductivity (~ 10^{-3} Scm^{-1}) at operating temperatures
2) Negligible electronic conductivity at high (anode) and low (cathode) Li activity
3) High chemical stability with Li electrodes during the long-term operation
4) Thermal expansion coefficient match with Li electrodes
5) High electrochemical decomposition voltage (up to 5.5V vs Li)
6) Low cost, easy transportation, and environmental benignity

The solid electrolytes can be further divided into two classes, namely (i) solid polymer electrolytes, and (ii) ceramic electrolytes.

2.4.1 Solid polymer electrolytes

The high ionic conductivity of Li metal salt based polyethylene oxide (PEO) was first reported by Wright et al. in 1973[16]. Following this discovery, they have been introduced for application as solid state electrolytes by Armand et al. [17,18]. Several lithium salts such as $LiClO_4$ and $LiN(CF_3SO_2)_2$ were used along with these high molecular weight polymers[18]. Solid polymer electrolytes can act as both an electrolyte and separator. They exhibit very poor conductivities in the order of 10^{-8} Scm^{-1} at ambient temperatures[19]. Organic plasticizers are applied into the polymer matrix to improve its ionic conductivity. This again causes safety concerns, mechanical instability, and other drawbacks associated with liquid based electrolytes. Nano material ceramic fillers such as

SiO_2, Al_2O_3, TiO_2, and clays are normally used as mechanical strengthening agents, which are added to the polymer network[20,21].

Carbon nanotubes (CNT) are considered as better mechanical reinforcing agents for polymer matrix because of their excellent aspect ratio and conductivity. This also enhances the Li ion conductivity by providing easy pathways for Li mobility[22,23]. The possible disadvantages of using CNTs are high electronic conductivity and possible short circuiting; however, the use of CNTs and clay together could avoid this problem[24].

2.4.2 Ceramic (inorganic) electrolytes

There are several classes of inorganic materials that can be used as electrolytes. A general picture of solid electrolytes used and their conductivities are shown in Figure 2.3[25]. The problems associated with the current solid electrolytes for functional applications in batteries are summarized in Table 2.1[25-31]. This section covers a few important families of ceramics (metal oxides), including A-site deficient perovskites, sodium super ionic conductors (NASICON)-type, and garnet-like compounds.

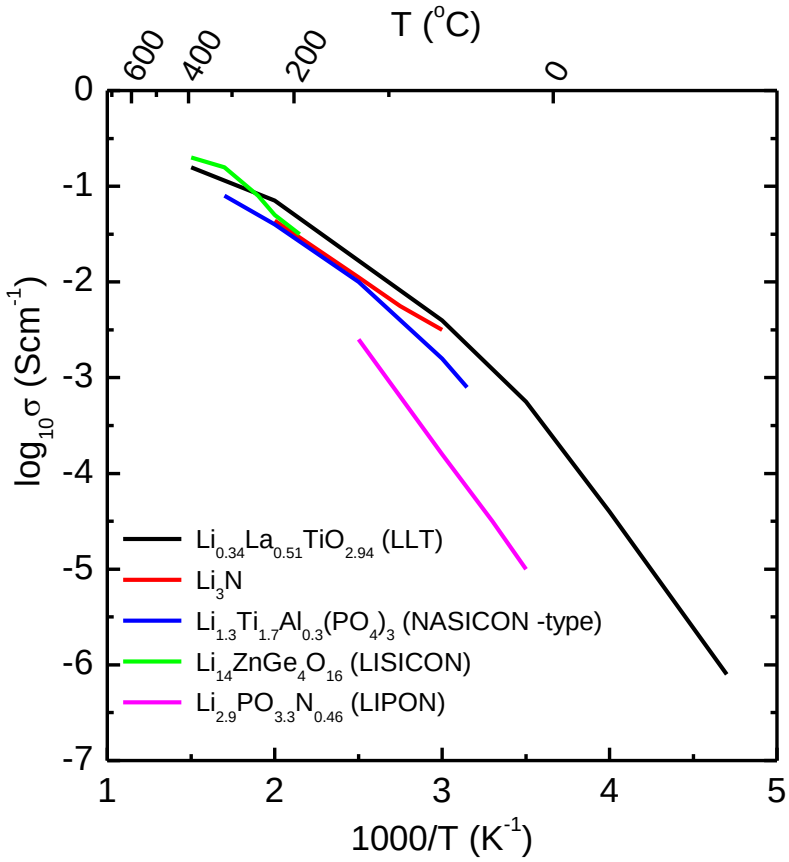

Figure 2. 3 Arrhenius plots of different solid state Li conducting electrolytes[25].

Table 2. 1 Current solid state Li electrolytes and their disadvantages[25-31].

Currently used solid Li electrolyte material	Structure	Problems encountering for the Li ion battery application
Li_3N	2D (layered)	Poor electrochemical stability at room temperature (0.445 V)
$Li_{1.4}ZnGe_4O_{16}$ (LISICON)	3D	Reactive towards Li metal and atmospheric CO_2, and conductivity decreases with time
$Li_{1.3}Ti_{1.7}Al_{0.3}(PO_4)_3$ (NASICON)	3D	Unstable with Li metal
$(Li,La,\square)TiO_3$	3D	Unstable with Li metal, difficult to control the lithium content, and large grain boundary resistance
$Li_{2.88}PO_{3.86}N_{0.14}$ (LiPON)	3D	Moderate conductivity, which varies with sputtering conditions.

2.4.2.1 A-Site deficient perovskite Li-ion electrolytes

The general formula for perovskite is ABO_3, where A, and B are twelve and six-fold coordinated cations, respectively. Figure 2.4 represents the crystal structure of a perovskite, ABO_3 where A and B occupy the A and B site respectively. The A-site deficient perovskite is found to be highly conducting crystalline solid with general formula, $La_{(2/3)-x}Li_{3x}\square_{(1/3)-2x}TiO_3$ ($0<x<0.16$) (LLTO or LLT)[30-32]. A high bulk Li ion conductivity of 10^{-3} Scm^{-1} at ambient temperature was obtained for single crystal LLTO with $x = 0.11$[30-32]. The electronic conductivity of these materials is negligible in air[33]. Li ion dynamics is driven by the A-site vacancy mechanism. The conduction occurs through the square planar bottleneck between A-sites.

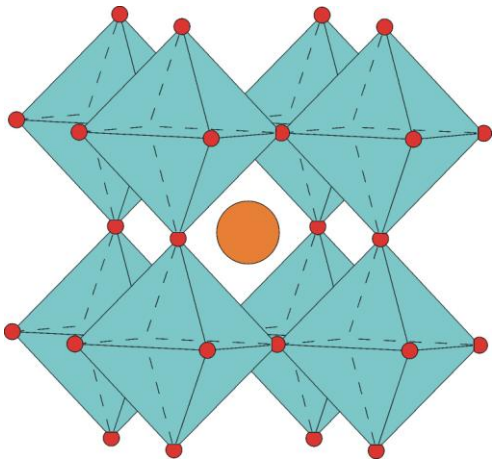

Figure 2. 4 Crystal structure of perovskite, ABO_3. The yellow sphere and blue octahedra, and red spheres represent A-site cation, BO_6 octahedra, and oxygen, respectively.

Several substitution studies have been done at the A-site to improve the conductivity. There are a few cases, where the conductivity has decreased by doping with

rare earth cations, such as Pr, Nd, and Sm (can be denoted as Ln)[34,35]. This is due to the shortening of Ln-O bond length, which in turn narrows the hopping of Li ions through the bottleneck containing four oxygen atoms. Hence, it is very important to control the oxygen position to form the bottleneck to have facile Li hopping. Various studies have been done to understand the degree of ordering in accordance with A-site doping. Disordered arrangement of the A-site cation was found in α-LLT, crystallizing with a space group *P*3*m*3, and whose conductivity was found to be 1.53 x 10^{-3} Scm^{-1} at 25 °C[36]. Whereas the LLT with ordered arrangement of the A-site cation was found in β-LLT, has a space group of *P*4/*mmm*, and shows a conductivity of 6.88 x 10^{-4} Scm^{-1}at 25 °C[37].

The effect of substitution of F^- for O^{2-} on Li ion conductivity was studied by Li et al.[38]. Recent studies by Okumura et al. have shown that addition of LiF during the synthesis of α-LLT further improves the ionic conductivity[39,40]. Li conductivity of 2.30 x 10^{-3} Scm^{-1} at 30 °C was observed for $La_{0.56-y}Li_{0.33}TiO_{3-3y}F_{3y}$ (LLTF) with y = 0.017. Comparative studies have been done by varying the La and F content in α-$La_{0.56-y}Li_{0.33+3y}TiO_3$ and α-$La_{0.56-y}Li_{0.33}TiO_{3-3y}F_{3y}$, respectively, and have found that the perovskites containing F^{-1} show higher conductivity than the non-fluoride member. There are several hardships associated with A-site deficient LLT materials. The requirement of high sintering temperature is a key issue. The volatilization of Li_2O occurs during sample preparation and leads to uncontrolled lithium content in the structure. Moreover, the Ti^{4+} cation undergoes reduction at the Li metal anode interface[41-43].

2.4.2.2 NASICON-type Li-ion electrolytes

The phosphates having NASICON structure are identified as safe, cheap and suitable materials for LIB application. The properties like high ionic conductivity and very good reversible lithium intercalation properties make them suitable for this application. The term NASICON comes from "sodium super ionic conductors", and it has the general formula unit, $[A_2P_3O_{12}]^-$, which consists of AO_6 octahedra and PO_4 tetrahedra, three dimensionally (3D) connected to form two interstitial sites (M1 and M2) which make the conduction pathways[44]. The mobile ions find their path through the bottle neck. The crystal structure of NASICON is shown in Figure 2.5.

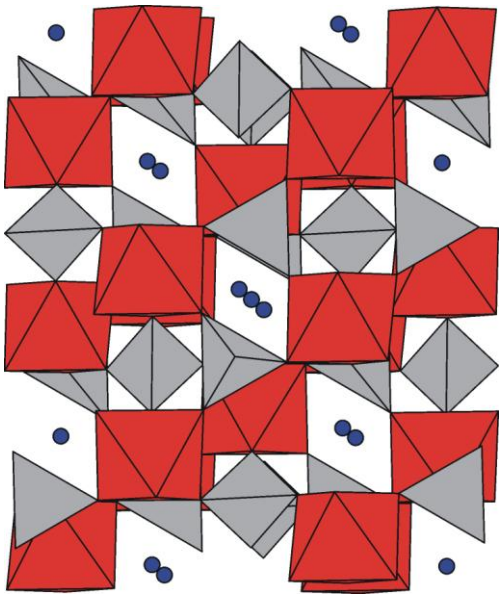

Figure 2. 5 Crystal structure of NASICON. The red octahedra, grey tetrahedra and blue spheres represent AO_6, PO_4, and lithium, respectively.

A site cation can be Ti, Ge or Zr, and several aliovalent substitutions by trivalent cations are possible for Ti^{4+}. It has been observed that substitution by the above mentioned cations and addition of lithium salts such as $LiNO_3$ to $LiTi_2(PO_4)_3$ [LTP] to produce

composite electrolytes has greatly improved the ionic conductivity[45,46]. As resulted ceramics are highly dense materials to reduce the grain-boundary resistance. The possible factors for the enhancement in conductivity are partial melting of LTP during sintering in the presence of lithium salts, crystallization of LTP during melting, and formation of $Li_4P_2O_7$.

The problems associated with the NASICON-type $LiM_2(PO_4)_3$ (M = Ge, Ti, or Hf) include its very low conductivity and poor sinterability, but these problems can be solved by the substitution of M^{4+} with trivalent cations[47]. The compound having stoichiometric formula, $Li_{1.3}Al_{0.3}Ti_{1.7}(PO_4)_3$ has a high conductivity of 3 x 10^{-3} Scm^{-1} at 25 °C[47]. In 2007, Arbi et al. performed a detailed study based on NMR and AC impedance spectroscopy, on $Li_{1+x}Ti_{2-x}M_x(PO_4)_3$ (M=Al, Ga, In, Sc)[48]. The investigation proved that Al^{3+} substitution at the Ti^{4+} site significantly affects the rhombohedral unit cell dimensions and conductivity. Cell parameters were found to decrease, while the conductivity increased by three orders of magnitude. However, possible reduction of Ti^{4+} in the presence of metallic Li is problematic as observed with the A-site deficient LLTO perovskites. Recently, Pinus et al. have studied the effect of aliovalent doping of $LiTi_2(PO_4)_3$ by Nb^{5+} and found an expansion in the cell volume (increase of lattices constants) and elongation of Li1-O bond length[49]. These factors account for the increase in Li ion mobility. Variable temperature ^{7}Li NMR studies on $LiM_2(PO_4)_3$ (M = Ge, Ti, Sn, Zr and Hf) reveal the mechanism of Li ion dynamics in the structure[50-53]. According to this study, below 250 K, Li ions occupy specific sites in the crystal lattice and when the temperature is increased to 400 K, conductivity increases due to phase change from

triclinic to rhombohedral. Above 400 K, conductivity is further increased due to the formation of vacancies at the M1 sites of the rhombohedral phase.

2.4.2.3 Garnet and garnet-like electrolytes

2.4.2.3.1 Structure of garnet and garnet-like oxides

The garnet structure has general formula, $A_3^{II}B_2^{III}(SiO_4)_3$ (where A = Ca, Mg and B = Al, Cr, Fe) and the A, B and Si cations occupy the eight, six, and four coordination sites, respectively[54,55]. Another classic way of writing this is $A_3B_3C_2O_{12}$ where A, B, and C cations occupy at eight, four, and six coordination respectively. All these sites are occupied in conventional garnets. As garnets have various coordinating cations, there are greater options for substitution by alkali, alkaline earth, transition, and rare earth metal cations. The garnet-like oxide with nominal formula, $Li_5La_3M_2O_{12}$ (M = Nb, Ta) is the most recognized solid Li ion electrolyte since its discovery by Thangadurai et al. in 2003[56]. There are two excess Li^+ in the formula unit and various studies had been done to understand positioning of these extra cations. The typical garnet-like structure of $Li_5La_3M_2O_{12}$ is given in Figure 2.6. For the first time, Mazza et al.[57,58] proposed that the space group for $Li_5La_3M_2O_{12}$ is *Ia*-3*d* from the XRD analysis. However, a different space group, $I2_13$ was proposed by Hyooma et al., which has less symmetry[59]. Later on, Cussen et al.[55] confirmed by neutron diffraction studies that the cubic garnet has space group *Ia*-3*d*.

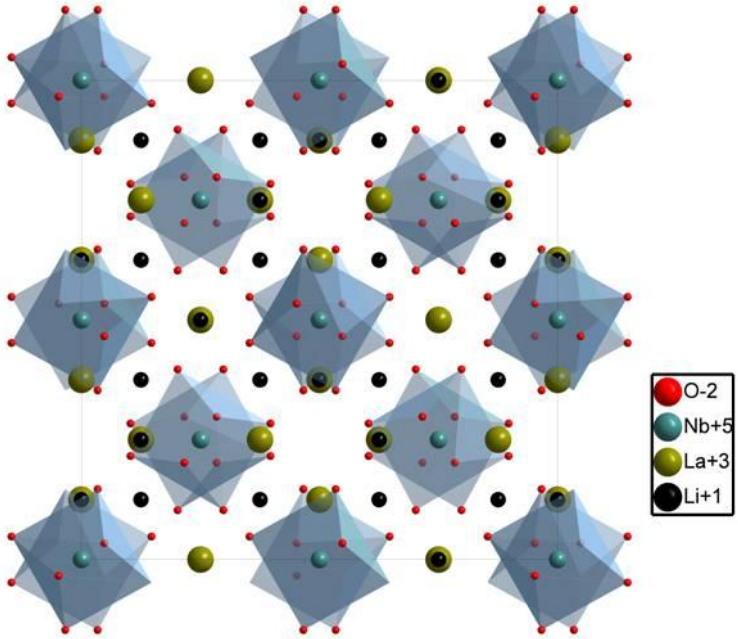

Figure 2. 6 Crystal structure of garnet-like $Li_5La_3M_2O_{12}$. The blue, green, red, and black spheres represent Nb, La, O, and Li ions respectively. The blue octahedra represent the NbO_6 octahedra.

Neutron diffraction analysis revealed that lithium is distributed in both tetrahedral (Td) and distorted octahedral (Oh) sites. The occupancy of lithium is ~ 80 % in the Td site and ~ 40 % in the Oh site in $Li_5La_3M_2O_{12}$. The octahedra containing Li is linked between two tetrahedral through face sharing and the distance between centered Li in two polyhedra is 2 Å. In order to withstand the repulsion between polyhedra, some Li cations in octahedra are displaced with respect to an axis, and in this case Li-Li distance becomes 2.4 Å. The highest conducting ($\sigma = 10^{-4}$ Scm^{-1} at 23 °C) cubic garnet-like $Li_7La_3Zr_2O_{12}$ synthesized by Murugan et al.[60] also crystallized with the same space group *Ia*-3*d*. The lattice parameter (*a*) found was 12.9682(6) Å. In 2009, Awaka et al.[61] synthesized $Li_7La_3Zr_2O_{12}$ with tetragonal morphology with space group $I4_1/acd$ by lower sintering

temperature, which resulted in the decrease in conductivity in the order of two (9 x 10^{-6} Scm^{-1} at 25 °C). The lattice parameters obtained were *a* = 13.134(4) Å and *c* = 12.663(8) Å. Rietveld refinement of X-ray and neutron diffraction studies have shown that the crystal framework consists of dodecahedral $La(1)O_8$, $La(2)O_8$, and octahedral ZrO_6. Three different crystallographic positions were found for Li and Li(1), Li(2), and Li(3) occupied at crystallographic sites at the interstices of this framework structure at tetrahedral 8*a* site, distorted octahedral 16*f*, and 32*g* sites, respectively. In contrast to the cubic structure, all these sites were filled by Li atoms.

Up to now, chemical compositions, crystal structures, and ionic conductivities of many Li-conducting garnets have been investigated in detail by several groups[50,51,60-78]. Following the discovery of garnet structured $Li_5La_3M_2O_{12}$, various research has been attempted to improve ionic conductivity by chemical substitution.

- Substitution at M by different cations like Bi, W, Sb, Te was also done followed by Nb and Ta[70,79-81].
- The complete substitution at the La site in $Li_5Ln_3Sb_2O_{12}$ was done by Slater et al. in 2008, using various rare earth elements, Ln = La, Pr, Nd, Sm, Eu[70]. A reduction in Ln-O distance and contraction of cell volume was obtained for the d^0 analogues compared to the d^{10} analogues.
- Aliovalent substitution of La with alkaline earth metals resulted in the composition, $Li_6ALa_2M_2O_{12}$ (A = Ca, Sr, Ba, Mg) and the Ba substituted Ta member showed high ionic conductivity of 4 x 10^{-5} S cm^{-1} at 22 ^oC[62,64,65,82]. Also, the Ta members were found to be stable against chemical reaction with molten Li, and exhibited a high electrochemical stability window of up to ~ 6 V/ Li.

- The ionic conductivity was found to be increasing with increasing Li content in the garnet. The structural investigation on the composition, $Li_6ALa_2M_2O_{12}$ (M = Sb, Ta) was performed by Cussen et al.[83].
- The partial substitution of La by divalent Ba resulted in the composition $Li_{5+x}Ba_xLa_{3-x}Ta_2O_{12}$ and the effect of substitution on lattice expansion was well studied by Murugan et al.[82]. They have also investigated the effect of lithium and oxygen content on a series of compounds, $Li_{5+x}Ba_xLa_{3-x}Ta_2O_{11.5+0.5x}$ (x = 0-2), and found that the lithium oxide has an effect on increasing the conductivity[84].
- Studies show that there is a correlation between the ionic radius of the substituent on the crystal lattice constant and ionic conductivity[85]. The lattice parameter was found to increase with increasing final sintering temperature for all substitutions except the co-substitution by $Sr_{0.5}Ba_{0.5}$[85]. The very small deviation in this trend could be due to diffusion of impurity or unreacted oxides from the surface to the bulk at high temperatures.
- In 2007, Murugan et al. developed a new garnet, $Li_7La_3Zr_2O_{12}$ by Li stuffing into the structure, which is a cubic polymorph synthesized at high temperature, 1230 °C[60]. It was found to have an extraordinarily high ionic (bulk) conductivity of approximately 10^{-4} Scm^{-1} at 25 °C.
- However, a low temperature synthesis at 980 °C resulted in the formation of tetragonal $Li_7La_3Zr_2O_{12}$, with a space group $I4_1/acd$. The conductivity is two orders of magnitude lower than that of the cubic modification at ambient temperatures[61,86].
- A similar trend of transition in symmetry, from tetragonal to cubic in accordance with temperature, was also found for $Li_7La_3Sn_2O_{12}$[87].

- No attempts were found in the literature to improve the Li ion conductivity by doping Y^{3+} for Nb^{5+} in the parent $Li_5La_3Nb_2O_{12}$.

However, less is known about the details of the conduction mechanisms of Li-containing oxide garnets. Complementary impedance spectroscopy measurements and NMR studies may help to understand the correlation between crystal structure and Li transport properties. Quite recently, we have used variable-temperature NMR spin-lattice relaxation and conductivity measurements to investigate Li ion dynamics in phase-pure $Li_7La_3Zr_2O_{12}$, crystallizing with tetragonal symmetry[77]. Geiger et al. have also reported detailed NMR studies on the cubic analogue to understand the conduction mechanism[76]. Very interestingly, few peaks due to Al_2O_3 were found in the Al NMR studies, and it can be considered that the presence of small amount of alumina which is coming from the crucibles used for preparation could contribute to the better sinterability and further improvement in the conductivity. A similar trend was found by Kumazaki et al.[89]. They have proved that inclusion of small amounts of Si or Al into the $Li_7La_3Zr_2O_{12}$ significantly reduces the grain boundary resistance.

Few reports on the fabrication of solid state batteries using high conducting garnets are available. The intersection of a thin film of $LiCoO_2$ on $Li_7La_3Zr_2O_{12}$ pellet was studied recently and transmission electron microscopic studies showed the Li insertion and extraction at the interface; however, they found poor electrochemical performance for this combination[71]. Ohta et al. have investigated an all-solid-state Li-ion battery consisting of $LiCoO_2$ (cathode), $Li_{6.75}La_3Zr_{1.75}Nb_{0.25}O_{12}$ (solid electrolyte), and lithium (anode). They had proved that the battery has favorable charge-discharge behavior and exhibits good stable cycle performance up to 100 cycles[90].

2.5 Li ion battery electrodes

2.5.1 Li cathodes

There are several characteristics that are needed for an insertion material to act as a cathode for LIBs. It should possess high chemical potential with respect to lithium ($\mu_{Li(c)}$) in order to maximize the V_{oc}. High lithium insertion/desertion with minimal change in the structure is preferred, in addition to high electrochemical stability and chemical stability with the electrolyte. Moreover, the cathode should possess high electronic and Li ion conductivity to ensure high current and power density. Electrochemical potential windows for several Li intercalation compounds are shown in Figure 2.7[12]. The structural classifications of cathodes are spinel and layered structured materials. In most cases, the cathodes are chosen from transition metal oxides that can undergo higher oxidation states when Li is removed from the structure[91,92].

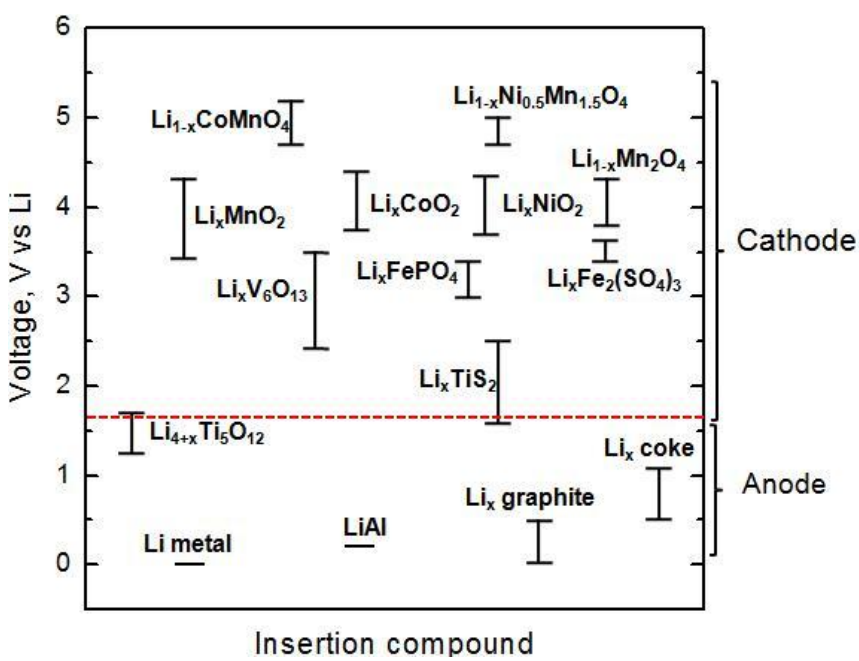

Figure 2. 7 Electrochemical potential of some Li-intercalation compound vs metallic Li[12].

$LiCoO_2$ has a layered structure and its electrochemical cyclability at 4V was reported in 1980. A decade later, it was used for the first commercial Li-ion batteries[93]. Initially, the layered $LiNiO_2$ was considered instead of $LiCoO_2$ due to its high specific capacity, but they are structurally unstable materials which cause exothermic oxidation of the electrolyte, causing safety issue[94]. Even though $LiCoO_2$ is leading the market now as a Li-ion battery cathode, recently several disadvantages have been reported, including the disadvantage of performance degradation on over charging. Co is also less available and expensive[95-97]. Aliovalent substitution for Ni by cations such as Al, Mg, Ti, Mg etc. could solve the structural stability problem[98]. The most commonly used $Li(Ni_{1/3}Mn_{1/3}Co_{1/3})O_2$ shows high capacity, voltage and rate capability etc. and is a promising cathode material[99-100], but is prone to capacity loss during cycling[101].

The spinel structured $LiMnO_2$ is a promising candidate as a cathode and is much cheaper and safer than $LiCoO_2$; however, the structural stability is not very good for these oxides, which undergo phase change during cycling[92,102]. Vanadates are another type of cathode that fulfills the requirement of multiple valence state for a cathode; however, its voltage is very low (~3V), which makes them unsuitable for battery applications[103,104].

A very promising cathode family is $LiMPO_4$ (Fe, Mn, Co) having olivine structure. Among these, the most commonly used cathode is $LiFePO_4$, which has higher capacity compared to other members. $LiFePO_4$ forms $FePO_4$ upon delithiation[105]. The two-phase condition maintains a constant voltage over the discharge cycle. Though the electronic conductivity of these materials is very low around 10^{-9} Scm^{-1}, it can be improved by the addition of conductive phase along with the heat treatment[106].

Research is progressing to find the ideal cathode with high voltage and high capacity, with good structural stability. Mixed oxides like $Li_2CoMn_3O_8$, $Li_2FeMn_3O_8$, $Li[Li,Mn,Ni,Co]O_2$ etc. have been proved as high voltage cathodes (> 5V) showing possibility for further application in Li ion batteries[107-109].

2.5.2 Li anodes

Metallic Li is a high energy dense material; making it worthwhile for use as an anode. In terms of safety and cycle life, metallic Li is a challenge. The requirements for a good anode are higher degree of Li insertion/desertion ability, high electronic and ionic conductivity, strong chemical and structural stability, and economical favorability. Other intercalation materials such as coke have replaced the highly reactive Li metal anode. There are several problems associated with metallic lithium as anode. Although a passivative film is formed during operation, which protects the bulk from further decay, it creates dendritic short circuiting and local heating. In order to find a solution for this problem, use of intercalation compounds as anodes has come into practice, including many carbonaceous and non-carbonaceous materials.

Carbonaceous materials have graphene layers, which allow lithium ions to intercalate and de-intercalate during battery operation. The properties of carbon materials such as porosity, structure, and synthesis conditions affect this process significantly[110,111]. The first commercial Sony Li-ion battery used soft carbon as the anode, with a maximum charging voltage of 4.1 V, and the use of hard carbon increased the charging voltage to 4.2 V[112]. The specific capacity of current graphitic carbon anodes is 372 mAh/g. More research is being done on non-carbonaceous materials to improve the specific capacity.

The non-carbon materials include WO_2, TiS_2, $Li_4Ti_5O_{12}$, silicon alloys of Li, and conducting polymers, such as polyacetylene[113-119].

Silicon alloys having formula, $Li_{22}Si_5$, provide a specific capacity of 4200 mAh/g at high temperature and $Li_{15}Si_4$ at room temperature exhibits a capacity of 3579 mAh/g. This is an order of magnitude higher than that of graphitic anode[117-119]. However, the overall capacity of the cell when used with the current cathode ($LiCoO_2$) is not great[120]. The problem associated with silicon based anodes is its transition from amorphous to crystalline during insertion of Li and re-crystallization upon Li removal. This causes disconnectivity in the anode structure, in turn causing safety issues[121]. By using nano-silicon, one can avoid the phase transition[122]. The degradation of silicon can also be reduced by the use of nano materials[123,124].

2.6 Experimental techniques

2.6.1 Powder X-ray diffraction

Powder X-ray diffraction (PXRD) technique is the backbone of solid state chemistry. This technique is commonly used to understand the crystal structure, phase formation, crystallinity, impurity formation, and grain size of materials. In crystalline materials, the atoms or ions are arranged in a regularly repeated fashion to produce parallel planes. The X-rays are produced by accelerating high voltage electron beams towards a metal target, typically Cu. The resultant X-rays are filtered using beryllium windows to obtain a monochromatic X-ray source, normally CuKα radiation with a wavelength, λ = 1.5418Å. When X-rays of certain wavelength have bombarded the

material, it will interact with atoms and undergo diffraction when the condition for Braggs' law (as given in equation [2.5]) is satisfied[125].

$$n\lambda = 2d_{hkl}\sin\theta \qquad [2.5]$$

where n, λ, d_{hkl}, and θ represent an integer (order of the reflection), wavelength of incident X-rays, spacing between two atomic planes, and the angle of incidence, respectively. The schematic representation of diffraction of incident X-rays by a crystal plane is shown in Figure 2.8[125]. The PXRD analysis is carried out over a range of 2θ angles. For all the materials mentioned in this thesis, the 2θ range is between 5 and 80 °. The detector collects the diffracted X-rays and the corresponding output information is a pattern of observed *d*-spacing values against the corresponding 2θ.

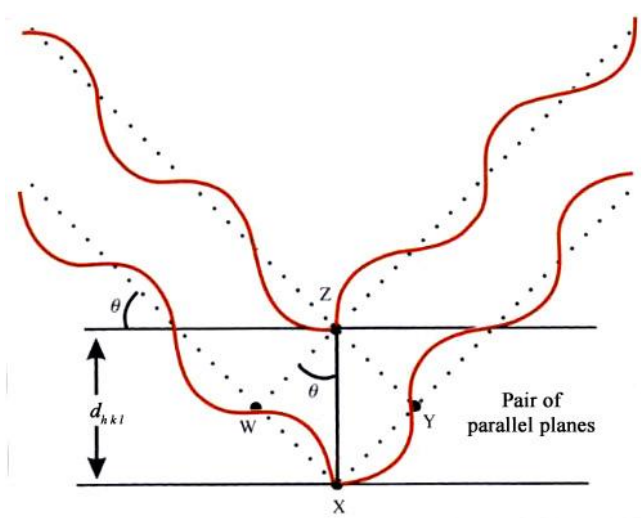

Figure 2. 8 Schematic representation of X-ray diffraction by a pair of crystal planes. The useful (in-phase) scattering occurs when the path difference, WX + XY = $2d_{hkl}\sin\theta$[125].

Further PXRD analysis is carried out using *PROSZKI* and Rietveld refinement (GSAS and EXPGUI package) software to understand the crystal structure and cell parameters. The refinement is a least square approach by which the atomic parameters of a crystal are refined until it matches the experimental observations.

2.6.2 Fourier transform infrared (FTIR) spectroscopy

Fourier transform infrared (FTIR) spectroscopy is an analytical tool used to understand the microscopic properties of a material by deducing the nature of bonds present[126,127]. The data collection is commonly done in the range of 4000-400 cm^{-1} for a specific number of scans (>100 scans). When IR radiation is passed through the material, certain frequency is absorbed by the material when it matches with the natural vibrations of the bond. A unique frequency is absorbed by different bonds. The resultant transmittance is measured through the range of 4000-400 cm^{-1}. The focus of interest for us was checking the bands for carbonyl, O-H and Li-O bonds.

2.6.3 Scanning electron microscopy (SEM)

Scanning electron microscopy (SEM) is an imaging technique which can be extensively used to understand the surface morphology, microstructure, particle size, porosity, and phase formation of samples[66,69,128]. Either powders or polished pellets were used in the present study. In this technique, a high energy electron beam (20 kV) is used to bombard the sample surface. It generates radiation and two types of electrons, namely secondary and backscattered electrons, which are detected by differing detectors and transformed into high contrast images[129].

The secondary electrons (with lower energy) are produced by the inelastic interaction of the incident electron beam with the K-shell of the sample (a few nm deep) which may interact with the ionized atoms before it hits the detector. The electrons which are closer to the surface are detected more easily that those at farther distances. Hence, the secondary electron images are useful to understand the topography and morphology of the samples[130].

The high energy (similar to the incident electron beam) backscattered electrons are originated by the elastic collision of incident electrons with atoms on the sample surface. As a result, atoms with different mass have different brightness in the backscattered images.

2.6.4 Electron probe microanalysis (EPMA)

Electron probe microanalysis (EPMA) can be used to understand the elemental analysis and distribution of atoms (elemental mapping) in solid samples. The detection of one element at a time is possible with this technique with a high resolution. The wavelength of X-rays produced upon the bombardment of the electron beam of a specific wavelength is detected individually for different elements. Specific targets are used for different elements. Several scans are carried out to understand the overall elemental distribution at certain positions on the sample. The image can be read using color scale.

2.6.5 Alternating current (AC) electrochemical impedance spectroscopy (EIS)

Electrochemical impedance spectroscopy is a measure of the resistance of a material to the sinusoidal AC potential. According to Ohm's law, resistance is measured

as the ratio of voltage to current as given in equation [2.6]. The impedance is denoted by Z which is a complex function.

$$R = \frac{V}{I} \qquad [2.6]$$

In EIS, the current response on applying AC voltage across an electrochemical cell at a constant amplitude is measured as a function of frequency (ω). The impedance measurement is usually carried out in the frequency range, 10^{-2} Hz - 10 MHz. The equations [2.7] and [2.8] indicate the complex functions for voltage, and current response respectively.

$$V_t = V_0 \sin(\omega t) \qquad [2.7]$$

$$I_t = I_0 \sin(\omega t + \phi) \qquad [2.8]$$

The angular frequency can be represented as equation [2,9],

$$\omega = 2\pi f \qquad [2.9]$$

where V_t and I_t are the instantaneous voltage, V_0 and I_0 are the signal amplitude, ω is the angular frequency ($rads^{-1}$), ϕ is the phase shift between the signal and response, and *f* is the frequency.

The impedance of an electrochemical system can be derived using Ohm's law (see equation [2.6]) as provided in equation [2.10][131],

$$Z = \frac{E_t}{I_t} = \frac{V_0 \sin(\omega t)}{I_0 \sin(\omega t + \phi)} \qquad [2.10]$$

The equation [2.10] shows that the impedance is dependent on the phase shift. Considering the phase shift, the frequency dependent impedance of a system can be

represented as a vector function as shown by equation [2.11]. The corresponding schematic representation is shown in Figure 2.9[131].

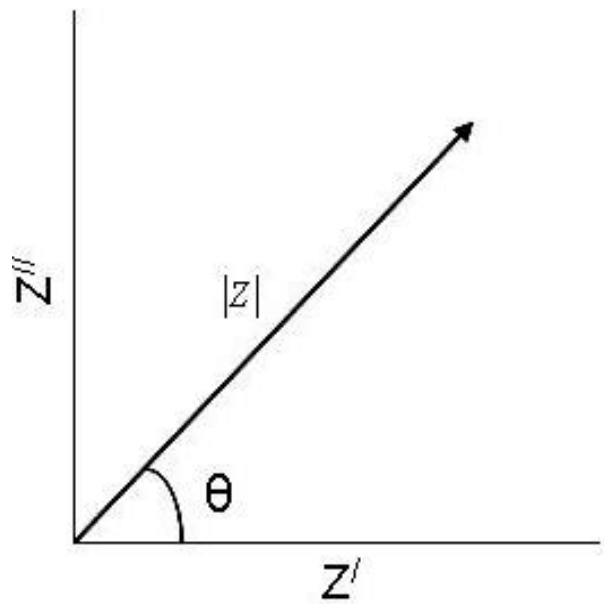

Figure 2. 9 The impedance, *Z* shown as a vector function[131].

$$Z(\omega) = Z^{/} + jZ^{//} \qquad [2.11]$$

where $Z^{/}$ and $Z^{//}$ represent the real and imaginary axes, respectively, and j represents the imaginary complex number, $\sqrt{-1}$.

$$Z^{/} = |Z|\cos(\theta) \qquad [2.12]$$

$$Z^{//} = |Z|\sin(\theta) \qquad [2.13]$$

Combining equations [2.11]-[2.13],

$$Z(\omega) = |Z|[\cos(\theta) + j\sin(\theta)] \qquad [2.14]$$

Impedance data can provide information on different contributions involved in an electrochemical system. A pure resistor (R) has $\phi = 0$ °, and the impedance, Z = R, which is independent of the frequency (equation [2.15]). For a pure capacitor (C), and inductor (L) the phase shift between the perturbation and response are ϕ = -90 and +90 °, respectively (equations [2.16] and [2.17]).

$$Z_R = R \qquad [2.15]$$

$$Z_C = \frac{1}{j\omega C} \qquad [2.16]$$

$$Z_L = j\omega L \qquad [2.17]$$

For non-ideal systems where ϕ is between 45 and 90 °, the representation of the above mentioned relationships are problematic. An additional term called the constant phase element (CPE) is needed to predict the impedance measurement. The CPE is defined by equation [2.18], and the integer *n* can have values between 0 and 1. When n = 1, the CPE represents a pure capacitor, n = 0.5 represents a Warburg element (W), and n = 0 it represents a pure resistor.

$$Z_{CPE} = \frac{1}{C(j\omega)^n} \qquad [2.18]$$

The schematic of typical Nyquist plot and the corresponding equivalence circuit including a parallel resistor - capacitor circuit (as inset) is shown in Figure 2.10. The frequency decreases from left to right as indicated by arrow in the figure.

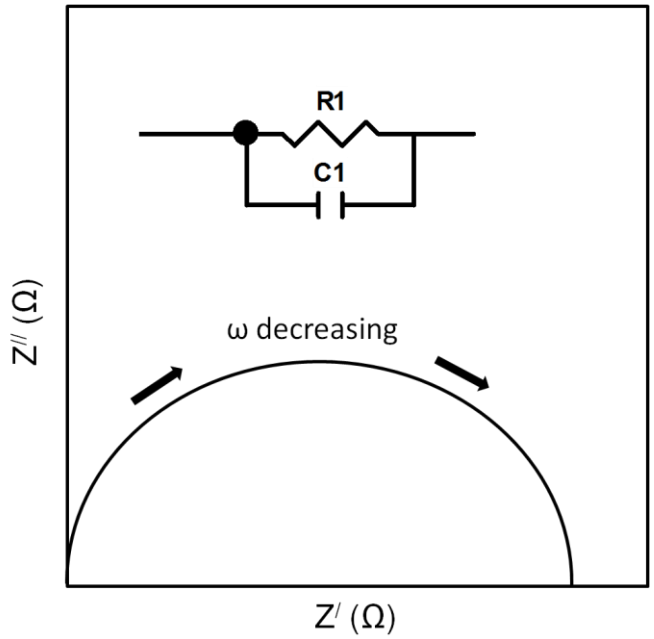

Figure 2. 10 The schematic of a typical Nyquist plot and the corresponding equivalent circuit (inset).

2.6.6 Solid state nuclear magnetic resonance (NMR) spectroscopy

Solid state NMR is a powerful tool to understand the electronic properties and local structure of lithium battery materials, especially cathode and electrolyte materials. Throughout, the thesis is based on garnet-like structured materials that have highly disordered crystal structure. Complete understanding of the Li ion mobility in these materials is not well known; even though, studies based on solid state NMR spectroscopy provide a better understanding of Li ion mobility for several garnet-like systems. Both ^{7}Li and ^{6}Li probes are used for characterization and this technique allows for determination of Li environment in the structure. Powder samples are used for this technique and it has several crystallites in different orientation and which will affect the resolution of NMR spectrum. The nuclear spin interactions are anisotropic, which depend on the molecular

orientations under the applied magnetic field during NMR experiment[132]. There are several other factors that will also affect the resolution of the NMR spectrum; hence it is important to use special techniques such as magic angle spinning (MAS) to obtain high resolution NMR spectra. This is achieved by spinning the sample at high rate at a certain angle, which in turn, increases the rate of molecular orientation. Therefore, the effects such as chemical shift anisotropy are negligible with respect to molecular orientation. ^{27}Al NMR is also used to investigate the Al impurity present in the materials synthesized.

Chapter Three: **Experimental methods**

3.1 Material synthesis

In the present work, we have employed the conventional solid state route (ceramic method) to prepare the investigated solid Li ion electrolytes.

The first step involved in the solid state synthesis is initial mixing of the precursors of stoichiometric amount[1,2] using ball milling (Pulverisette, Fritsch, Germany). The zirconia or alumina bowls and zirconia balls were used for this purpose. A 10 wt % excess of lithium salt is also added at this stage to compensate for the lithium loss due to volatilization during sintering[3-10]. To ensure the homogeneous mixing, ball milling time was fixed for 12 h at a rate of 200 rpm. 2-isopropanol is used as a mixing reagent and it also ensures the easy drying in air after ball milling. The dried powders are transferred into clean alumina crucibles and heated at 700 °C for 6 h. The resultant powders were ground into fine powders using a mortar and pestle to make pellets. The pellets were made in an isostatic press (isostatic press, P. O. Weber) by applying a pressure of 183 MPa for 5 minutes. The pellets were covered with mother powder in each sintering step. An initial sintering at 900 °C for 24 h was carried out in all cases. After sintering one of the pellet samples is crushed into powder for phase characterization. A final sintering at 1100 °C for 6 h was done in order to increase the density and crystallinity of pellets. The reaction scheme is illustrated as a schematic in Figure 3.1 and is used for the preparation of all the materials investigated in this thesis.

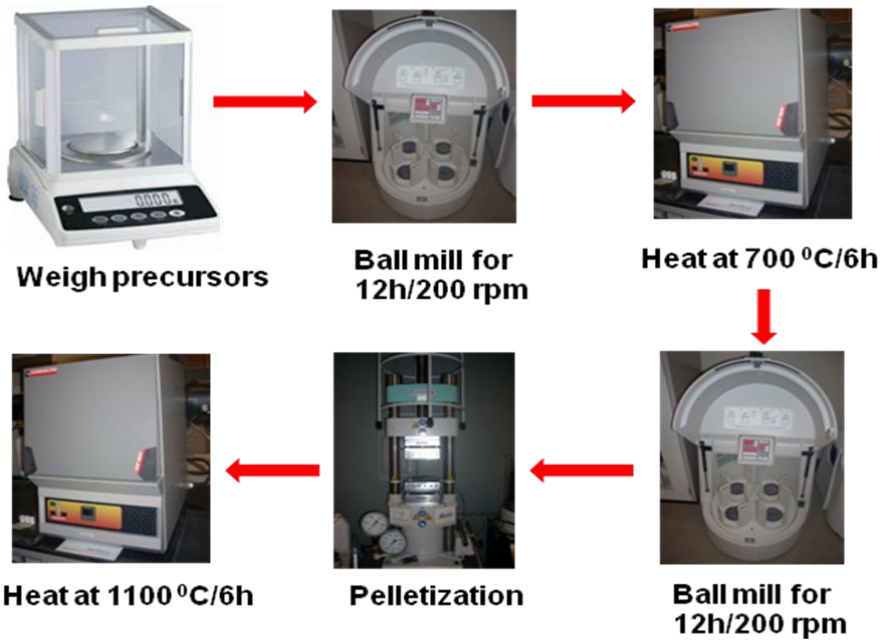

Figure 3. 1 Schematic representation of conventional solid state synthesis.

Compounds of nominal compositions of $Li_5La_3Nb_{2-x}Y_xO_{12-\delta}$ (x = 0-1) and $Li_{5+2x}La_3Nb_{2-x}Y_xO_{12}$ ($0.05 \leq x \leq 0.75$) were prepared using $LiNO_3$ (99 %, Alfa Aesar), La_2O_3 (99.99 %, Alfa Aesar, pre-heated at 800 ^oC for 24 h), Nb_2O_5 (99.5 %, Alfa Aesar), and $Y(NO_3)_3$ (99.9 %, Alfa Aesar). To prepare the compound $Li_{6.5}La_{2.5}Ba_{0.5}ZrTaO_{12}$, the precursors used were $LiNO_3$ (99 %, Alfa Aesar) La_2O_3 (99.99 %, Alfa Aesar, pre-heated at 800 ^oC for 24 h), $Ba(NO_3)_2$ (AR grade, BDH), ZrO_2 (99 %, Alfa Aesar) and Nb_2O_5 (99.5 %, Alfa Aesar). The precursors were used as received and no additional purification was done. The sintered pellets were cut into small discs (~ 1-2 mm thickness) using diamond wheel (Buehler, Isomet 5000) for further characterizations. The representation of synthesis in general format is provided in equations [3.1]–[3.3]. Complete information

on the stoichiometry of the compounds synthesized for this thesis work is shown in Table 3.1.

The formation of the targeted chemical compositions can be expressed as:

$$2.5Li_2O + 1.5La_2O_3 + \left(\tfrac{2-x}{2}\right)Nb_2O_5 + \tfrac{x}{2}Y_2O_3 \xrightarrow[\text{Air}]{1100°C/6\ h} Li_5La_3Nb_{2-x}Y_xO_{12-\delta} \qquad [3.1]$$

$$\left(\tfrac{5+2x}{2}\right)Li_2O + 1.5La_2O_3 + \left(\tfrac{2-x}{2}\right)Nb_2O_5 + \tfrac{x}{2}Y_2O_3 \xrightarrow[\text{Air}]{1100°C/6\ h} Li_{5+2x}La_3Nb_{2-x}Y_xO_{12} \qquad [3.2]$$

$$3.25Li_2O + 1.25La_2O_3 + 0.5BaO + ZrO_2 + 0.5Nb_2O_5 \xrightarrow[\text{Air}]{1100°C/6\ h} Li_{6.5}La_{2.5}Ba_{0.5}ZrNbO_{12} \qquad [3.3]$$

Table 3. 1 Stoichiometric formulae of compounds synthesized in this thesis work. It is divided according to the relevant chapter number.

Section	Stoichimetric formula
Chapter 4	$Li_5La_3Nb_2O_{12}$
	$Li_5La_3Nb_{1.95}Y_{0.05}O_{11.95}$
	$Li_5La_3Nb_{1.9}Y_{0.1}O_{11.9}$
	$Li_5La_3Nb_{1.85}Y_{0.15}O_{11.85}$
	$Li_5La_3Nb_{1.8}Y_{0.20}O_{11.8}$
	$Li_5La_3Nb_{1.75}Y_{0.25}O_{11.75}$
	$Li_5La_3Nb_{1.5}Y_{0.5}O_{11.5}$
	$Li_5La_3NbYO_{11}$
Chapter 5	$Li_{5.1}La_3Nb_{1.95}Y_{0.05}O_{12}$
	$Li_{5.2}La_3Nb_{1.9}Y_{0.1}O_{12}$
	$Li_{5.4}La_3Nb_{1.8}Y_{0.2}O_{12}$
	$Li_{5.5}La_3Nb_{1.75}Y_{0.25}O_{12}$
	$Li_6La_3Nb_{1.5}Y_{0.5}O_{12}$
	$Li_{6.5}La_3Nb_{1.25}Y_{0.75}O_{12}$
Chapter 6	$Li_{6.5}La_{2.5}Ba_{0.5}ZrTaO_{12}$

3.2 Characterization

3.2.1 Structural characterization

The phase purity was measured employing a powder X-ray diffraction (PXRD; Bruker D8 powder X-ray diffractometer (CuKα, 40 kV, 40 mA). The image of PXRD instrument employed is shown in Figure 3.2. The data collection was carried out in the 2θ range, 5-80 ° at a step scan of 0.2 °/min for minimum 3 h and for the Rietveld refinements, a long scan for 12 h was done. *In-situ* measurements were employed in a high temperature reactor chamber (Anton Paar XRK 900) which is shown in Figure 3.3. The *Eva program* was used to index the peaks. The JCPDS (Joint Committee on Powder Diffraction Standards) database provides the crystal information of most of the chemical compounds. The recorded PXRD pattern was compared with the JCPDS files of parent compound $Li_5La_3Nb_2O_{12}$ of different morphology (cubic and tetragonal). Further analysis on PXRD data was done using *PROSZKI program* and Rietveld refinement using *GSAS* program and *EXPGUI* interface to calculate the cell parameters of the crystal structure.

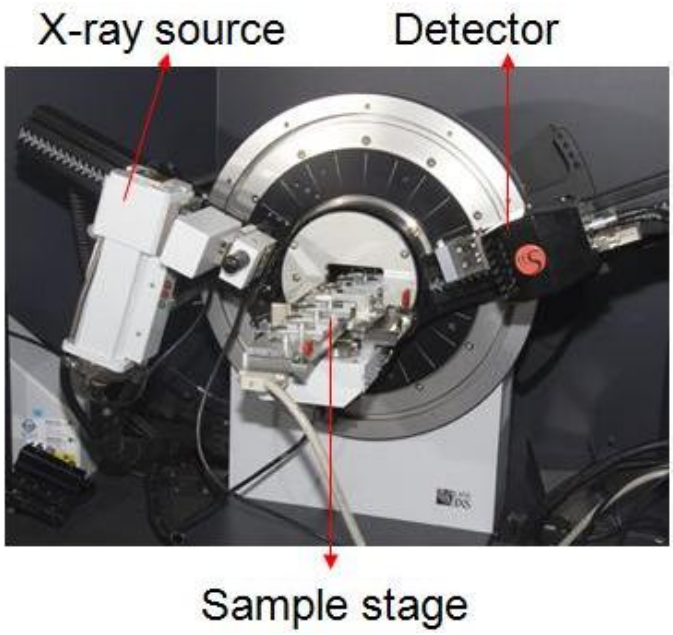

Figure 3. 2 Bruker D8 powder X-ray diffractometer used for PXRD measurements.

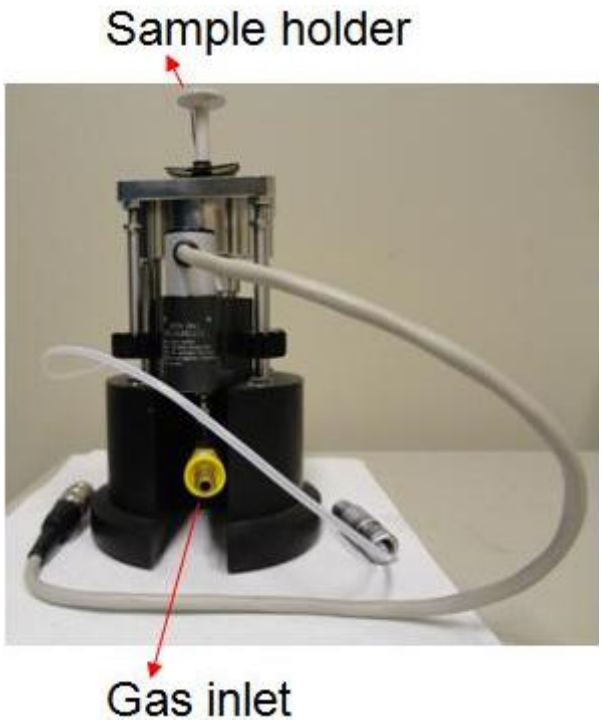

Figure 3. 3 High temperature reactor chamber (Anton Paar XRK 900) used for *in-situ* PXRD measurements.

3.2.2 Morphological and elemental studies

The morphological characterization was done by scanning electron microscopy (SEM) (Philips FEI XL30) in the Microscopy and Imaging Facility, Health Sciences Center, University of Calgary as shown in Figure 3.4. The pellet samples were used for all the measurements. The pellets were polished well before mounting it on a stainless steel stud containing carbon tape, and a very thin layer (few nm thicknesses) of Au was sputtered on top of it to ensure the electronic conductivity. A high vacuum of the order of 10^{-4} Torr is used for the operation and a working distance of 10 mm is maintained. The elemental analysis was done using EDX (Energy Dispersive X-ray Spectroscopy) measurement to get a rough understanding of the composition of the material by scanning different positions on the sample surface.

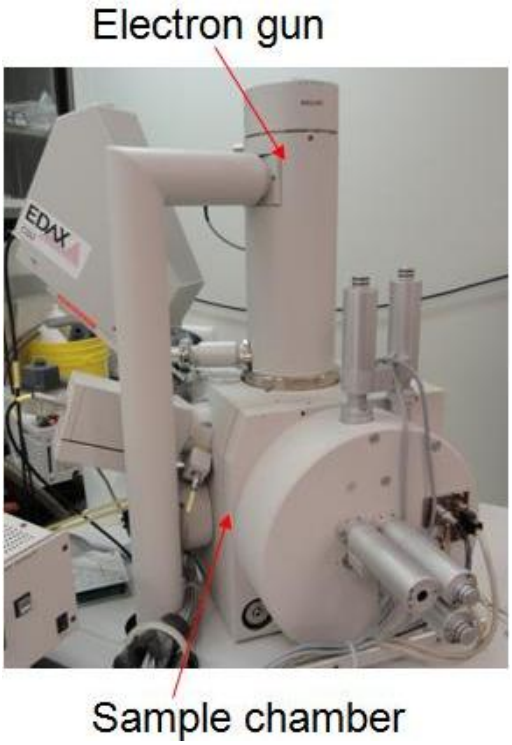

Figure 3. 4 Scanning electron microscopy (SEM) (Philips FEI XL30) instrument used for morphological studies.

Electron probe microanalysis (EPMA) (Electron Probe Microanalyser, JEOL JXA-8200) coupled with a wavelength-dispersive spectrometer (WDS) was used for the elemental mapping of materials prepared. Usually samples are prepared as polished pellet forms for this characterization. EPMA was carried out under vacuum at an excitation voltage of 15 kV and current of 11.51 nA.

3.2.3 Electrical conductivity measurements

For the electrical conductivity measurements, the pellets were painted with Au paste on both sides using a brush. Two layers of coating were used to obtain a good electrical conductivity. Each coating was done after drying in air oven at ~ 80 °C for 5 minutes. Finally, the coated pellets were cured at 600 ^{o}C for 1h to evaporate the organic matter which comes from the electronic solution used to make the Au paste. The image of a pellet coated with gold which is used for electrical measurements is shown in Figure 3.5. The impedance analysis was carried out using a Solartron SI 1260 impedance and gain-phase analyzer in the frequency range of 0.01 Hz to 10 MHz in air. The normal temperature range used for electrical measurement of garnet-like materials is 23-330 °C. Both the heating and cooling cycles were done after reaching thermal equilibrium at specific temperature. Minimum two runs were carried to check the reproducibility.

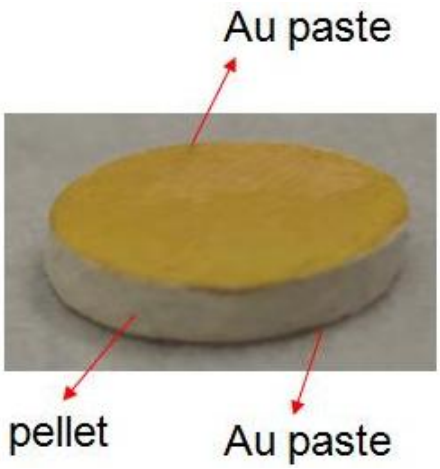

Figure 3. 5 The schematic representation of Au coated pellet prior to the impedance measurement.

The schematic representation of a cell set up for impedance measurements is provided in Figure 3.6. In addition, multiple pellets were investigated from each batch of synthesis of the same material. Dry ice in combination with ethylene glycol and ethanol in different ratios was used to maintain very low temperatures (below 25 °C)[11]. The *Zview* and *Zplot* programs were used for the impedance data collection and analysis.

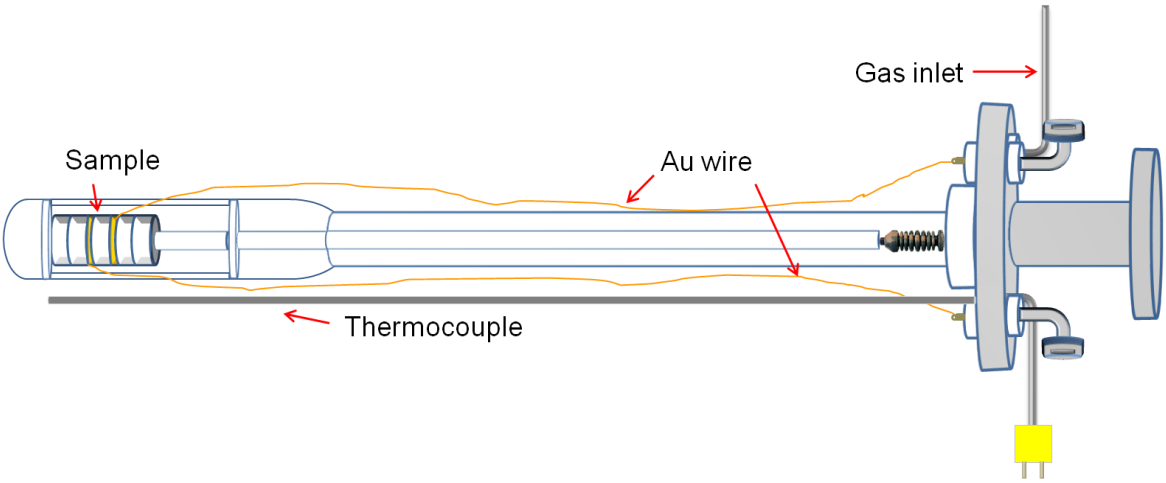

Figure 3. 6 The schematic representation of cell arranged with pellet sample for impedance measurement. The current collectors (Au wires) are attached to either side of the sample and the thermocouple allows temperature measurements.

3.2.4 Solid state NMR (nuclear magnetic resonance) studies

The solid state NMR studies have been carried out using the facility at the University of Calgary. The ^{27}Al and ^{7}Li magic angle spinning nuclear magnetic resonance (MAS NMR) (AMS 300, Bruker, at spinning rate 5 kHz) were performed for the powdered samples and the chemical shift values were expressed against the standards $Al(NO_3)_3$, and LiCl, respectively.

The detailed study of garnet like $Li_{6.5}La_{2.5}Ba_{0.5}ZrTaO_{12}$ described in chapter 6 was done by employing variable-temperature ^{7}Li nuclear magnetic resonance (VTNMR) spectroscopy using an Avance III NMR spectrometer (Bruker BioSpin, Rheinstetten) in combination with a shimmed 7 T cryomagnet (Bruker) at the University of Hannover, Germany[12]. The resonance frequency was $\omega_0/2\pi$ = 117 MHz. NMR spectra were acquired with the help of a one-pulse sequence. The recycle delay between each scan was at least 5 T_1 where T_1 is the spin-lattice relaxation time in the laboratory frame of reference. NMR T_1 times were recorded with the saturation recovery pulse sequence: a comb of closely spaced 90° pulses destroys longitudinal magnetization and its recovery is probed as a function of delay time with a single detection pulse. A ^{6}Li magic angle spinning (MAS) NMR spectrum was recorded at 88 MHz using an Avance 600 Bruker NMR spectrometer connected to a cryomagnet magnet with a nominal field of 14.1 T. The standard used was 2.5 mm MAS-NMR probe which was operated at a spinning speed of 30 kHz. Additionally, with the same equipment a ^{27}Al MAS NMR spectrum was also recorded.

3.2.5 Chemical stability tests

Selected samples were used for chemical stability investigation. The chemical stability tests of the electrolyte materials prepared were carried out under different conditions including high voltage cathodes ($Li_2CoMn_3O_8$ and $Li_2FeMn_3O_8$), anode (carbon) and water. Both the *ex-situ* and *in-situ* PXRD technique was used to analyze the structural stability after the chemical test. For this purpose the selected electrolyte and electrode material was mixed in 1:1 wt. % ratio and heat treated in varying temperatures. For *ex-situ* measurements, the heat treatments at 200, 400, 600, 800 and 900 ^{o}C for 24h in air was used. The samples were heated at the rate of 10 ºC/min and then stabilized for 30 min, prior to each *in-situ* measurement in the temperature range of 30-900 ºC.

For the H_2O stability test, the pellet was crushed into powder (2g) and was then treated with H_2O under mechanical stirring for 2 days. After that the water treated powder was washed again with water several times and filtered out. The dried sample was investigated using *in-situ* PXRD with high temperature reactor chamber. The samples were heated at the rate of 10 ºC/min and then stabilized for 30 min, prior to each measurement in the range of 30-900 ºC. The thermal stability measurement was conducted using thermo gravimetric analysis (TGA) (Mettler Toledo thermal system; TGA/DSC1 HT 1600 ºC system) in the range of 25-800 ºC under N_2 atmosphere. The ramping rate was set to 10 ºC/min for both heating and cooling cycles and two subsequent cycles were performed. The equipment employed for thermal analysis is provided in Figure 3.7.

Figure 3. 7 Thermo gravimetric analysis (TGA) (Mettler Toledo thermal system; TGA/DSC1 HT 1600 ºC) system.

3.2.6 Fourier transform infrared (FTIR) spectroscopic studies

The Fourier transform infrared spectroscopy (FTIR) (NEXUS Model 470 FTIR, Varian Model 7000 FTIR) was used for FTIR measurements under air atmosphere. Prior to the measurements, the samples and KBr powder were ground and dried in vacuum oven at ~ 200 °C for overnight. The samples are dispersed in KBr powder in the sample holder for the measurements. The instrument chamber was purged with inert gas to eliminate the H_2O and CO_2 content in air to avoid any impurity peaks due to contamination.

3.3 Error considerations

- One of the plausible errors from the material synthesis steps is the impurities coming from the precursors as most of them are only ~ 99 % pure. Another potential error could be in the stoichiometric formula since there is a chance of Li_2O volatilization during sintering in the synthesis step. Hence, the investigated compounds could be considered to have a nominal chemical formula.
- The detection limit of PXRD analysis is 5 % and hence traces of impurities present in the sample cannot be detected. Also potential amorphous phases also cannot be identified.
- The error in the measurement of temperature in tubular furnaces which are used for impedance measurements is ~ ±3 °C. In addition, the stabilization time at each temperature step is not uniform, which could implement some error in the impedance results.
- At high frequency range, possible errors could be due to cable contact, noise, and cable connection. The cable used to connect the impedance cell and the instrument is ~ 2 m length.
- The contribution of impedance at open circuit potential condition is not taken into account in the impedance analysis.
- During the TGA measurements, the gas flow rate is manually set to 90 ml/min. Some times the level drops down which could implement error in the measurement.
- Author is also responsible for any oversight on data interpretation.

Chapter Four: **Effect of Y substitution for Nb in $Li_5La_3Nb_2O_{12}$ on Li ion conductivity of garnet-type solid electrolytes**

4.1 General overview

This chapter discusses the effect of Y substitution for Nb on Li ion conductivity in the well-known garnet-type, $Li_5La_3Nb_2O_{12}$. It is a systematic study to understand the role of oxygen content on transport properties while keeping a constant lithium ion concentration. It has been assumed that the doping of trivalent Y for pentavalent Nb in $Li_5La_3Nb_2O_{12}$ may create oxide ion vacancies ($V_o^{\bullet\bullet}$) in the structure to maintain the electronic charge balance. This can be represented by Kroger-Vink notation as shown in equation [4.1].

$$O_O^x + Nb_{Nb}^x \xrightarrow{\frac{1}{2}Y_2O_3} Y_{Nb}^{//} + V_O^{\bullet\bullet} + \frac{1}{2}O_2 \qquad [4.1]$$

Garnet-type metal oxides of the nominal chemical formula, $Li_5La_3Nb_{2-x}Y_xO_{12-\delta}$ ($0 \leq x \leq 1$) were prepared by conventional solid state (ceramic method) reactions in air at elevated temperatures using high purity metal oxides and metal salts in stoichiometric amounts.

Powder X-ray diffraction (PXRD) showed formation of the single-phase cubic garnet-like structure for x up to x = 0.25 and impurities above x = 0.25. The cubic lattice constant increases with increasing Y content in $Li_5La_3Nb_{2-x}Y_xO_{12-\delta}$ and are consistent with expected ionic radius trend. ^{7}Li MAS NMR showed a very sharp single peak, which could be attributed to fast migration of ions between various sites in the garnet structure, with a chemical shift close to 0 ppm with respect to solid LiCl. The chemical shift value confirmed that Li ions are distributed at an average octahedral coordination in $Li_5La_3Nb_{2-x}Y_xO_{12-\delta}$. Y-doped compounds showed comparable electrical conductivity to that of the

parent compound, $Li_5La_3Nb_2O_{12}$. The x = 0.1 member of $Li_5La_3Nb_{2-x}Y_xO_{12-\delta}$ showed total (bulk + grain-boundary) ionic conductivity of 1.44 x 10^{-5} Scm^{-1} at 23 ºC in air, with an activation energy of 0.51 eV at 23-250 ºC.

4.2 Results and discussion[1]

4.2.1 Phase characterization

Figure 4.1 shows the powder X-ray diffraction (PXRD) patterns of as-prepared $Li_5La_3Nb_{2-x}Y_xO_{12-\delta}$ ($0 \leq x \leq 1$)[1,2]. A "single-phase" garnet-type structure was observed for x up to x = 0.25, with a very small amount of an unknown impurity peak (less than 10 % intensity) marked as * in all the compositions. Starting from the x = 0.25 member, there is an extra peak marked as + is due to $LiNb_3O_8$ (International Crystal Structure database, ICSD No. 01-075-2154) and another impurity peak marked as x due to $LiLaNb_2O_7$ (ICSD No. 01-081-1193). Major peaks could be indexed to a simple cubic garnet-type structure based on the space group *Ia-3d* and is similar to that of the parent compound, $Li_5La_3Nb_2O_{12}$[3]. All the observed lines fit into the cubic phase and there is no evidence for tetragonal modification, as reported for $Li_7La_3Zr_2O_{12}$[4]. The number of impurity peaks began to increase for members with x > 0.25 in $Li_5La_3Nb_{2-x}Y_xO_{12-\delta}$.

---

[1] Narayanan, S.; Thangadurai, V. *J. Power Sources*, **2011**, *196*, 8080-8090
[2] Narayanan, S.; Thangadurai, V. *ECS Trans.* **2011** *35* (32) 125-131

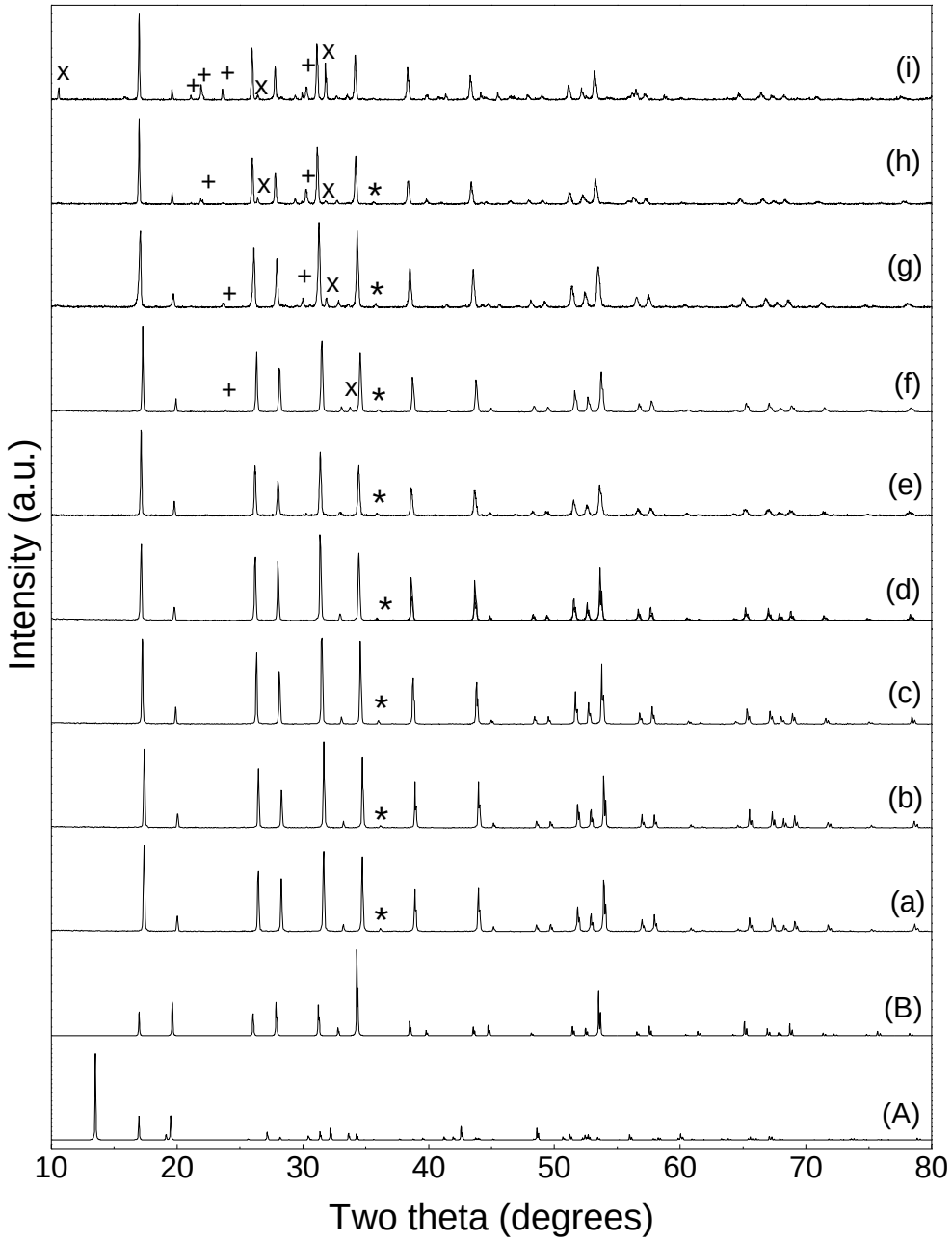

Figure 4. 1 Powder XRD patterns of $Li_5La_3Nb_{2-x}Y_xO_{12-\delta}$ (a) x = 0, (b) x = 0.05, (c) x = 0.1, (d) x = 0.15, (e) x = 0.2, (f) x = 0.25, (g) x = 0.5, (h) x = 0.75, and (f) x = 1. For comparison, the calculated PXRD patterns using PowderCell program of (A) tetragonal $Li_7La_3Zr_2O_{12}$ (*a* = 13.130(2) Å; *c* = 12.675(2) Å; space group: $I4_1/acd$)[4] and (B) cubic $Li_5La_3Nb_2O_{12}$ (*a* = 12.80654(11) Å; space group: *Ia*-3*d*)[3] are given.

Table 4.1 lists the indexed PXRD patterns of $Li_5La_3Nb_{2-x}Y_xO_{12-\delta}$ (x = 0.05 and 0.1) and for the rest of the compositions are provided in Appendix A (Table A.1-A.2). As anticipated, the cubic lattice constant increases with increasing Y substitution in $Li_5La_3Nb_2O_{12}$ (Figure 4.2)[5]. The six-fold oxygen coordinated Nb (0.64 Å) show lower ionic radius than that of Y (0.9 Å)[6].

Table 4. 1 Indexed powder XRD patterns of $Li_5La_3Nb_{2-x}Y_xO_{12-\delta}$ (x = 0.05; 0.1)[1].

			x = 0.05			x = 0.1		
h	*k*	*l*	$d_{obs.}$ (Å)	$d_{cal.}$ (Å)	$I_{obs.}$ (%)	$d_{obs.}$ (Å)	$d_{cal.}$ (Å)	$I_{obs.}$ (%)
2	1	1	5.093	5.192	100	5.151	5.185	87
2	2	0	4.436	4.496	20	4.469	4.490	22
3	2	1	3.367	3.399	83	3.386	3.394	93
4	0	0	3.156	3.179	53	3.173	3.175	69
4	2	0	2.825	2.844	98	2.838	2.840	100
3	3	2	2.696	2.711	10	2.708	2.708	10
4	2	2	2.583	2.596	98	2.594	2.592	100
5	1	0	2.483	2.494	4	2.493	2.491	5
5	2	1	2.313	2.322	64	2.322	2.319	60
6	1	1	2.059	2.063	64	2.065	2.060	55
6	2	0	2.007	2.011	8	2.015	2.008	6
6	3	1	1.874	1.875	10	1.879	1.872	11
4	4	4	1.835	1.836	9	1.840	1.833	10

6	4	0	1.762	1.764	33	1.768	1.761	42
7	2	1	1.726	1.731	14	1.736	1.728	29
6	4	2	1.700	1.700	73	1.704	1.697	78
6	5	1	1.616	1.615	19	1.621	1.626	15
8	0	0	1.590	1.590	18	1.595	1.587	23
8	2	1	-	-	-	1.526	1.529	5
6	5	3	1.521	1.520	5	1.504	1.518	3
7	5	2	1.443	1.440	4	1.446	1.438	4
8	4	0	1.424	1.422	26	1.428	1.420	20
8	4	2	1.390	1.388	23	1.393	1.386	17
7	6	1	1.374	1.371	14	1.378	1.369	10
6	6	4	1.358	1.356	17	1.362	1.354	14
9	3	2	1.314	1.312	8	1.318	1.310	8
10	1	0	1.263	1.265	4	1.265	1.264	4
10	3	0	1.216	1.218	10	1.219	1.216	10
			a =12.717(2) Å			*a* = 12.700(7) Å		

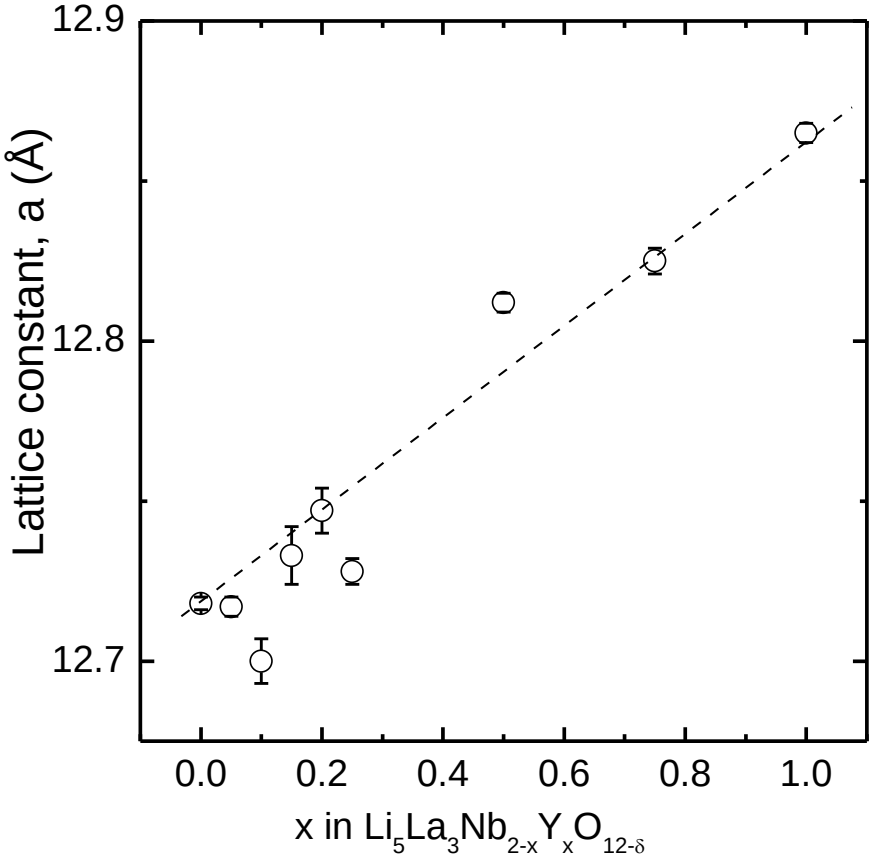

Figure 4. 2 Effect of Y doping into $Li_5La_3Nb_{2-x}Y_xO_{12-\delta}$ (x = 0-1) on the lattice constant.

4.2.2 Morphology and solid state ^{7}Li NMR studies

Figure 4.3 and 4.4 include typical SEM images of the as-prepared $Li_5La_3Nb_{2-x}Y_xO_{12-\delta}$ and showed that Y substitution influences the particle size[1,2]. Comparable images for other garnet-type materials were also reported in the literature[7]. We clearly see that Y substitution for Nb in $Li_5La_3Nb_2O_{12}$ increases the crystallite to crystallite contact. The roughness of the surface may occur during sample preparation for SEM using a diamond saw. Based on the SEM study, Y promotes better sintering of the investigated garnet-type materials.

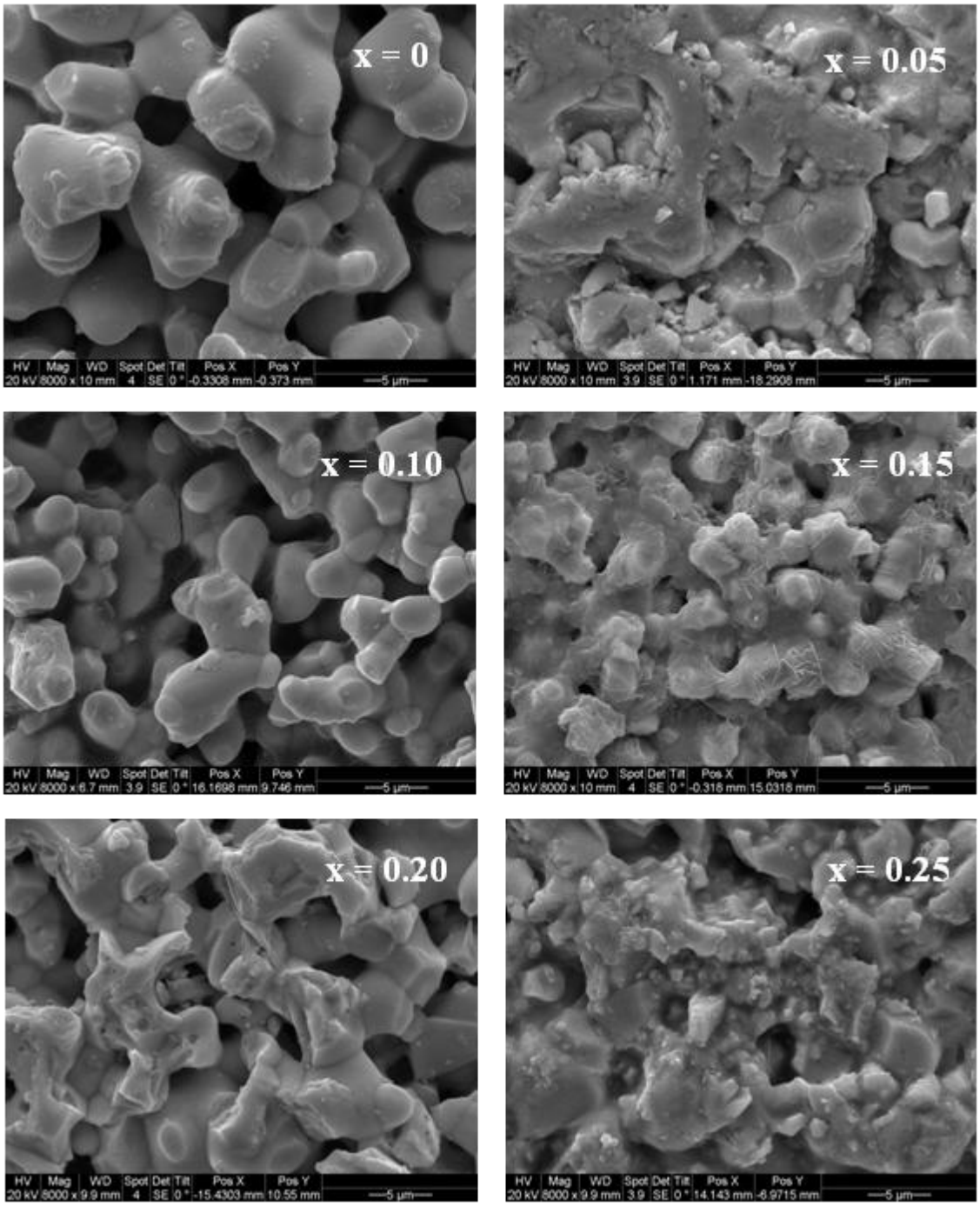

Figure 4. 3 Typical SEM images of $Li_5La_3Nb_{2-x}Y_xO_{12-\delta}$ (x = 0 to 0.25) prepared at 1100 °C in air. The effect of Y doping on the morphology is clearly seen[1].

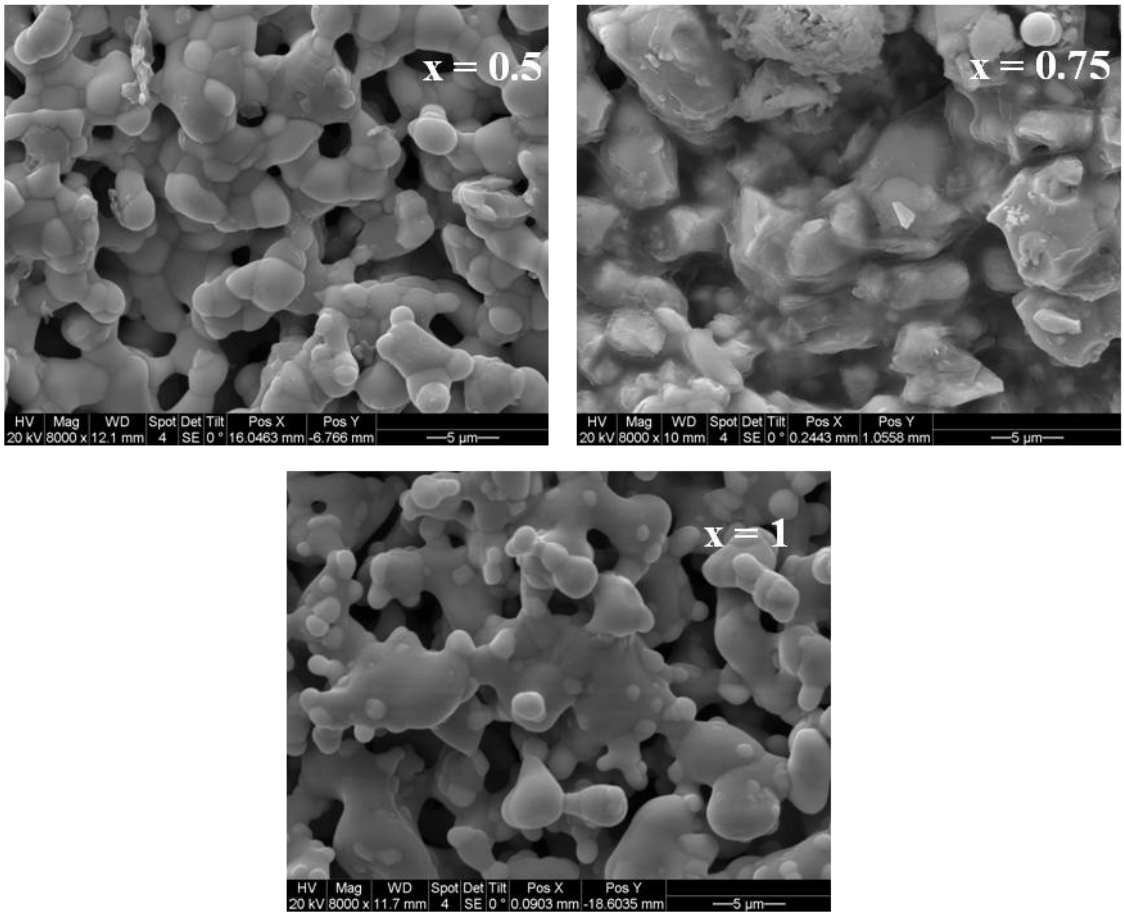

Figure 4. 4 Typical SEM images of $Li_5La_3Nb_{2-x}Y_xO_{12-\delta}$ (x = 0.5 to 1) prepared at 1100 °C in air. The effect of Y doping on the morphology is clearly seen[2].

The room temperature solid state ^{7}Li magic angle spinning nuclear magnetic resonance (MAS NMR) of $Li_5La_3Nb_{2-x}Y_xO_{12-\delta}$ is presented in Figure 4.5. The chemical shift value was expressed with reference to solid LiCl. Very interestingly, all the investigated compounds show a "single peak" at a chemical shift of around 0 ppm and similar data was reported for several other garnet-type compounds in the literature[8-10]. Accordingly, we believe that Li in the investigated compounds may occupy a similar crystallographic site to that of the parent garnet-type $Li_5La_3Nb_2O_{12}$. The narrowing of the peak may be attributed to fast Li ion mobility in the Y-doped $Li_5La_3Nb_{2-x}Y_xO_{12-\delta}$. It has

been proposed that the octahedral site Li ions are more mobile than the tetrahedral sites. In the parent compound, Li occupancy at octahedral sites is 2/3 and that at tetrahedral sites is 1/3 [3,11-13].

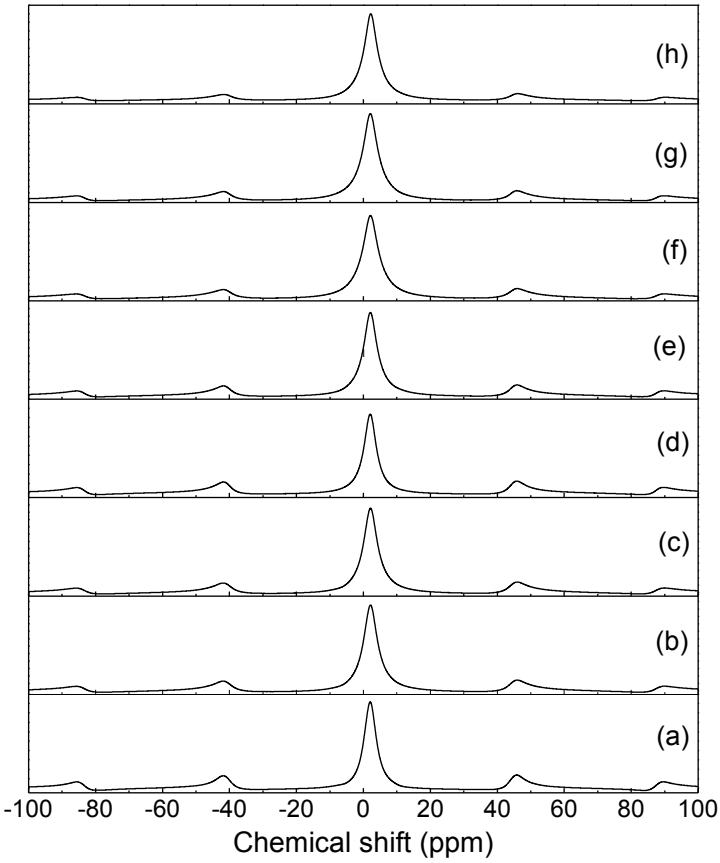

Figure 4. 5 Solid state ^{7}Li NMR spectra of $Li_5La_3Nb_{2-x}Y_xO_{12-\delta}$ prepared at 1100 °C in air (a) x = 0, (b) x = 0.05, (c) x = 0.10, (d) x = 0.15, (e) x = 0.20, (f) x = 0.25, and (g) x = 0.75, (h) x = 1. The chemical shift values are expressed with respect to solid LiCl[2].

In this study, the nominal concentration of Li ions was kept constant to elucidate the role of oxygen defects on Li ion conduction. Bond valence analysis showed that the Li ion conduction path appears to be around the transition metal octahedra in the garnet-type frame work[14]. However, further experimental studies including neutron diffraction and

NMR studies are required to fully understand the crystal structure and the proposed chemical substitution.

4.2.3 Electrical properties[2]

AC impedance spectroscopy was used to evaluate the effect of Y doping in $Li_5La_3Nb_2O_{12}$ on Li ion conductivity. The typical AC impedance plots for $Li_5La_3Nb_{2-x}Y_xO_{12-\delta}$ at 50 and 150 °C are shown in Figures 4.6 and 4.7[2]. The high frequency portion is zoomed in and given as the inset in Figures 4.6 and 4.7 for clarity.

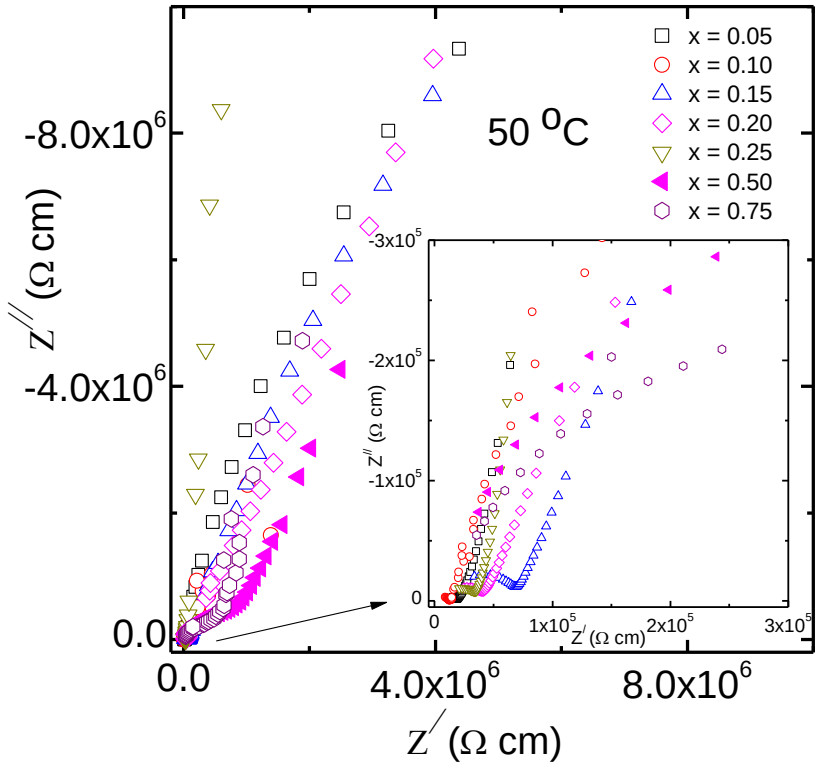

Figure 4. 6 Typical AC impedance plots at 50 °C of $Li_5La_3Nb_{2-x}Y_xO_{12-\delta}$ (x = 0.05, 0.1, 0.15, 0.2, 0.25, 0.5, and 0.75). The inset figure shows the expanded view of the high frequency region.

---

[2] Narayanan, S.; Thangadurai, V. *ECS Trans.* **2011** *35* (32) 125-131

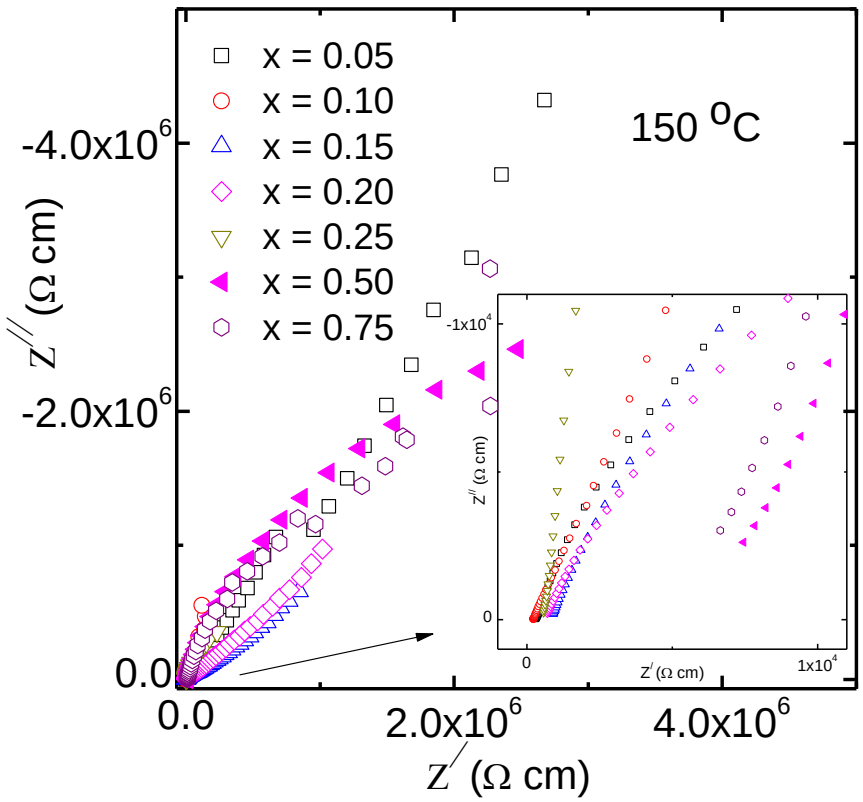

Figure 4. 7 Typical AC impedance plots at 150 °C of $Li_5La_3Nb_{2-x}Y_xO_{12-\delta}$ (x = 0.05, 0.1, 0.15, 0.2, 0.25, 0.5, and 0.75). The inset figure shows the expanded view of the high frequency region.

At lower temperatures, the impedance plots consist of a semicircle due to the bulk and grain-boundary resistance, and a tail due to electrode effects in the high, intermediate, and low frequency regimes, respectively. However at higher temperatures, it becomes more complicated to resolve these contributions meaningfully. Hence, for calculating electrical conductivity, the low-frequency minimum on the real axis was used as resistance 'R' at lower temperatures and the intercept to the real axis was used at higher temperatures. A similar approach has been used in the literature to determine the electrical conductivity of garnet-type solid Li ion electrolytes[15-17].

A typical fitting of the impedance data for $Li_5La_3Nb_{1.95}Y_{0.05}O_{11.95}$ and $Li_5La_3Nb_{1.75}Y_{0.25}O_{11.75}$ at 50 °C are shown in Figures 4.8 and 4.9. The equivalent circuits used for the simulation using *Zview* program include a parallel resistor-constant phase element and a constant phase element which is shown in Figure 4.10.

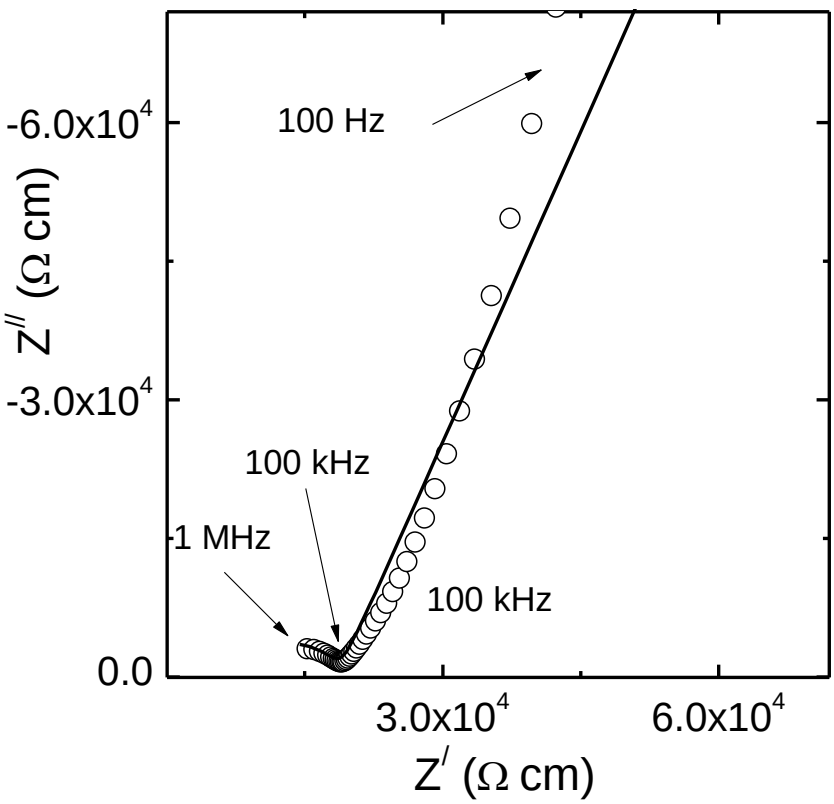

Figure 4. 8 Typical AC impedance plot at 50 °C of $Li_5La_3Nb_{1.95}Y_{0.05}O_{11.95}$. The solid line represents the fitting data and the symbol represents the measured data. The equivalent circuit used for fitting includes a parallel resistor-constant phase element, and a constant phase element.

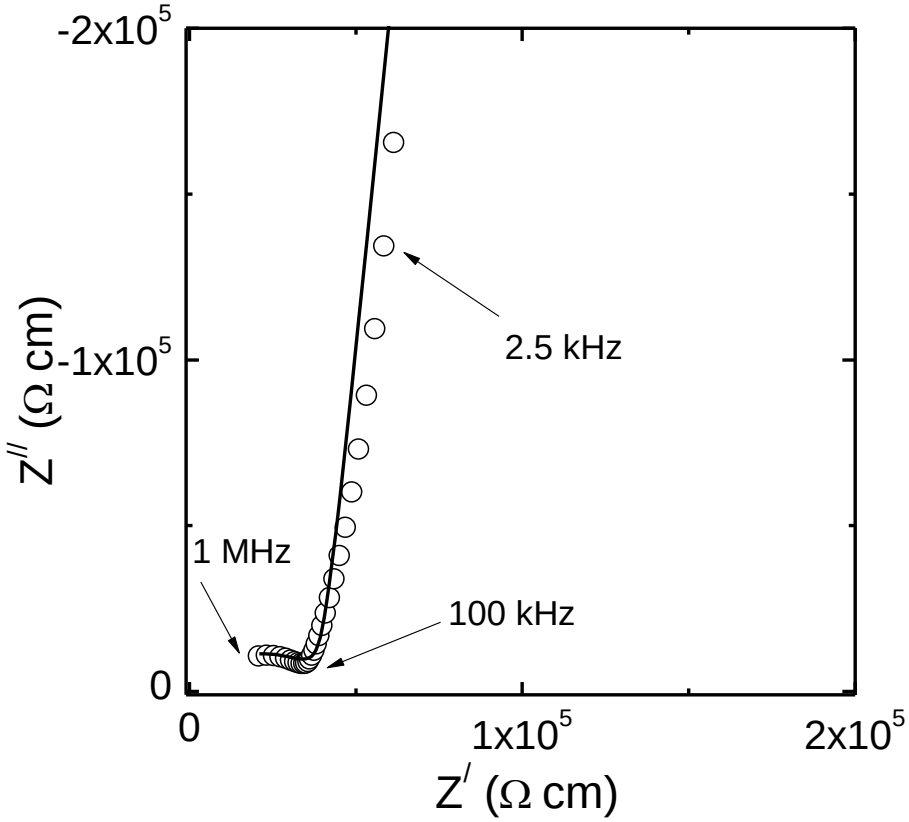

Figure 4. 9 Typical AC impedance plot at 50 °C of $Li_5La_3Nb_{1.75}Y_{0.25}O_{11.75}$. The solid line represents the fitting data and the symbol represents the measured data. The equivalent circuit used for fitting includes a parallel resistor-constant phase element, and a constant phase element.

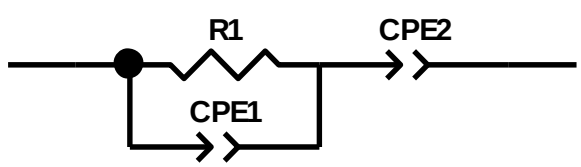

Figure 4. 10 The equivalent circuit used for the fitting of AC impedance plot at 50 °C of $Li_5La_3Nb_{1.95}Y_{0.05}O_{11.95}$ and $Li_5La_3Nb_{1.75}Y_{0.25}O_{11.75}$ (shown in Figures 4.8 and 4.9). It includes a parallel resistor-constant phase element, and a series constant phase element.

The equation used to calculate electrical conductivity throughout this thesis is given in equation [4.2]:

$$\sigma = \left(\frac{1}{R}\right)\left(\frac{l}{a}\right) \qquad [4.2]$$

where l is the thickness of the sample and a is the area of the electrode. The electrical conductivity as a function of temperature was determined and plotted using the Arrhenius equation [4.3]:

$$\sigma T = A\exp^{\left(-\frac{E_a}{kT}\right)} \qquad [4.3]$$

where A is the pre-exponential term, E_a is the activation energy, T is the temperature, and k is the Boltzmann constant.

Figure 4.11 shows the Arrhenius plots for electrical conductivity of $Li_5La_3Nb_{2-x}Y_xO_{12-\delta}$ prepared at 1100 °C[2]. The data obtained during the heating and cooling cycles follow the same line, indicating equilibrium behavior. The substitution of Y for Nb is assumed to create oxygen vacancies in the garnet-type structure for charge compensation. These oxide ion vacancies do not seem to support the Li ion migration in the garnet-type structure. Several authors recently showed the effect of chemical doping such as Sb^{V}, W^{VI} and Te^{VI} for Nb in $Li_5La_3M_2O_{12}$ (M = Nb, Ta) on the ionic conductivity[18,19]. This approach has decreased the ionic conductivity by several orders of magnitude compared to the parent compound since the Li ions mainly occupy the tetrahedral sites and this decreases the concentration of mobile Li ions in the structure. In the current chemical substitution approach, the concentration of Li ions in the investigated compounds is nearly the same. The decrease in conductivity seems to be attributed to oxygen vacancies in the structure. The activation energy for electrical conductivity was found to be in the

range 0.5-0.6 eV at 20-200 °C, which is in good agreement with garnet-type Li ion conductors reported in the literature[15-17].

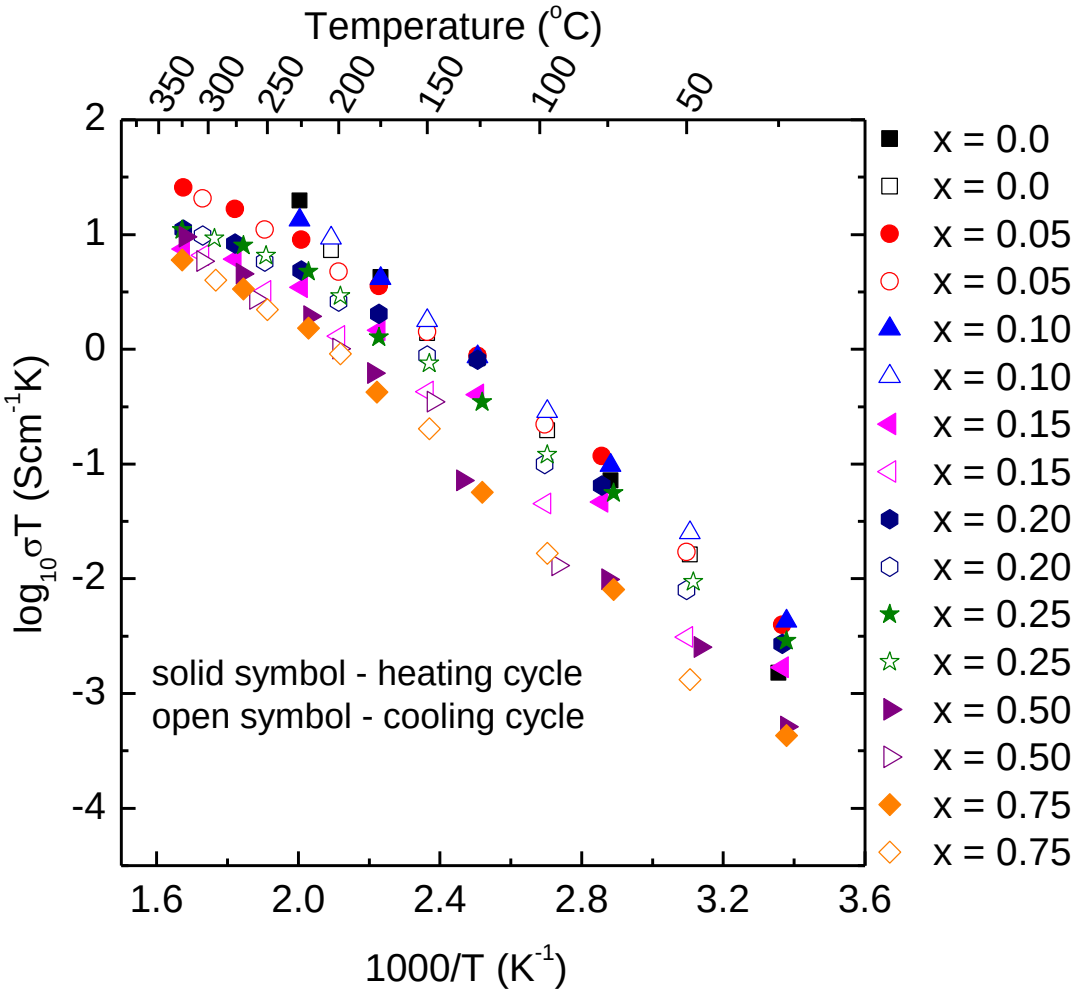

Figure 4. 11 Arrhenius plots for electrical conductivity of $Li_5La_3Nb_{2-x}Y_xO_{12-\delta}$ sintered at 1100 °C in air[2].

The electrical conductivities and activation energies of the investigated compounds are listed in Table 4.2 along with lattice constants. The Li ion diffusion coefficient (*D*) is determined from the AC electrical conductivity, using the Nernst-Einstein relation as shown in equation [4.4]:

$$\sigma(0) = \frac{q^2 N}{k_B T} \cdot D \qquad [4.4]$$

where q is the elementary charge (1. 602 x 10^{-19} C), N the concentration of charge carriers calculated according to $N = n/V$, where n is the number of Li ions per unit cell and V is the volume of the unit cell calculated from the PXRD, k_B is the Boltzmann constant (1.38 x 10^{-23} JK^{-1}), and T is the temperature. The diffusion coefficient was found to be in the order of 10^{-11}-10^{-12} cm^2s^{-1} at room temperature and is found to be two orders of magnitude lower than that of other garnet-type materials reported in the literature[7].

Table 4. 2 Electrical transport properties of $Li_5La_3Nb_{2-x}Y_xO_{12-\delta}$.

Y content (x)	$\sigma_{(23\,°C)}$ (Scm^{-1})	$\sigma_{(100\,°C)}$ (Scm^{-1})	E_a (eV)
0	5.08 x10^{-6}	5.32 x10^{-4}	0.60
0.05	1.34 x10^{-5}	5.94 x10^{-4}	0.45
0.10	1.44 x10^{-5}	7.78 x10^{-4}	0.51
0.15	5.71 x10^{-6}	1.22 x10^{-4}	0.43
0.20	9.13 x10^{-6}	2.70 x10^{-4}	0.43
0.25	9.68 x10^{-6}	3.24 x10^{-4}	0.43
0.50	1.73 x10^{-6}	3.57 x10^{-5}	0.51
0.75	1.46 x10^{-6}	4.50 x10^{-5}	0.50

In Figure 4.12, we compare the electrical conductivity of Y-doped $Li_5La_3Nb_2O_{12}$ with parent $Li_5La_3Nb_2O_{12}$, $Li_6BaLa_2Ta_2O_{12}$, $Li_7La_3Zr_2O_{12}$, and In-doped $Li_5La_3Nb_2O_{12}$[5,7,16,17]. Li concentration seems to be important for electrical conductivity at

lower temperatures, while at higher temperatures, all compounds show comparable ionic conductivity. A slight improvement in conductivity was obtained by substitution of In for Nb in the structure, which is believed to be due to small changes in Li concentration and lattice constant. Further increase in the conductivity of about 10^{-5} Scm^{-1} at 22 °C was obtained for $Li_6BaLa_2Ta_2O_{12}$. In addition, the fast conducting garnet related electrolyte with a nominal composition of $Li_7La_3Zr_2O_{12}$ has been reported with a conductivity of 10^{-4} Scm^{-1} at 25 °C. These results indicate that increase in Li concentration has a positive effect on ionic conductivity. The effect of dopant is increasing the cell constant and in turn, decreasing the interaction between Li and other ions in the structure can also be attributed to the increase in conductivity. The influence of crystal structure on the conductivity has also been shown elsewhere. For example, Akimoto et al. showed that tetragonal modification of $Li_7La_3Zr_2O_{12}$ gave a Li ion conductivity of about two orders of magnitude lower than that of the cubic phase, which is the highest ranking garnet-type solid electrolyte for Li ion batteries reported so far[4,17].

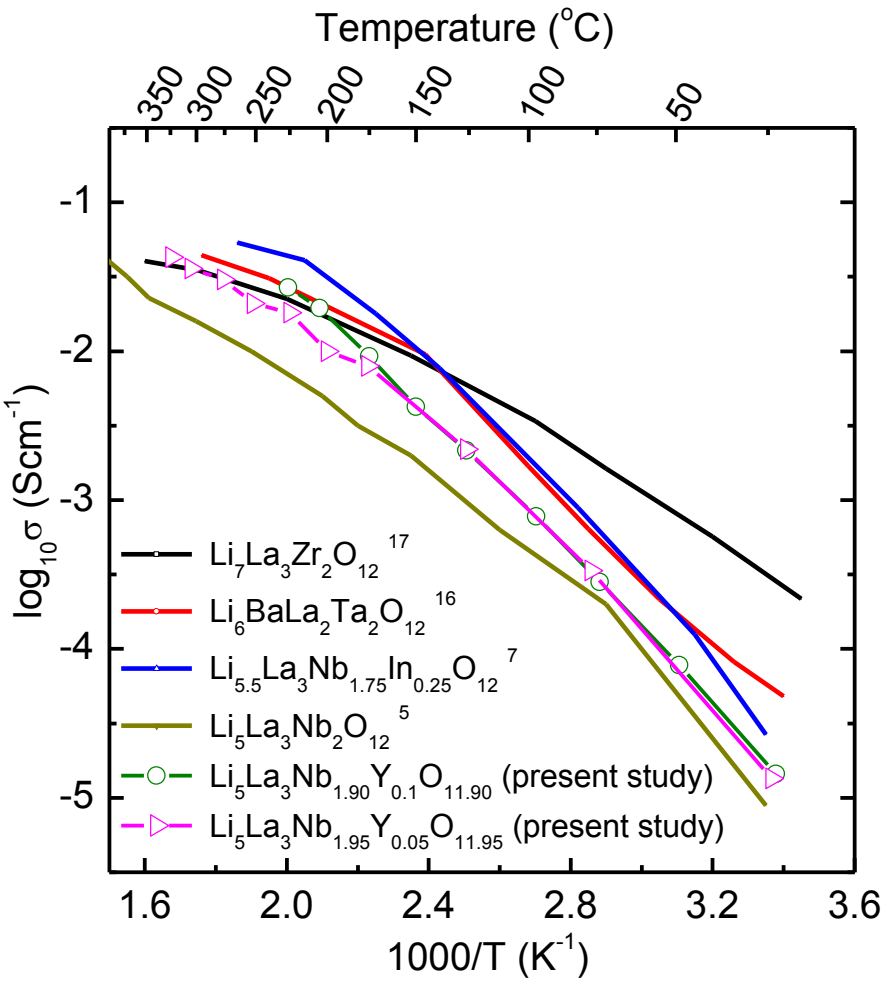

Figure 4. 12 Comparison of electrical conductivity of $Li_5La_3Nb_{1.9}Y_{0.1}O_{11.9}$ with other garnet-type solid electrolytes reported in the literature[5,7,16,17].

4.2.4 Chemical reactivity of $Li_5La_3Nb_{1.95}Y_{0.05}O_{11.95}$ with temperature and high voltage cathode material, $Li_2FeMn_3O_8$

The stability of garnet under temperatures between 30 and 325 °C was tested employing *in-situ* PXRD analysis (Figure 4.13) to give the behaviour of the sample during impedance measurements. The material is stable under the investigated temperature range.

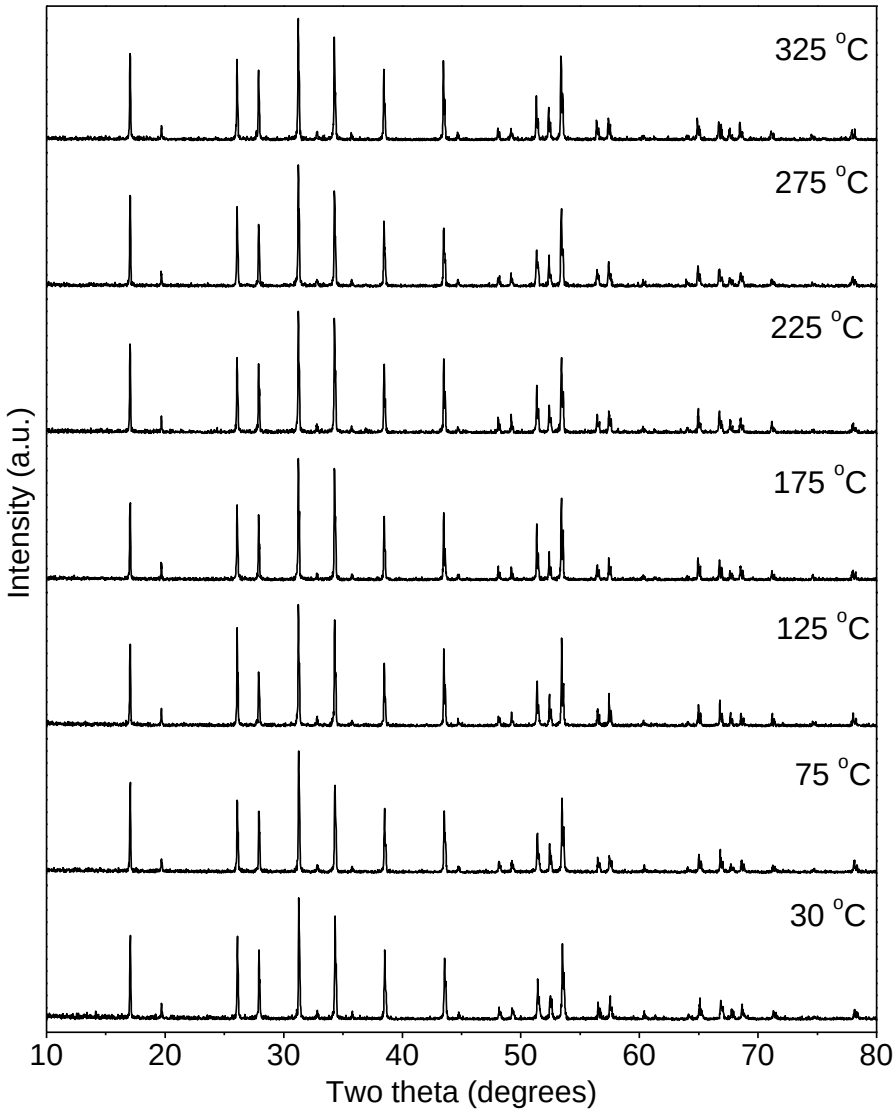

Figure 4. 13 *In-situ* powder XRD patterns showing the chemical reactivity of $Li_5La_3Nb_{1.95}Y_{0.05}O_{11.95}$ against temperature. It is stable under the temperature range used for impedance analysis.

Figure 4.14 shows the *ex-situ* PXRD patterns of $Li_5La_3Nb_{1.95}Y_{0.05}O_{11.95}$ and the cathode $Li_2FeMn_3O_8$ mixture before heat treatment and after heating at 400, 600, 800 and 900 °C for 24 h[1]. The diffraction patterns clearly indicate the garnet and spinel-type peaks up to 400 °C. Following this, the garnet-like peaks started to disappear, but those of the spinel-

type electrode are still present in all the patterns. The new peaks, which are clearly seen at 800 and 900 °C, are indexed to $LiLaNb_2O_7$ (2θ ~ 28, 33, 37, 56, 66, and 67 °; ICSD No. 00-027-1249) and $LiLa_2NbO_6$ (2θ ~ 31, 45, and 46 °; ICSD No. 00-040-0895). These results show that $Li_5La_3Nb_{1.95}Y_{0.05}O_{11.95}$ is chemically stable with the cathode $Li_2FeMn_3O_8$ up to 400 °C and is a promising electrolyte for Li ion batteries. Further electrochemical studies need to be done to confirm the range of voltage stability for this particular combination.

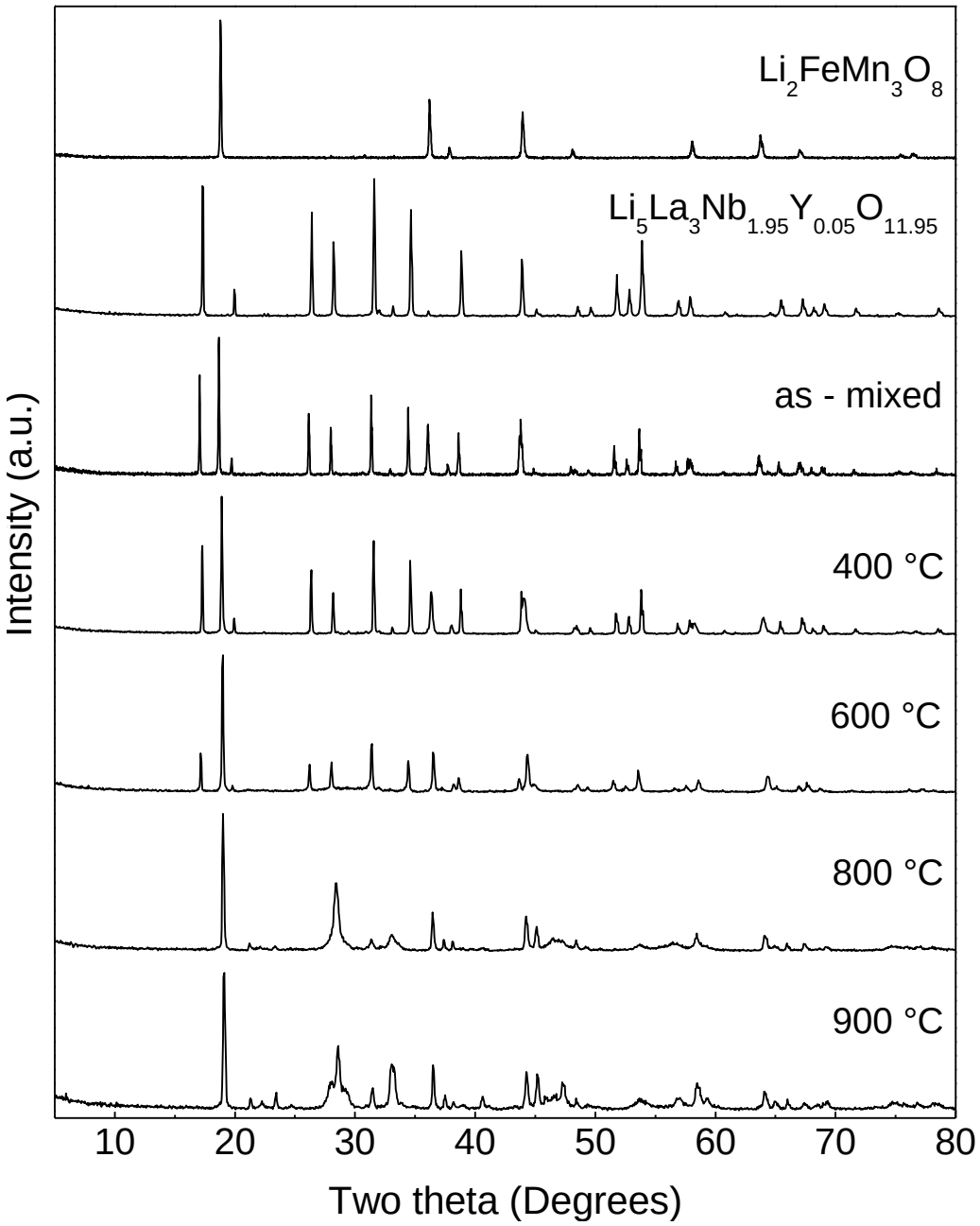

Figure 4. 14 *Ex-situ* powder XRD patterns showing the chemical reactivity of $Li_5La_3Nb_{1.95}Y_{0.05}O_{11.95}$ and the cathode $Li_2FeMn_3O_8$ as mixed and heated at 400, 600, 800 and 900 °C for 24 h in air. The garnet-like phase is stable up to 400 °C and after 600 °C they started reacting in presence of the cathode[1].

4.3 Summary

In summary, the substitution of Y for Nb in the $Li_5La_3Nb_2O_{12}$ was possible by solid state reaction at elevated temperatures. The powder X-ray diffraction study revealed a single-phase cubic garnet-type structure for x up to 0.25 in $Li_5La_3Nb_{2-x}Y_xO_{12-\delta}$ and very small amount of second phase at high Y doping. AC impedance showed bulk and grain-boundary contribution to the total electrical conductivity and is similar to other garnet-type materials reported in the literature. All the investigated Y-substituted compounds showed comparable electrical conductivity to that of the parent compound $Li_5La_3Nb_2O_{12}$. The x = 0.05 and 0.1 members of $Li_5La_3Nb_{2-x}Y_xO_{12-\delta}$ showed ionic conductivity of 1.34 x 10^{-5} and 1.44 x 10^{-5} Scm^{-1} respectively at 23 °C, which is about an order of magnitude lower than that of the fast Li ion conducting cubic $Li_7La_3Zr_2O_{12}$. The chemical reactivity of $Li_5La_3Nb_{1.95}Y_{0.05}O_{12-\delta}$ with the cathode $Li_2FeMn_3O_8$ showed that the compound is stable on heating up to 400 °C for 24 h.

Chapter Five: **The effect of Li concentration on the ionic conductivity of garnet-like $Li_{5+2x}La_3Nb_{2-x}Y_xO_{12}$**

5.1 General overview

Lithium stuffing into the garnet structure has shown to improve the ionic conductivity of garnet-like solid electrolytes for Li ion batteries[1-8]. Substitution of Y at Nb site in $Li_5La_3Nb_2O_{12}$ has resulted in the novel Li stuffed garnet-like $Li_{5+2x}La_3Nb_{2-x}Y_xO_{12}$ ($0.05 \leq x \leq 0.75$), a promising candidate as solid state electrolyte for Li ion batteries. Solid state reactions were employed for the synthesis of garnet-like $Li_{5+2x}La_3Nb_{2-x}Y_xO_{12}$ and are characterized using powder X-ray diffraction (PXRD), ^{7}Li and ^{27}Al magic angle spinning nuclear magnetic resonance (MAS NMR), scanning electron microscopy (SEM), thermo-gravimetric analysis (TGA), Fourier transform infrared (FTIR), and AC impedance spectroscopy.

Rietveld refinement with the PXRD data confirmed the formation of a cubic, garnet-like *Ia*-3*d* structure for all phases. ^{7}Li MAS NMR showed a single sharp peak close to 0 ppm as the usual trend for fast Li ion conducting garnets. Among the materials studied, $Li_{6.5}La_3Nb_{1.25}Y_{0.75}O_{12}$ showed a very high bulk ionic conductivity of 2.7×10^{-4} Scm^{-1} at 25 °C, which is the highest value found in garnet-type compounds, and is only reported for $Li_7La_3Zr_2O_{12}$. The *in-situ* PXRD measurements revealed higher structural stability (up to 400-600 °C) after water treatment as well as chemical compatibility with high voltage Li cathodes $Li_2MMn_3O_8$ (M = Co, Fe) and up to 800 °C for as-prepared aged samples. The electron probe microanalysis (EPMA) also showed non reactivity of the garnet with the electrode $Li_2FeMn_3O_8$. The current work demonstrates that slight Al

contamination from the Al_2O_3 crucible, which is commonly observed in this class of materials and was detected by ^{27}Al MAS NMR, does not affect the Li ionic conductivity and chemical stability of $Li_{5+2x}La_3Nb_{2-x}Y_xO_{12}$ garnets, and also Li stuffing is critical to improve further ionic conductivity of parent compound $Li_5La_3Nb_2O_{12}$. Y^{3+} seems to be very efficient dopant to improve ionic conductivity of garnets compared to other investigated dopants that include M^{2+} (M = alkaline earth metals), In^{3+}, and Zr^{4+}.

5.2 Results and discussion

5.2.1 Structural analysis

The preliminary analysis of PXRD data of $Li_{5+2x}La_3Nb_{2-x}Y_xO_{12}$ using the *PROSZKI* program was done and rough estimations of lattice parameters were calculated. Most of the peaks could be indexed to the cubic structure of the garnet with space group *Ia*-3*d*. The results for $Li_{5+2x}La_3Nb_{2-x}Y_xO_{12}$ (x = 0.05 and 0.10) are summarized in Table 5.1 and for the rest of the compositions (x = 0.20-0.75) are provided in Appendix B (Table B.1-B.2).

Table 5. 1 Indexed powder XRD patterns of $Li_{5+2x}La_3Nb_{2-x}Y_xO_{12}$ (x = 0.05 and 0.10) using PROSZKI program.

			x = 0.05			x = 0.10		
h	*k*	*l*	$d_{obs.}$ (Å)	$d_{cal.}$ (Å)	$I_{obs.}$ (%)	$d_{obs.}$ (Å)	$d_{cal.}$ (Å)	$I_{obs.}$ (%)
2	1	1	5.181	5.201	100	5.151	5.195	86
2	2	0	4.492	4.504	19	4.469	4.499	15
3	2	1	3.399	3.405	79	3.392	3.401	76
4	0	0	3.184	3.185	70	3.173	3.181	65
4	2	0	2.851	2.849	94	2.842	2.845	100
3	3	2	2.716	2.716	8	2.712	2.713	8
4	2	2	2.601	2.601	89	2.598	2.597	82
5	1	0	2.503	2.499	5	2.494	2.495	4
5	2	1	2.328	2.326	49	2.325	2.323	48
6	1	1	2.070	2.067	53	2.067	2.064	49
6	2	0	2.017	2.014	6	2.015	2.012	6
6	3	1	1.883	1.878	9	1.879	1.876	8
4	4	4	1.843	1.839	9	1.840	1.837	8
6	4	0	1.771	1.767	31	1.768	1.764	31
7	2	1	1.739	1.734	21	1.736	1.732	21
6	4	2	1.707	1.703	68	1.706	1.700	61
6	5	1	1.622	1.618	12	1.621	1.616	12
8	0	0	1.596	1.593	18	1.595	1.590	16
6	5	3	1.527	1.523	4	1.526	1.521	5

8	3	2	1.448	1.452	4	1.447	1.450	4
8	4	0	1.429	1.424	14	1.428	1.423	15
9	1	1	1.395	1.398	15	1.394	1.397	15
7	6	0	1.378	1.382	9	1.378	1.380	9
6	6	4	1.363	1.358	11	1.362	1.356	13
8	5	2	1.318	1.321	7	1.318	1.319	7
10	1	0	1.267	1.268	3	1.265	1.266	3
10	3	0	1.219	1.220	8	1.219	1.219	8
			12.740(4) Å			12.724(2) Å		

The *GSAS* program[9] and *EXPGUI* interface[10] were used for the Rietveld refinements that confirmed the formation of a garnet-type *Ia*-3*d* structure for all phases. The structure contains Nb(Y) atoms coordinated octahedrally by oxygen. There is no direct corner- or edge-sharing between the $Nb(Y)O_6$ octahedra. They are also tilted to the left or right relative to the unit cell axis direction, such that the titling of each octahedron is opposite to its nearest neighbor octahedra (Figure 5.1). The Li environment in the crystal structure is also shown in Figure 5.2.

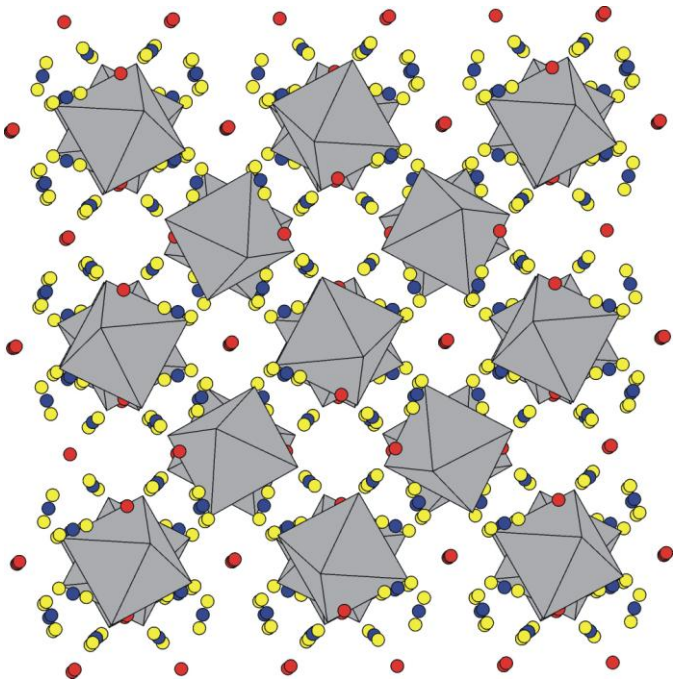

Figure 5. 1 The garnet-type structure of $Li_{5+2x}La_3Nb_{2-x}Y_xO_{12}$ showing the tilting of $Nb(Y)O_6$ octahedra (grey polyhedra). The La atoms are omitted for clarity. The red, blue and yellow spheres represent Li1 (24d site), Li2 (48g site) and Li3 (96h site), respectively. These Li positions are described in Figure 5.2.

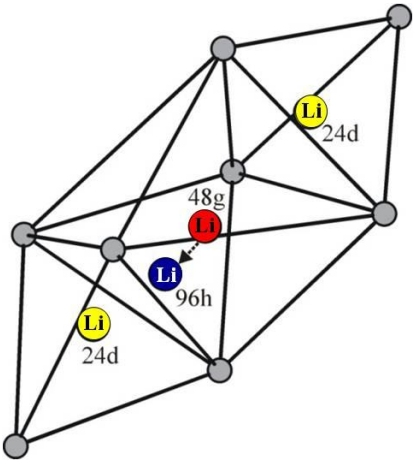

Figure 5. 2 The environment of Li atoms in the crystal structure. The smaller grey spheres are oxygen. The octahedral Li can be at the center (48g site) or shifted (96h site) towards one of the faces shared with the neighboring tetrahedron. It is important to note that the octahedral position and the two neighboring tetrahedral sites (24d) cannot be simultaneously occupied, due to electrostatic repulsion, and at least one of the three sites should be empty[11,12].

The Rietveld refined cell parameters for $Li_{5+2x}La_3Nb_{2-x}Y_xO_{12}$ phases (Figure 5.3) were found to range from 12.8169(6) to 12.9488(11) Å. These can be compared to the reported cell constants for $Li_5La_3M_2O_{12}$ (M = Nb, Ta), and $Li_7La_3Zr_2O_{12}$, and it is 12.80654(11) and 13.0035 Å, respectively[11,12]. The obtained cell parameters are consistent with the doping level and the larger ionic radius of Y^{3+} (0.90 Å) compared to those of Nb^{5+} (0.64Å), Ta^{5+}(0.64Å), and Zr^{4+}(0.72Å)[13].

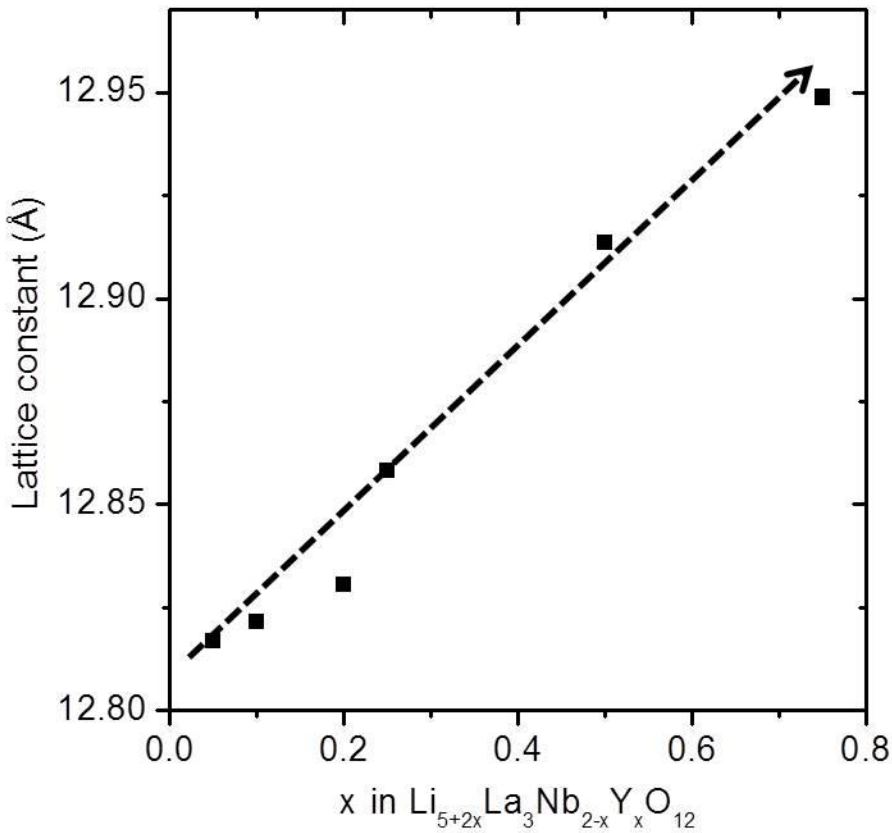

Figure 5. 3 The variation of the cell constant (Å) with the Y content in $Li_{5+2x}La_3Nb_{2-x}Y_xO_{12}$ calculated from Rietveld refinement on PXRD data.

Among the synthesized materials, the x = 0.2 and 0.75 phases show the presence of small peaks belonging to an unidentified second phase. However, these two samples

are 90-96% pure, based on an analysis where the largest second-phase peaks were fitted to Gaussian and then compared to the fitting results for the largest main phase reflections. Note that the parent compound, $Li_5La_3Nb_2O_{12}$, and also the Zr-phase, $Li_7La_3Zr_2O_{12}$, have been both reported to be accompanied by impurity phases[11,12]. For x = 0.05, 0.1, 0.25, and 0.5, very small extra peaks, barely distinguishable from the background, were observed. Figures 5.4-5.9 show the Rietveld refinement profiles for $Li_{5+2x}La_3Nb_{2-x}Y_xO_{12}$ (x=0.05-0.75), and the Tables 5.2-5.8 summarize the corresponding refined atomic parameters. The refinements were performed by placing La on a 24c site, Nb and Y on a 16a site and O on a 96h position. All refinable parameters for these atoms, even the oxygen thermal displacement factor, could be refined satisfactorily (Table 5.2-5.7). However, the quality of the refinements is affected by inherent limitations of PXRD. The Y/Nb ratios cannot be refined by PXRD and also it is obvious that a full refinement is not possible for compounds that contain lithium, as the Li parameters cannot be refined. Different Li positions have been reported for $Li_5La_3Ta_2O_{12}$, and $Li_7La_3Zr_2O_{12}$ from neutron diffraction experiments[11,12].

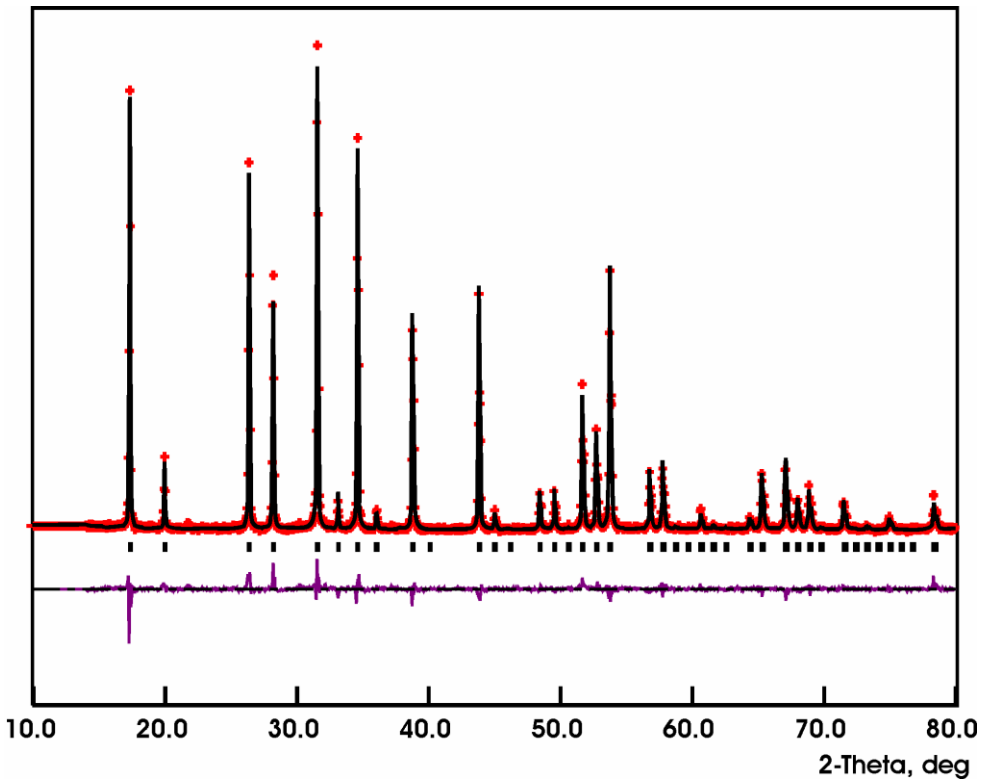

Figure 5. 4 The Rietveld refinement profile for $Li_{5.1}La_3Nb_{1.95}Y_{0.05}O_{12}$.

Table 5. 2 The powder X-ray Rietveld refinement results for $Li_{5.1}La_3Nb_{1.95}Y_{0.05}O_{12}$. The model used for the Li distribution is based on references 4 and 11. It is assumed that the excess Li is added to the 96h site.

		x	*y*	*z*	Occupancy	U_{iso}
La	24*c*	1/8	0	1/4	1	0.0213(11)
Nb	16*a*	0	0	0	0.975	0.0225(16)
Y	16*a*	0	0	0	0.025	0.0225(16)
Li1	24*d*	1/4	7/8	0	0.802	0.025
Li2	48*g*	1/8	0.6826	0.5674	0.139	0.025
Li3	96*h*	0.0927	0.684	0.5795	0.15533	0.025
O	96*h*	0.2889(8)	0.1019(8)	0.2012(9)	1	0.013(4)

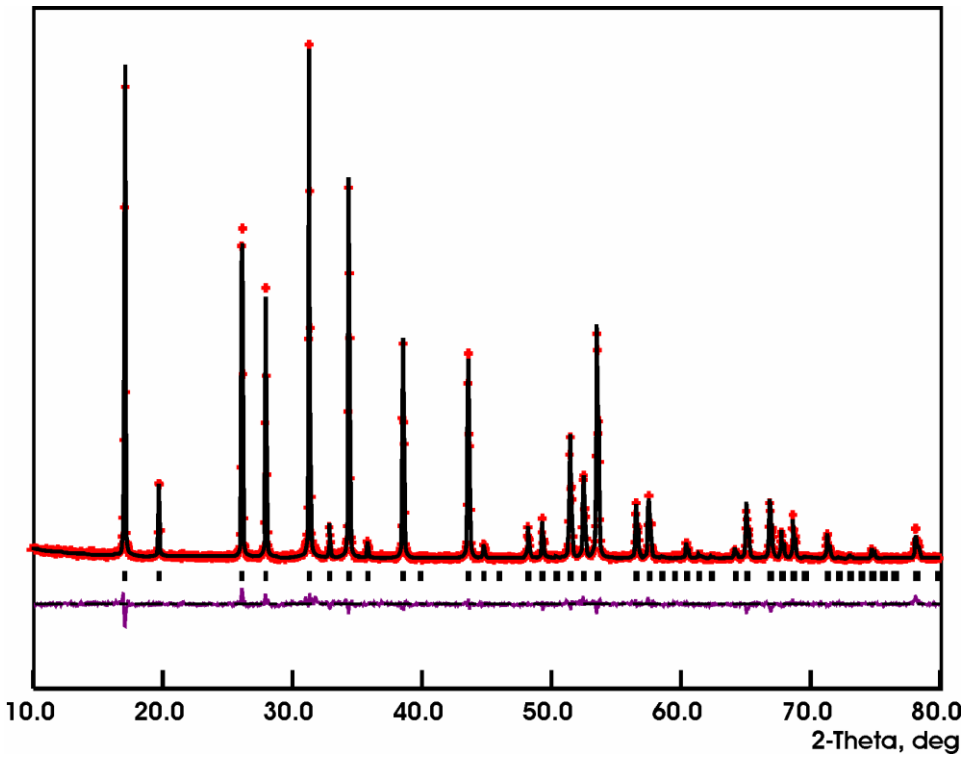

Figure 5. 5 The Rietveld refinement profile for $Li_{5.2}La_3Nb_{1.9}Y_{0.1}O_{12}$.

Table 5. 3 The powder X-ray Rietveld refinement results for $Li_{5.2}La_3Nb_{1.9}Y_{0.1}O_{12}$. The model used for the Li distribution is based on references 4 and 11. It is assumed that the excess Li is added to the 96h site.

		x	*y*	*z*	Occupancy	U_{iso}
La	24*c*	1/8	0	1/4	1	0.0219(10)
Nb	16*a*	0	0	0	0.95	0.0202(14)
Y	16*a*	0	0	0	0.05	0.0202(14)
Li1	24*d*	1/4	7/8	0	0.802	0.025
Li2	48*g*	1/8	0.6826	0.5674	0.139	0.025
Li3	96*h*	0.0927	0.684	0.5795	0.16367	0.025
O	96*h*	0.2849(7)	0.1020(7)	0.2002(8)	1	0.022(4)

As expected, the PXRD refinements gave an equally good match with the two models reported for the above materials. Nevertheless, some insight into the Li distribution can be obtained from careful examination of the available studies on garnets, such as the ones mentioned above[11,12]. In both references 11 and 12, a model with La on a 24c site, Nb, Ta or Zr on a 16a site and O on a 96h position is confirmed, but the Li distribution is different. Reference 11 shows that Li in $Li_5La_3M_2O_{12}$ (M = Nb, Ta) is disordered over three positions: tetrahedral site (24d), center of the octahedra (48g site) and shifted from the center of octahedra (96h site). The displacement of Li^+ cations from the center of octahedra is justified in terms of reduction in electrostatic repulsion and prevention of very short Li – Li distances that can occur between a Li atom on a tetrahedral site and its neighboring octahedral Li[4,11]. The high Li^+ mobility is described based on short Li^+ – Li^+ distances in the edge-sharing LiO_6 octahedra that facilitate the Li^+ conduction[11]. In reference 12, the distribution of Li over the octahedral and tetrahedral sites in $Li_7La_3Zr_2O_{12}$ is confirmed, although all octahedral Li atoms are shifted from the centre of the octahedra, and the presence of Li on the 48g position is ruled out. Therefore, the Li distribution varies in different garnet-type materials, but higher Li content and the octahedral site occupation appear to go hand in hand with high Li^+ conductivity.

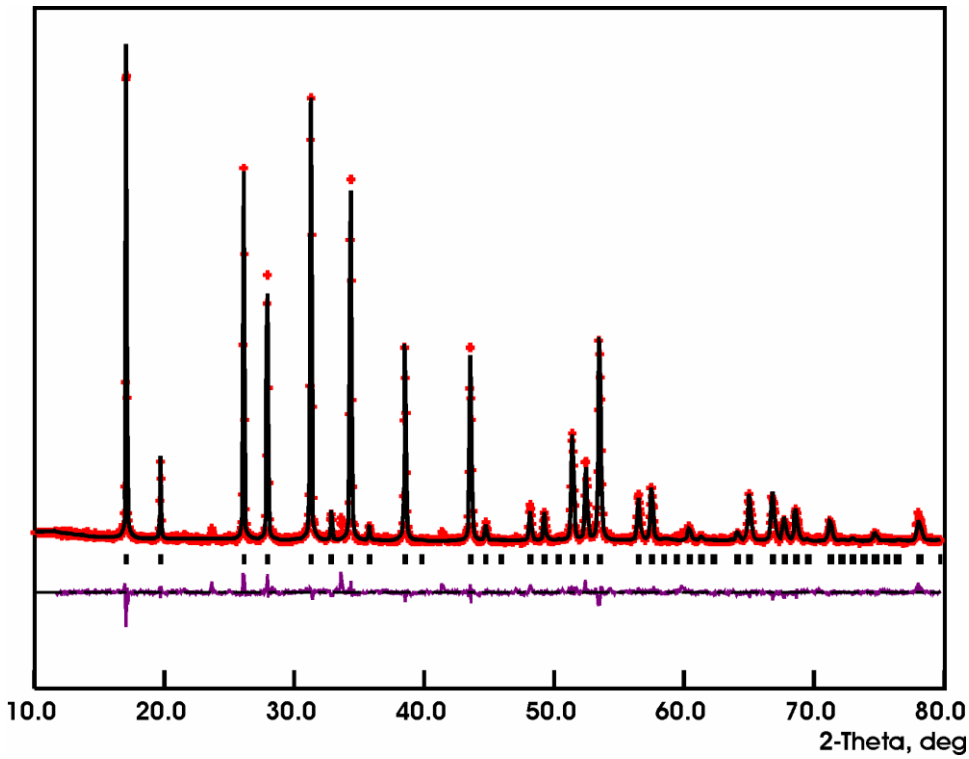

Figure 5. 6 The Rietveld refinement profile for $Li_{5.4}La_3Nb_{1.8}Y_{0.2}O_{12}$.

Table 5. 4 The powder X-ray Rietveld refinement results for $Li_{5.4}La_3Nb_{1.8}Y_{0.2}O_{12}$. The model used for the Li distribution is based on 4 and 11. It is assumed that the excess Li is added to the 96h site.

		x	*y*	*z*	Occupancy	U_{iso}
La	24*c*	1/8	0	1/4	1	0.0229(12)
Nb	16*a*	0	0	0	0.9	0.0216(18)
Y	16*a*	0	0	0	0.1	0.0216(18)
Li1	24*d*	1/4	7/8	0	0.802	0.025
Li2	48*g*	1/8	0.6826	0.5674	0.139	0.025
Li3	96*h*	0.0927	0.684	0.5795	0.18033	0.025
O	96*h*	0.2895(9)	0.1008(10)	0.1985(10)	1	0.032(5)

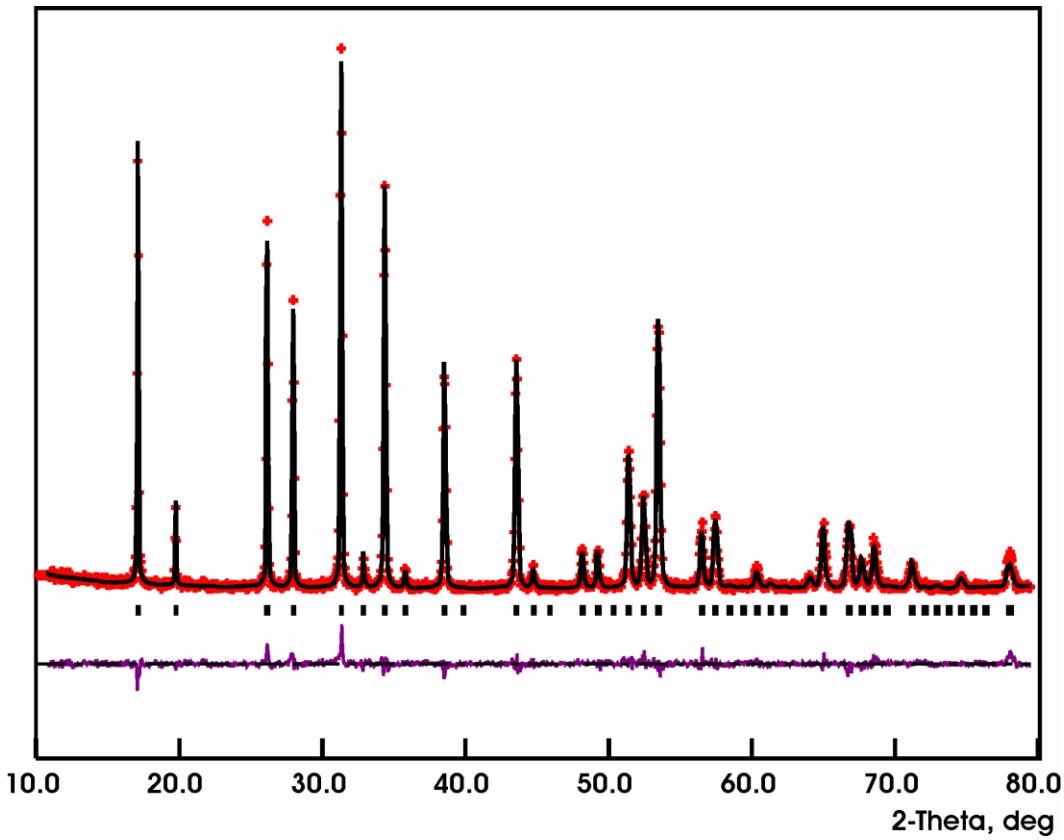

Figure 5. 7 The Rietveld refinement profile for $Li_{5.5}La_3Nb_{1.75}Y_{0.25}O_{12}$.

Table 5. 5 The powder X-ray Rietveld refinement results for $Li_{5.5}La_3Nb_{1.75}Y_{0.25}O_{12}$. The model used for the Li distribution is based on references 4 and 11. It is assumed that the excess Li is added to the 96h site.

		x	*y*	*z*	Occupancy	U_{iso}
La	24*c*	1/8	0	1/4	1	0.0151(12)
Nb	16*a*	0	0	0	0.875	0.0218(18)
Y	16*a*	0	0	0	0.125	0.0218(18)
Li1	24*d*	1/4	7/8	0	0.802	0.025
Li2	48*g*	1/8	0.6826	0.5674	0.139	0.025
Li3	96*h*	0.0927	0.684	0.5795	0.18867	0.025
O	96*h*	0.2849(9)	0.1036(9)	0.1973(10)	1	0.006(4)

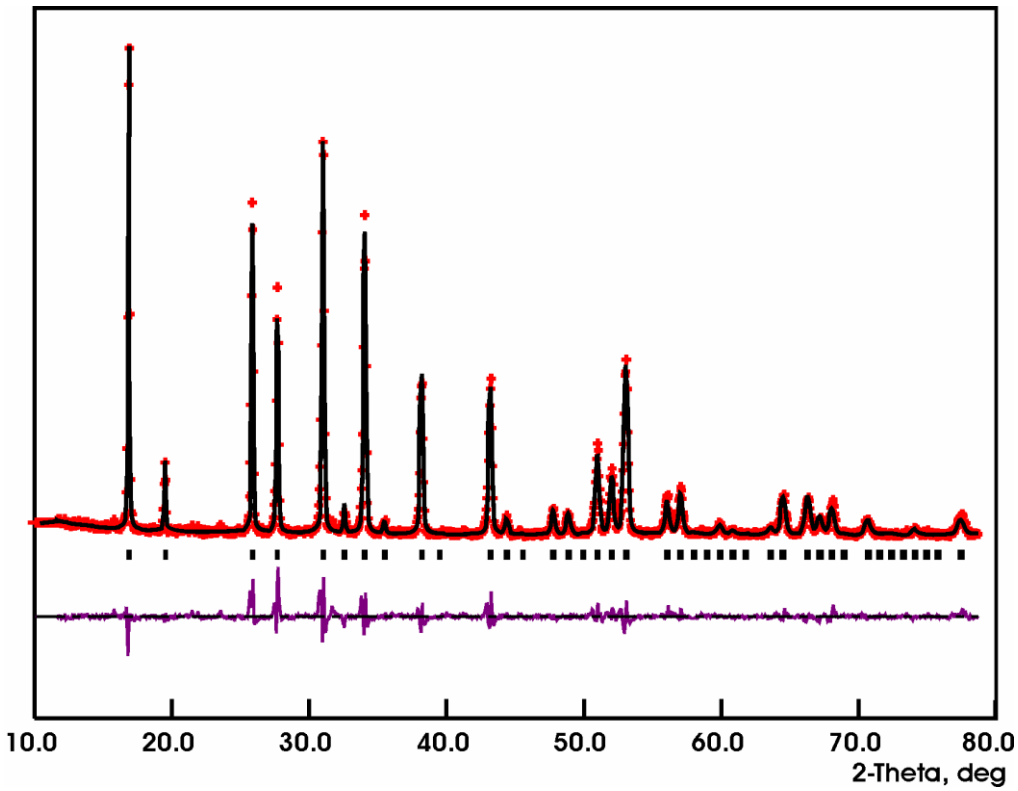

Figure 5. 8 The Rietveld refinement profile for $Li_6La_3Nb_{1.5}Y_{0.5}O_{12}$.

Table 5. 6 The powder X-ray Rietveld refinement results for $Li_6La_3Nb_{1.5}Y_{0.5}O_{12}$. (*The Li position and occupancies are taken from reference 4, where these parameters are refined using neutron diffraction data for $Li_6BaLa_2Ta_2O_{12}$).

		x	*y*	*z*	Occupancy	U_{iso}
La	24*c*	1/8	0	1/4	1	0.028(6)
Nb	16*a*	0	0	0	0.75	0.027(6)
Y	16*a*	0	0	0	0.25	0.027(6)
Li1*	24*d*	1/4	7/8	0	0.674	0.030
Li2*	48*g*	1/8	0.6773	0.5727	0.220	0.030
Li3*	96*h*	0.0937	0.6888	0.5817	0.218	0.030
O	96*h*	0.2883(8)	0.1009(8)	0.1969(8)	1	0.029(7)

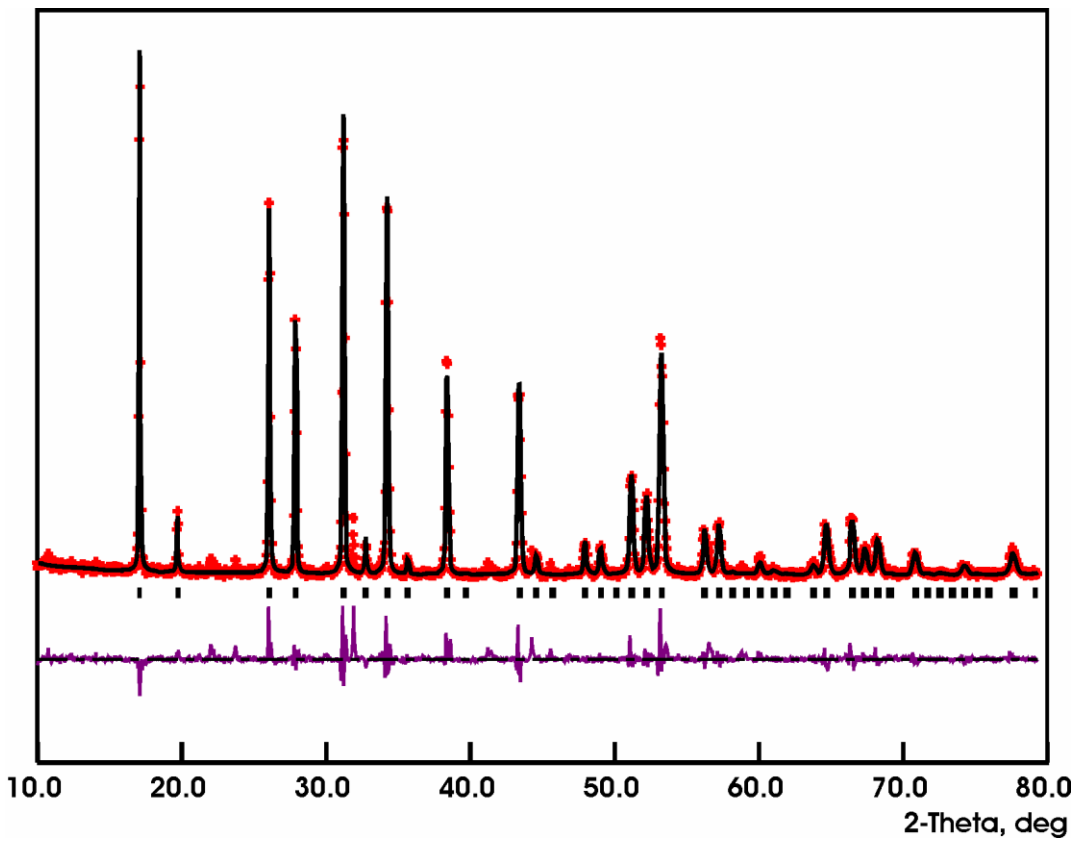

Figure 5. 9 The Rietveld refinement profile for $Li_{6.5}La_3Nb_{1.25}Y_{0.75}O_{12}$.

Table 5. 7 The powder X-ray Rietveld refinement results for $Li_{6.5}La_3Nb_{1.25}Y_{0.75}O_{12}$. The Li occupancies are taken from reference 4, where different Li site occupancies are plotted against the Li content per formula unit.

		x	*y*	*z*	Occupancy	U_{iso}
La	24*c*	1/8	0	1/4	1	0.0212(14)
Nb	16*a*	0	0	0	0.625	0.0184(21)
Y	16*a*	0	0	0	0.375	0.0184(21)
Li1	24*d*	1/4	7/8	0	0.545	0.025
Li2	48*g*	1/8	0.6826	0.5674	0.2625	0.025
Li3	96*h*	0.0927	0.684	0.5795	0.27417	0.025
O	96*h*	0.2892(10)	0.0981(11)	0.1968(11)	1	0.024(5)

Table 5. 8 The inter-atomic distances of $Li_{5+2x}La_3Nb_{2-x}Y_xO_{12}$ calculated from the Rietveld refinement and the agreement factors indicating the goodness of fit.

Compound	Interatomic distances (Å)			Agreement factors	
	La-O x 4	La-O x 4	Nb(Y)-O x 6	R_p (%)	R_{wp}
$Li_{5.1}La_3Nb_{1.95}Y_{0.05}O_{12}$	2.551(10)	2.643(11)	2.060(11)	9.05	0.1237
$Li_{5.2}La_3Nb_{1.9}Y_{0.1}O_{12}$	2.514(9)	2.622(10)	2.052(10)	7.78	0.1113
$Li_{5.4}La_3Nb_{1.8}Y_{0.2}O_{12}$	2.562(12)	2.615(13)	2.087(13)	10.33	0.1419
$Li_{5.5}La_3Nb_{1.75}Y_{0.25}O_{12}$	2.542(11)	2.590(12)	2.050(12)	8.46	0.1161
$Li_6La_3Nb_{1.5}Y_{0.5}O_{12}$	2.572(9)	2.610(10)	2.103(11)	9.64	0.1460
$Li_{6.5}La_3Nb_{1.25}Y_{0.75}O_{12}$	2.571(13)	2.622(14)	2.145(15)	10.33	0.1419

In $Li_{5+2x}La_3Nb_{2-x}Y_xO_{12}$, a high Li occupation on the octahedral sites might be expected and could increase the Li^+ conduction. Note that the garnet-type compound $Li_3Nd_3Te_2O_{12}$[14], with Li located exclusively on the tetrahedral site has a low Li^+ conductivity. Another observation is an inverse correlation between the total Li content and the tetrahedral site occupation demonstrated for the garnet type compounds $Li_{5+x}Ba_xLa_{3-x}Ta_2O_{12}$ (x = 0-1.6)[4]. Also, in these materials, the concentration of Li atoms displaced from the octahedral center increases almost linearly, as the total Li concentration increases in the composition[4]. Based on these correlations[4], the Li distribution in our highly conducting $Li_{6.5}La_3Nb_{1.25}Y_{0.75}O_{12}$ phase can be estimated as 25% on the tetrahedral site (24d), 24% at the octahedral centre (48g site), and 51% shifted from the center of octahedra (96h site). Additionally, in reference 12 an ordering of 24d site vacancies is suggested when the total Li content is ≥ 6.5 per formula unit. It is

also proposed that the highest Li^+ conductivity should occur in a composition with Li concentration of 6.4±1 per formula unit[12]. This prediction is in accordance with the highest Li^+ mobility in garnets, observed in our $Li_{6.5}La_3Nb_{1.25}Y_{0.75}O_{12}$ phase, although the conductivity of $Li_7La_3Zr_2O_{12}$ is also very close to our phase[12]. It is also notable that in an earlier work on $Li_{5+x}Ba_xLa_{3-x}Ta_2O_{12}$ (x = 0-2)[5], the highest bulk and total (bulk + grain-boundary) conductivity has been observed for the x = 1.25 phase (and not x = 1.5).

Regarding the Nb/Y ratios in $Li_{5+2x}La_3Nb_{2-x}Y_xO_{12}$ series, useful information can be obtained from the interatomic distances. For the previously studied material, $Li_5La_3Ta_2O_{12}$[11], the TaO_6 octahedron bond length, calculated based on the reported atomic positions, is Ta–O = 1.9974 Å. This value is very close to the sum of the ionic radii of Ta^{5+} (0.64 Å) and O^{2-} (1.40Å). Similar situation applies to $Li_7La_3Zr_2O_{12}$[12], where calculation of bond distances using the reported atomic positions gives Zr–O = 2.0809 Å, which corresponds closely to the sum of the radii for Zr^{4+} (0.72 Å) and O^{2-} (1.40 Å). Based on these observations, the interatomic distances obtained from the Rietveld refinements for $Li_{5+2x}La_3Nb_{2-x}Y_xO_{12}$ can be used to estimate the average ionic radius on the site occupied jointly by Nb^{5+} (0.64 Å) and Y^{3+} (0.900 Å). This information is then correlated with the Nb^{5+}/Y^{3+} ratio and is required to give that average radius. Such analyses are most useful for the x = 0.5 and x = 0.75 phases, where the doping level is significant and the effect on the bond distances is more pronounced. For the x = 0.5 compound, Nb(Y)–O = 2.103(11) Å that requires an estimated radius of 0.703±0.011 Å for the Nb(Y) site. This is nicely consistent with the theoretical radius of 0.705 Å, for 75% Nb^{5+} and 25% Y^{3+} on that site (Nb^{5+}/ Y^{3+}= 1.5/0.5). Also, for the x = 0.75 phase,

Nb(Y)–O = 2.145(15) Å suggesting an ionic radius of 0.745±0.015 Å, that matches the ideal value of 0.738 Å for Nb^{5+}/Y^{3+} = 1.25/0.75.

Further information on the cation occupancies can also be obtained using bond valence sum (BVS) calculations[15]. Note that the parameters used for the BVS calculations are specific to the ions involved in a particular bond. Therefore, caution is required when dealing with the atomic positions occupied jointly by two different ions. To avoid prejudgment about the cation ratios, the analyses performed here are the reverse of the conventional BVS calculation (that uses bond distances to calculate the bond valence). The argument used here is that interatomic distance generated by BVS method will match the observed bond distances from the Rietveld refinements, only if the bond valences used as input are correct. For example, for the x = 0.5 phase, the input bond valence sum was 4.5 that corresponds to the ideal ratio Nb^{5+}/ Y^{3+} = 1.5/0.5. The other input parameters required for the BVS analyses were calculated in a similar manner, based on the above Nb^{5+}/ Y^{3+} ratio. The interatomic distances extracted from the BVS method were then compared against the distances from the Rietveld refinements and a nice match was observed. For the x = 0.5 phase, the bond distance calculated using BVS method, was Nb(Y)–O = 2.0444 Å which is close to the observed value, Nb(Y)–O = 2.103(11) Å. Similar calculations for the x = 0.75 phase gave Nb(Y)–O = 2.0791 Å, as compared to the observed distance of Nb(Y)–O = 2.145(15) Å. Therefore, the BVS calculation results are also consistent with the nominal cation ratios in these materials.

5.2.2 ^{27}Al and ^{7}Li MAS NMR and SEM studies

As the preparation process involved the use of alumina crucibles, in order to check the possibility of Al impurity[8,16], the ^{27}Al NMR is also recorded and the data is provided in Figure 5.10. Surprisingly, we see a chemical shift value (δ) close to 15 ppm which indicates an octahedrally coordinated Al and one which is greater than 70 ppm and indicative of a tetrahedrally coordinated Al. It is known that α-Al_2O_3 shows an NMR peak with δ in the range of 13 to 17 ppm, and θ-Al_2O_3 shows two peaks centered at 11(1) and 80(1) ppm as it has equal number of octahedral and tetrahedral sites[10]. The possible peaks which can be seen due to the transformation of γ-AlOOH at higher temperature to γ-Al_2O_3 are at 12 and 70 ppm and for α-Al_2O_3, between 5 and 9 ppm[17,18]. The presence of a peak at ~ 80 ppm is also reported by Geiger et al. for Al-doped $Li_7La_3Zr_2O_{12}$[16]. At lower concentrations of Y in $Li_{5+2x}La_3Nb_{2-x}Y_xO_{12}$, the peak close to 13 ppm is visible, while at higher concentrations of Y only the peak close to 80 ppm is seen. The concentration of Al in garnet was found to be rather negligible compared to the doping level.

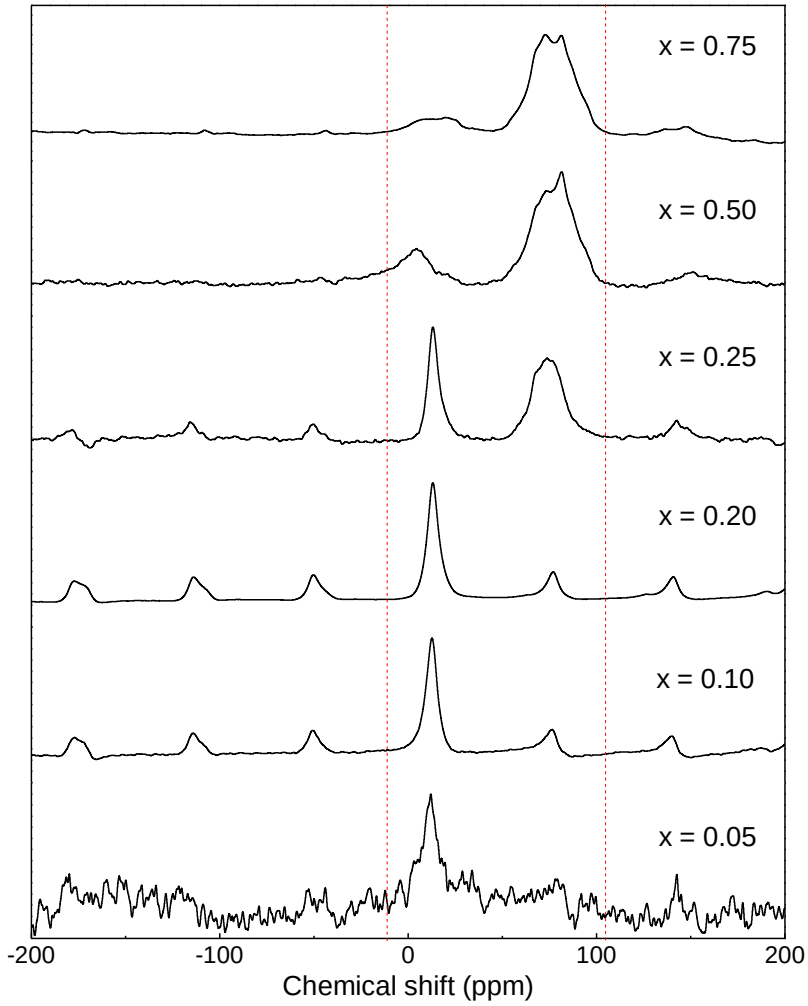

Figure 5. 10 ^{27}Al MAS NMR of $Li_{5+2x}La_3Nb_{2-x}Y_xO_{12}$ measured at a spinning frequency of 5 kHz. The chemical shift values are expressed with respect to $Al(NO_3)_3$.

Figure 5.11 shows the SEM images of the as prepared garnets $Li_{5+2x}La_3Nb_{2-x}Y_xO_{12}$. The samples were cut into small discs using the diamond saw for the measurements. The grains are clearly visible at lower Y dopant concentrations, whereas it is not distinguishable at higher doping level.

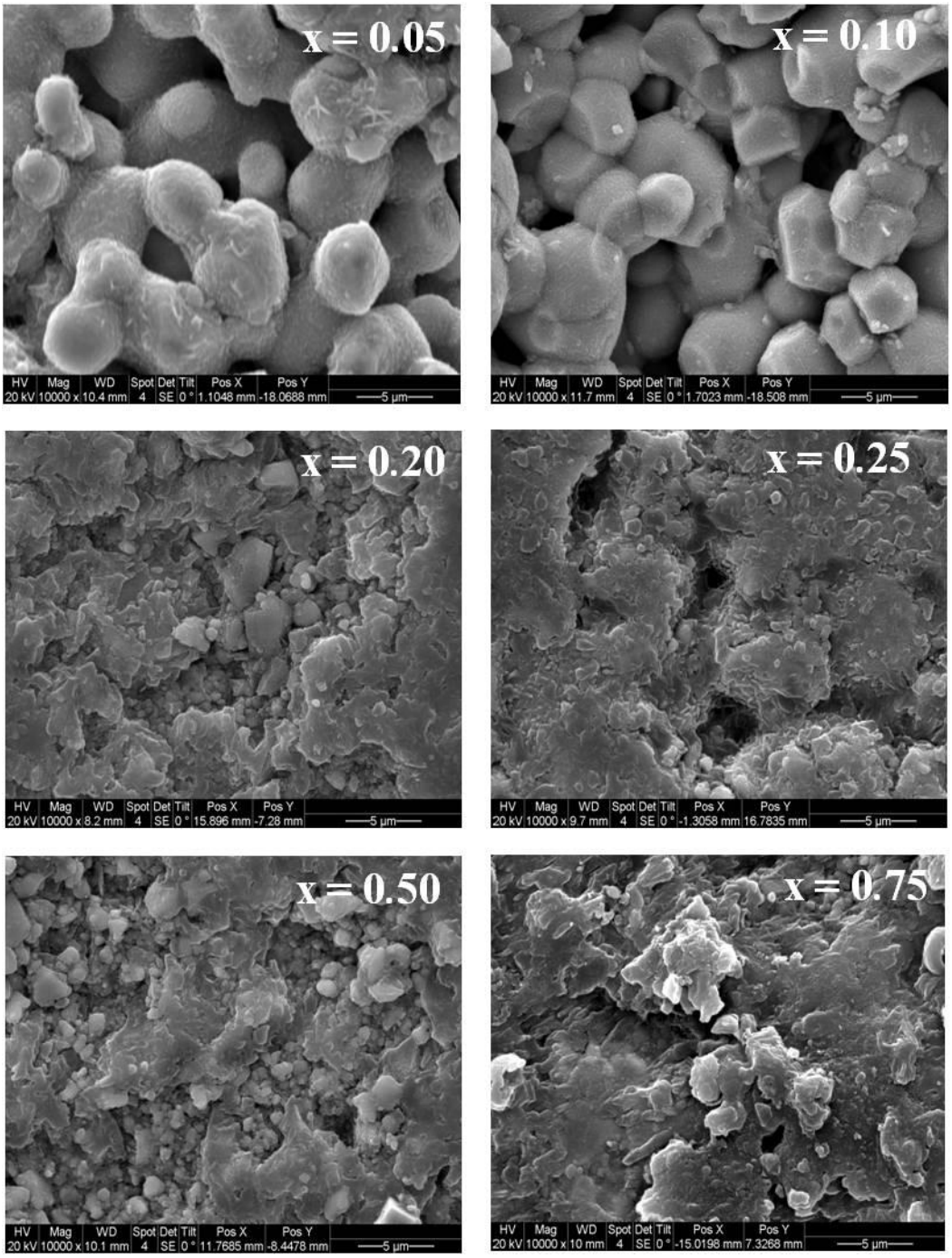

Figure 5. 11 Typical SEM images of $Li_{5+2x}La_3Nb_{2-x}Y_xO_{12}$.

The ^{7}Li MAS NMR measured using the reference LiCl is shown in Figure 5.12. A single peak close to 0 ppm was obtained in all cases which is characteristic of the garnet-

like compounds reported elsewhere[19-23]. Li ion mobility is directly proportional to the narrowness of the peak. Therefore, a narrower peak indicates a higher Li ion mobility.

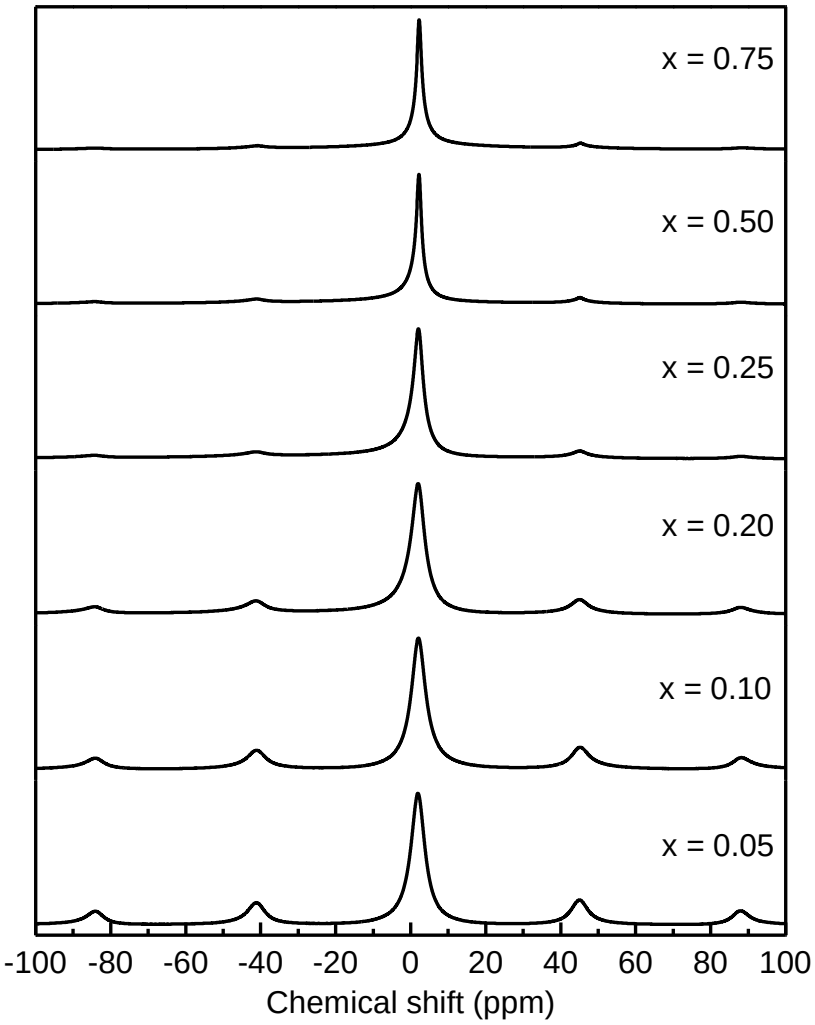

Figure 5. 12 ^{7}Li MAS NMR of $Li_{5+2x}La_3Nb_{2-x}Y_xO_{12}$ measured at a spinning frequency of 5 kHz. The chemical shift values are expressed with respect to solid LiCl.

5.2.3 Thermogravimetric analysis and FTIR spectroscopy

The thermal stability of as-prepared $Li_{5+2x}La_3Nb_{2-x}Y_xO_{12}$ garnets during the first heating and cooling cycles is shown in Figure 5.13. In all cases, the weight loss started at

~ 250 °C and ended at ~ 600 °C for the first run which may be due to uptake of water and Li_2CO_3 formation upon exposure to ambient air as shown in Figure 5.13. The weight loss in this region is due to the loss of chemically bonded water to the crystalline lattice[23]. Very interestingly, the weight loss decreased (from ~ 8 to 2 %) with increase in Li content.

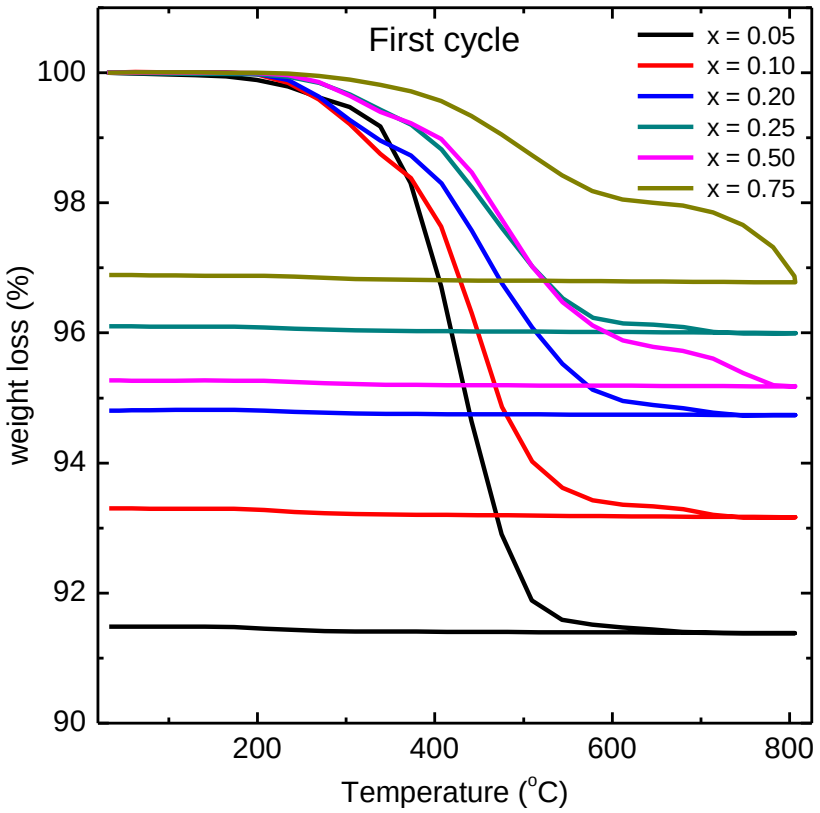

Figure 5. 13 Thermogravimetric analysis (TGA) of as prepared $Li_{5+2x}La_3Nb_{2-x}Y_xO_{12}$ (x = 0.05 to 0.75) garnets (First cycle).

Only single step weight loss is visible for the $Li_{5+2x}La_3Nb_{2-x}Y_xO_{12}$ phases with $x \leq 0.25$. Exceptionally, for the high lithium containing garnets, $Li_6La_3Nb_{1.5}Y_{0.5}O_{12}$ and $Li_{6.5}La_3Nb_{1.25}Y_{0.75}O_{12}$, an additional weight loss of 0.5 and 1 %, respectively, was

observed after treatment at 600 °C. The second cycle was carried out to show that the material is stable upon heat treatment of 800 °C and is provided in Figure 5.14. As expected, no weight loss was observed in the second run.

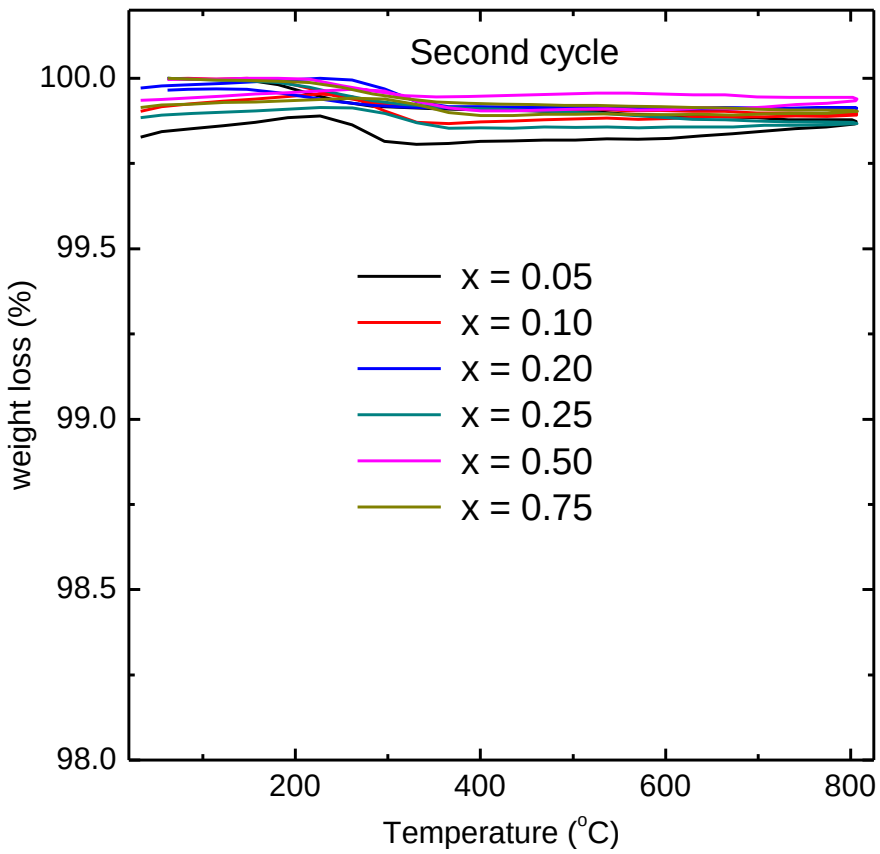

Figure 5. 14 Thermogravimetric analysis (TGA) of as prepared $Li_{5+2x}La_3Nb_{2-x}Y_xO_{12}$ (x = 0.05 to 0.75) garnets (Second cycle).

Figure 5.15 shows the FTIR spectra of $Li_{5+2x}La_3Nb_{2-x}Y_xO_{12}$ and peak corresponding to –OH band at 3300-3600 cm^{-1} is visible in all the patterns, which supports the TGA results.

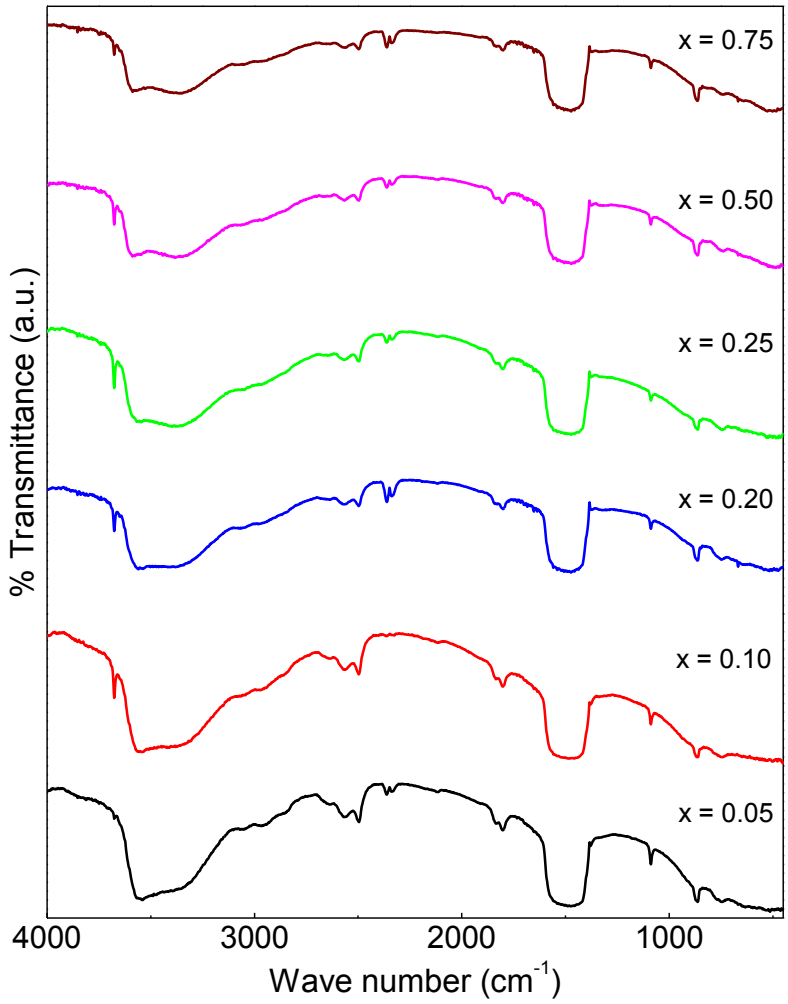

Figure 5. 15 FTIR spectra of as prepared $Li_{5+2x}La_3Nb_{2-x}Y_xO_{12}$ (x = 0.05 to 0.75) garnets.

5.2.4 AC impedance spectroscopy and electrical properties

The effect of Li concentration on the ionic conductivity is studied using the impedance spectroscopy. Figures 5.16 and 5.17 show typical AC-impedance plots of $Li_{6.5}La_3Nb_{1.25}Y_{0.75}O_{12}$ measured below the room temperature (at -53 °C, and -40 °C, respectively). Solid lines show fits using the equivalent circuit containing individual resistances and constant phase elements (CPEs), representing the electrical bulk, grain-

boundary and electrode responses and is shown as insets of Figures 5.16 and 5.17. The equation used to calculate the capacitance (C) value is given in equation [5.1] [24].

$$C = R^{\left(\frac{1-n}{n}\right)} Q^{\left(\frac{1}{n}\right)} \qquad [5.1]$$

Where R is the resistance, Q is the constant phase element and n is a parameter that has a value close to one. The capacitance C for the high-frequency semicircle is found to be in the order of 10^{-11} F, indicating bulk contribution and the semicircle appearing at intermediate frequencies with a capacitance in the order of 10^{-9} F (Table 5.8) indicates grain-boundary contribution[2,25,26]. The χ^2 values obtained were very low, ~ 10^{-3}, indicating reasonably good fits.

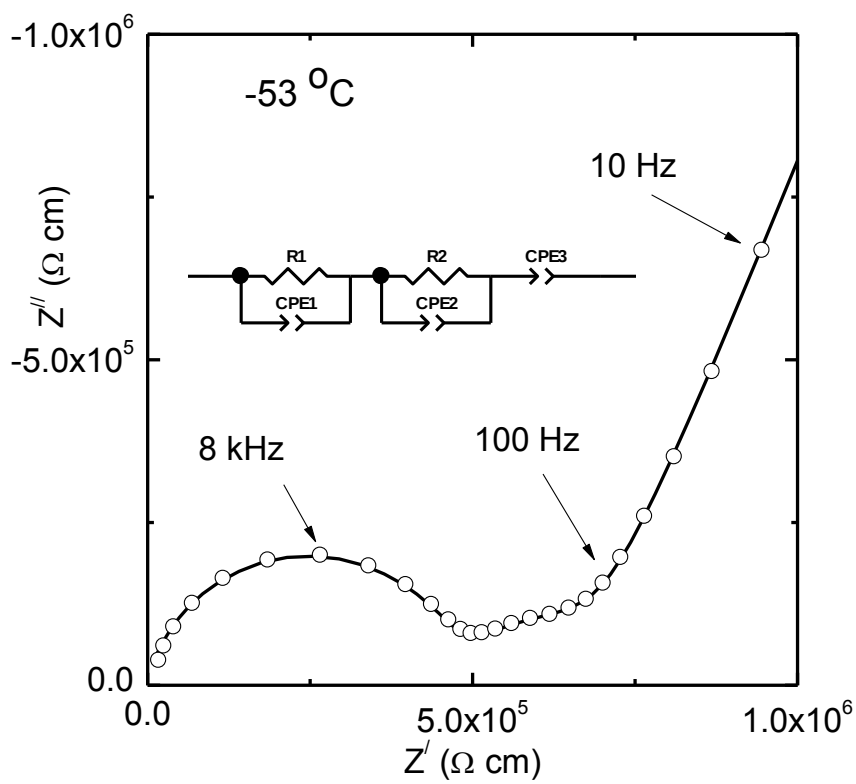

Figure 5. 16 Typical AC-impedance plot of $Li_{6.5}La_3Nb_{1.25}Y_{0.75}O_{12}$ measured at -53 °C. Solid line shows fitting using the equivalent circuit (inset) containing individual resistances and constant phase elements (CPEs) which represent the electrical bulk, grain-boundary and electrode responses. The χ^2 values obtained were very low, ~ 10^{-3}, showing reasonably good fits.

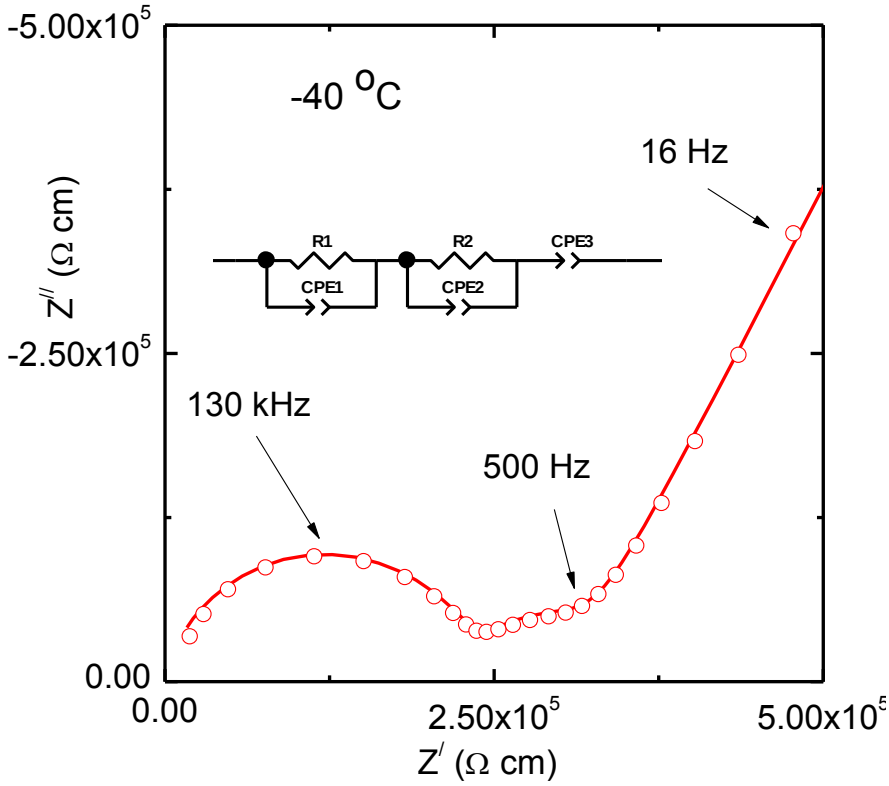

Figure 5. 17 Typical AC-impedance plot of $Li_{6.5}La_3Nb_{1.25}Y_{0.75}O_{12}$ measured at -40 °C. Solid line shows fitting using the equivalent circuit (inset) containing individual resistances and constant phase elements (CPEs) which represent the electrical bulk, grain-boundary and electrode responses. The χ^2 values obtained were very low, ~ 10^{-3}, showing reasonably good fits.

Table 5. 9 Fitting results of the analysis of the AC-impedance data (Figures 5.16 and 5.17) by using suitable equivalent circuit elements.

T (°C)	R_b (Ω)	CPE_b (F)	C_b (F)	R_{gb} (Ω)	CPE_{gb} (F)	C_{gb} (F)	χ^2
-53	1.66×10^5	7.59×10^{-11}	1.42×10^{-11}	6.93×10^5	3.22×10^{-8}	3.99×10^{-9}	0.0012
-40	8.26×10^4	1.23×10^{-10}	1.40×10^{-11}	2.42×10^4	1.59×10^{-8}	4.94×10^{-9}	0.0011

The dependence of $\sigma(\omega)$ on frequency is expressed by the following power law expression[30,31]:

$$\sigma(\omega) = \sigma(0) + A\omega^{p} \qquad [5.2]$$

where σ(0) represents the DC-conductivity, *A* is a constant, and *p* is the power law exponent (shows values between 0.7-0.8). Figure 5.18 shows the impedance analysis of $Li_{6.5}La_3Nb_{1.25}Y_{0.75}O_{12}$, measured at 25, 50 and 75 °C. Solid lines represent a rough analysis of the data using a power law, equation [5.2], and Table 5.10 summarizes the parameters derived from the fitting. A few examples are also provided for comparison[27-29]. A plateau is observed at higher frequencies (10^4 to 10^6 Hz) indicating the frequency independent nature of the conductivity and the so called dispersive AC-conductivity region. After this range, the polarization effects due to ion blocking electrodes arise and frequency dependency of the conductivity is clearly visible (Figure 5.18).

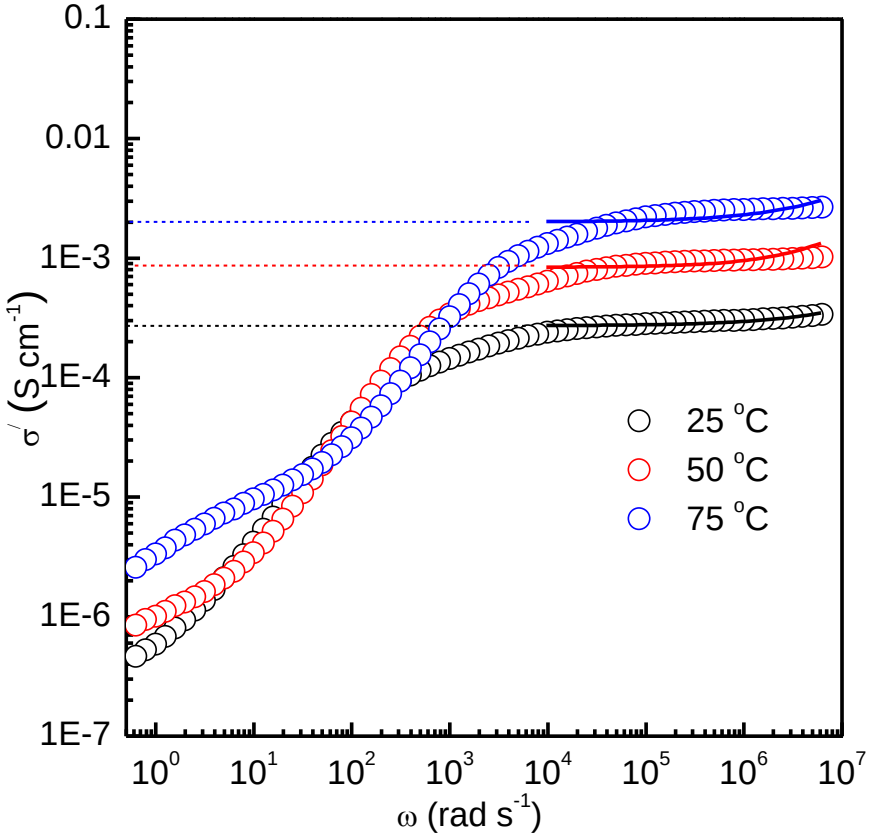

Figure 5. 18 Impedance data of $Li_{6.5}La_3Nb_{1.25}Y_{0.75}O_{12}$ measured at the temperatures indicated. Solid lines represent a rough analysis of the data using a power law expression (see equation [5.2], and Table 5.10). The frequency range used for power law fit is 10^4-10^6 Hz.

The *p* values for ionic conductors are generally between 1 and 0.5 indicating the long-range and tortuous pathways, respectively[31]. Experimental limitations in the access of dispersive region should be taken into account and hence the power law exponents have to be considered as rough estimations. However, the values obtained are in agreement with results reported for structurally disordered materials[28,29,32].

Table 5. 10 Fitting parameters obtained from the frequency-independent plateaus (10^4 to 10^6 Hz) of the impedance spectra for $Li_{6.5}La_3Nb_{1.25}Y_{0.75}O_{12}$ provided in Figure 5.18.

Compound	T (°C)	$\sigma(0)$ (S cm^{-1})	p	Reference
$Li_{6.5}La_3Nb_{1.25}Y_{0.75}O_{12}$	25	2.7×10^{-4}	0.65	present work
	50	8.3×10^{-4}	0.80	
	75	1.2×10^{-3}	0.68	
$Li_7La_3Zr_2O_{12}$ (tetragonal)	27	1.2×10^{-6}	0.77 (<- 135 °C)	27
$Li_{0.18}La_{0.61}TiO_3$	30	1.0×10^{-4}	0.60	23
Li_4SiO_4	123	4.0×10^{-8}	0.68	22

Arrhenius plots of $Li_{5+2x}La_3Nb_{2-x}Y_xO_{12}$ are shown in Figure 5.19. The electrical conductivity increases with increasing temperature and follows semiconducting behavior. A highest conductivity of 10^{-4} Scm^{-1} was observed for both $Li_{6.5}La_3Nb_{1.25}Y_{0.75}O_{12}$ and $Li_6La_3Nb_{1.5}Y_{0.5}O_{12}$ at 24 °C.

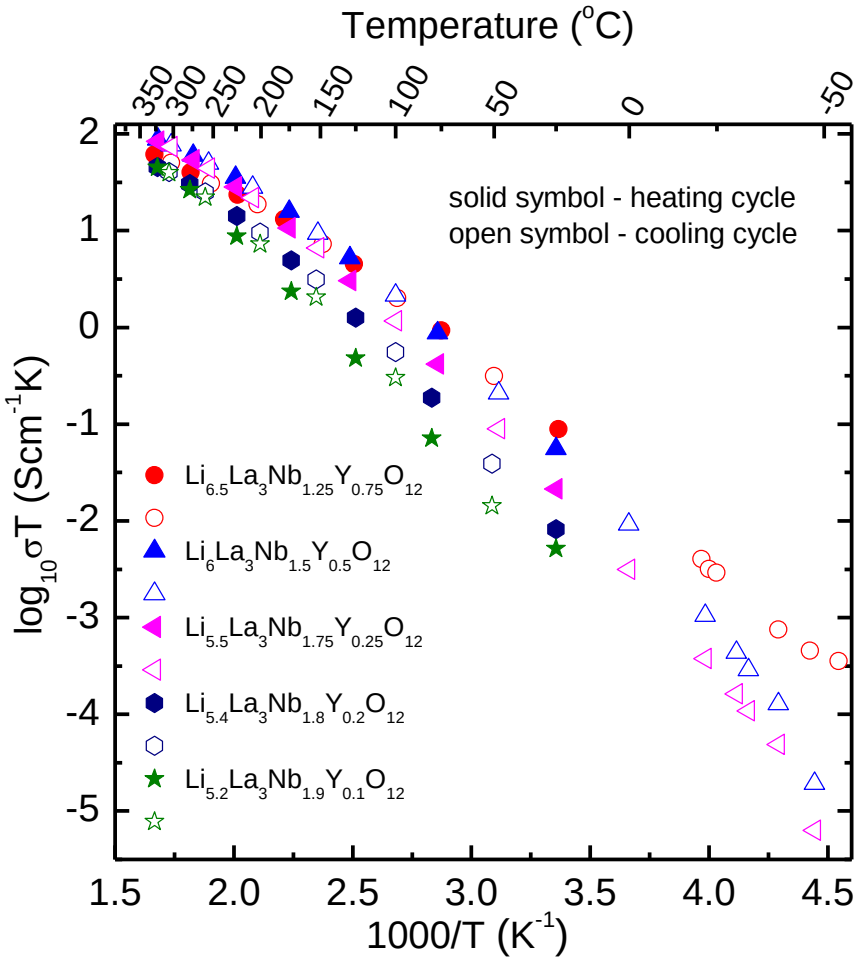

Figure 5. 19 Arrhenius plots of $Li_{5+2x}La_3Nb_{2-x}Y_xO_{12}$ (x = 0.1 to 0.75) at different temperatures ranging between -53 and 330 °C. The solid and open symbols represent heating and cooling cycle data, respectively.

The diffusivity (*D*) of Li ions can be calculated using the equation [4.4], and was found to fall in the range of 10^{-10} to 10^{-8} cm^2s^{-1} at 25-100 °C. Previous studies have revealed that the diffusivity (self-diffusion coefficient) calculated from NMR are in good agreement with that of the impedance analysis[8,27]. A comparison of changes in conductivity (σ) and diffusivity (*D*) of $Li_{5+2x}La_3Nb_{2-x}Y_xO_{12}$ at 25 °C with change in Li

concentration in the formula unit is provided in Figure 5.20. As expected, both the σ and D increase with Li concentration[20,21].

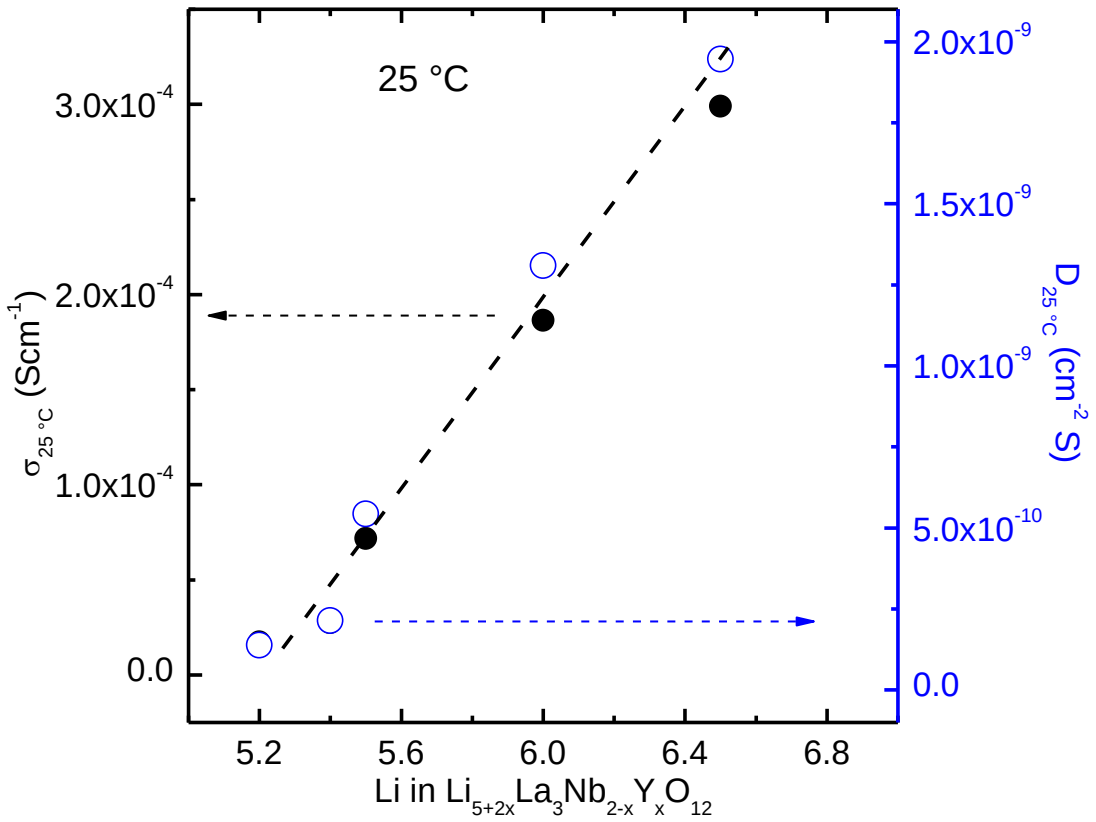

Figure 5. 20 The change in electrical conductivity and diffusivity of $Li_{5+2x}La_3Nb_{2-x}Y_xO_{12}$ (x = 0.1 to 0.75) with change in Li concentration in the formula unit at 25 °C. The line passing through the data points is a guide to the eye.

An increase in conductivity was observed with the increase in concentration of the Li ion in $Li_{5+2x}La_3Nb_{2-x}Y_xO_{12}$. The availability of more mobile ions contributes towards the total conductivity. The end members of $Li_{5+2x}La_3Nb_{2-x}Y_xO_{12}$, especially $Li_{6.5}La_3Nb_{1.25}Y_{0.75}O_{12}$, show conductivities as high as those of the outstanding garnet-like compounds given in conductivity comparison plots (Figure 5.21) [2,3,8,20,25,33].

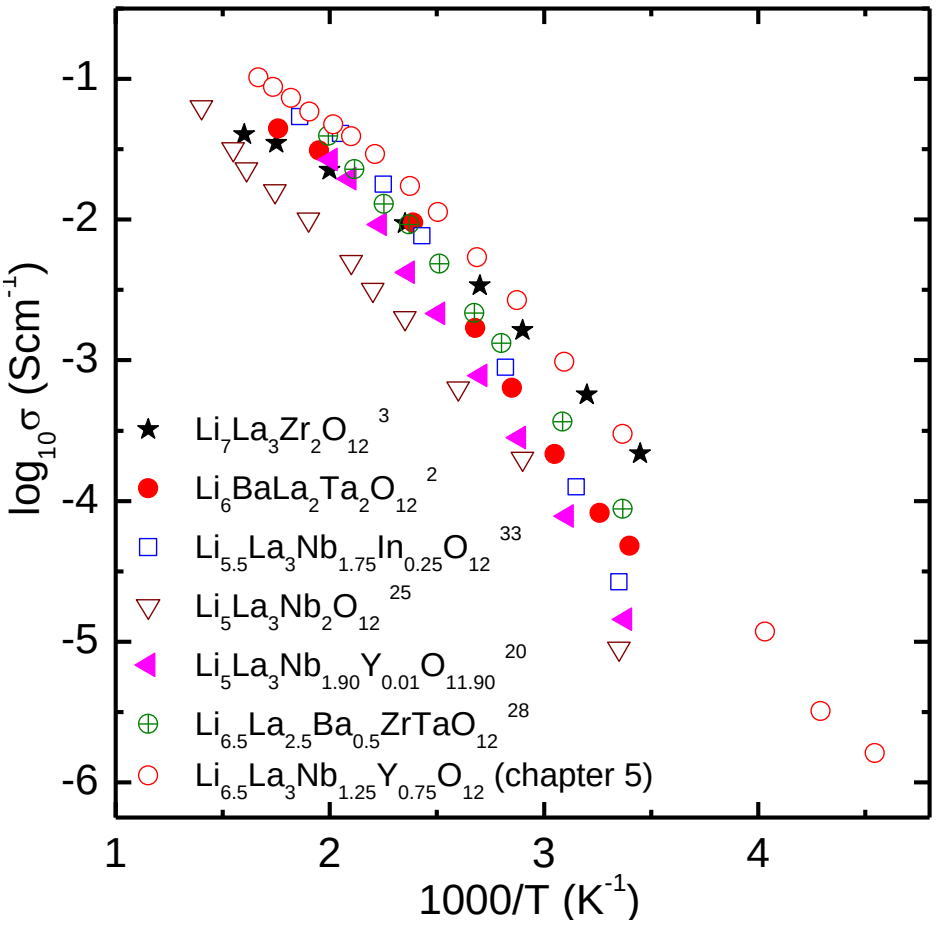

Figure 5. 21 Comparison of electrical conductivity of $Li_{6.5}La_3Nb_{1.25}Y_{0.75}O_{12}$ with that of other garnets in the literature[2,3,8,20,25,33].

5.2.5 Chemical stability of $Li_{5+2x}La_3Nb_{2-x}Y_xO_{12}$ with temperature, water, $Li_2MMn_3O_8$ (M = Co, Fe), and carbon using in-situ PXRD

The stability of garnet-like oxides with respect to temperature was studied and is illustrated in Figures 5.22 and 5.23 which show that the cubic phase is stable even after the heat treatment up to 800 °C. Rather interestingly, irrespective of significant weight loss observed in thermal analysis (Figure 5.13), the garnet-type structure was retained at

30-800 °C for x = 0.05, and 0.5 members, as confirmed by *in-situ* PXRD (Figures 5.22 and 5.23).

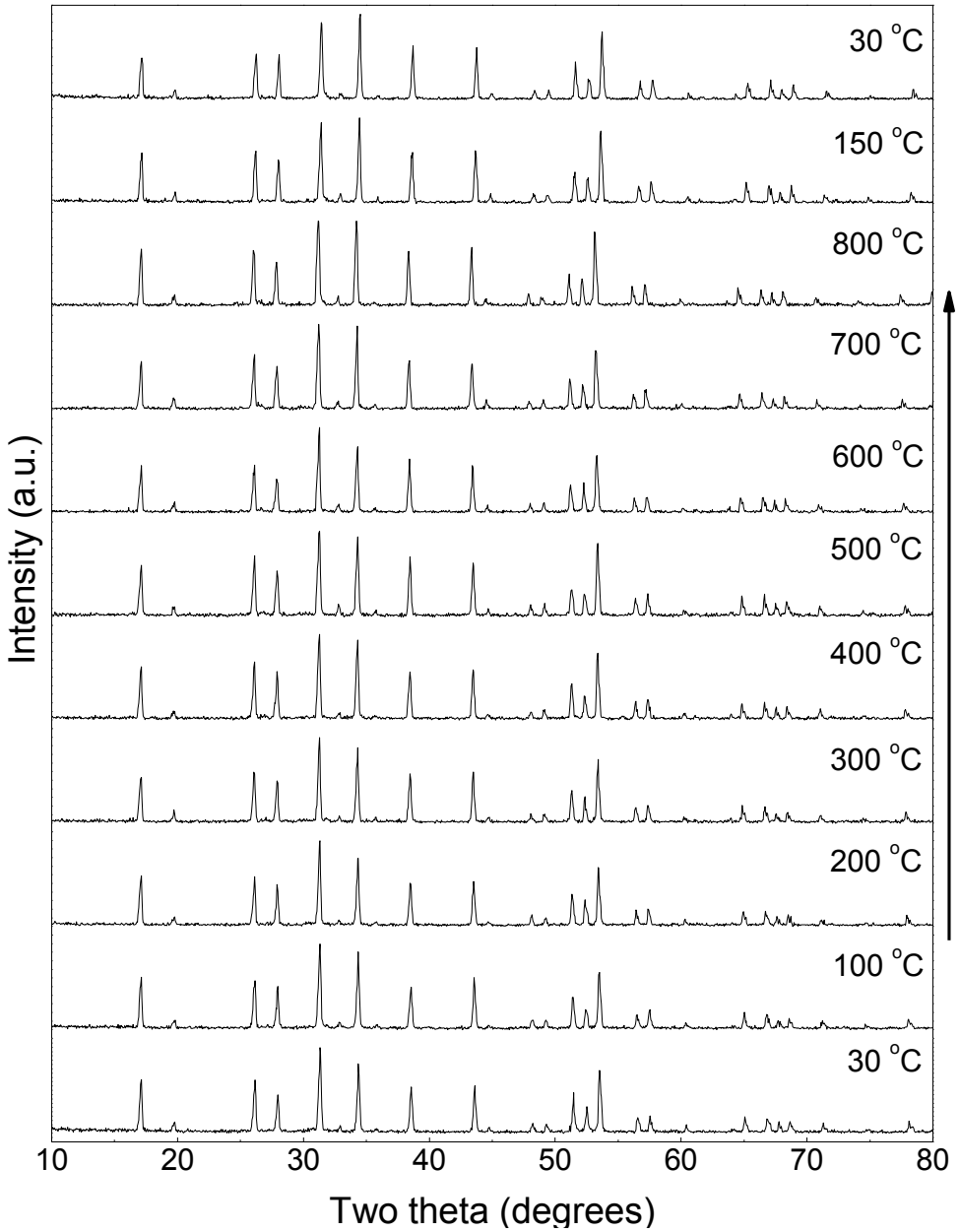

Figure 5. 22 *In-situ* PXRD of as-prepared aged $Li_{5.1}La_3Nb_{1.95}Y_{0.05}O_{12}$ in air. The arrow indicates the sequence of measurement. The samples were equilibrated for 30 mins prior to each measurement.

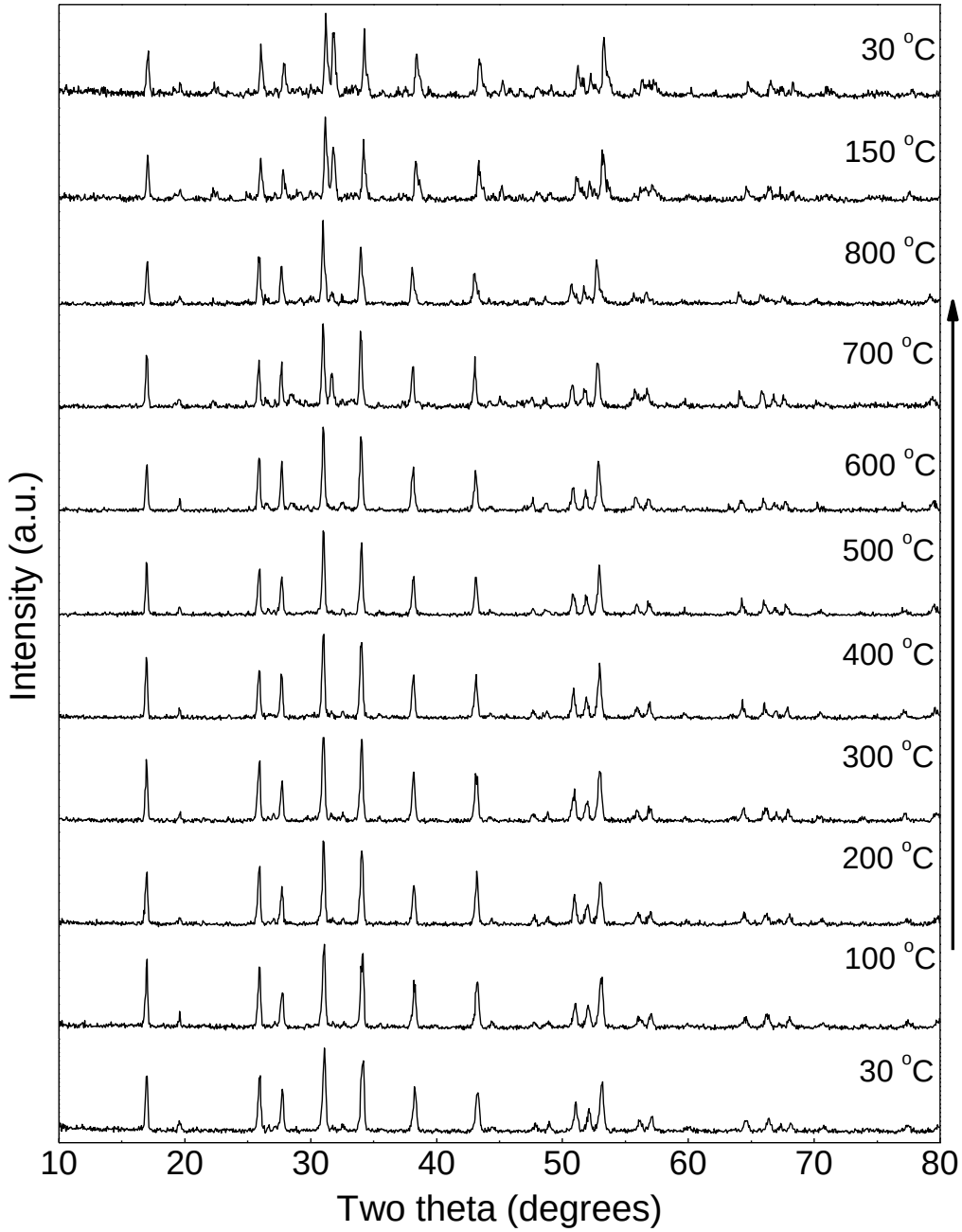

Figure 5. 23 *In-situ* PXRD of as-prepared aged $Li_6La_3Nb_{1.5}Y_{0.5}O_{12}$ in air. The arrow indicates the sequence of measurement. The samples were equilibrated for 30 mins prior to each measurement.

The possibility of exposure to air can cause water absorption. Hence, $Li_{6.5}La_3Nb_{1.25}Y_{0.75}O_{12}$ was treated with water and an *in-situ* PXRD was recorded at varying temperatures to understand the stability of water-treated samples and the results are shown in Figure 5.24. The garnet-like electrolyte material shows the same cubic structure even after the water-treatment. A few impurity peaks due to $LiLaNb_2O_7$ (ICSD No. 00-027-1249 and 01-081-1193) and $LiLa_2NbO_6$ (ICSD No. 00-040-0895) appeared at 700 °C and are marked in the figure using specific symbols. It is important to note that Li garnets are stable up to 600 °C and the present result is akin with our earlier claim, a complete decomposition of the garnet phase was noticed after 600 °C[34].

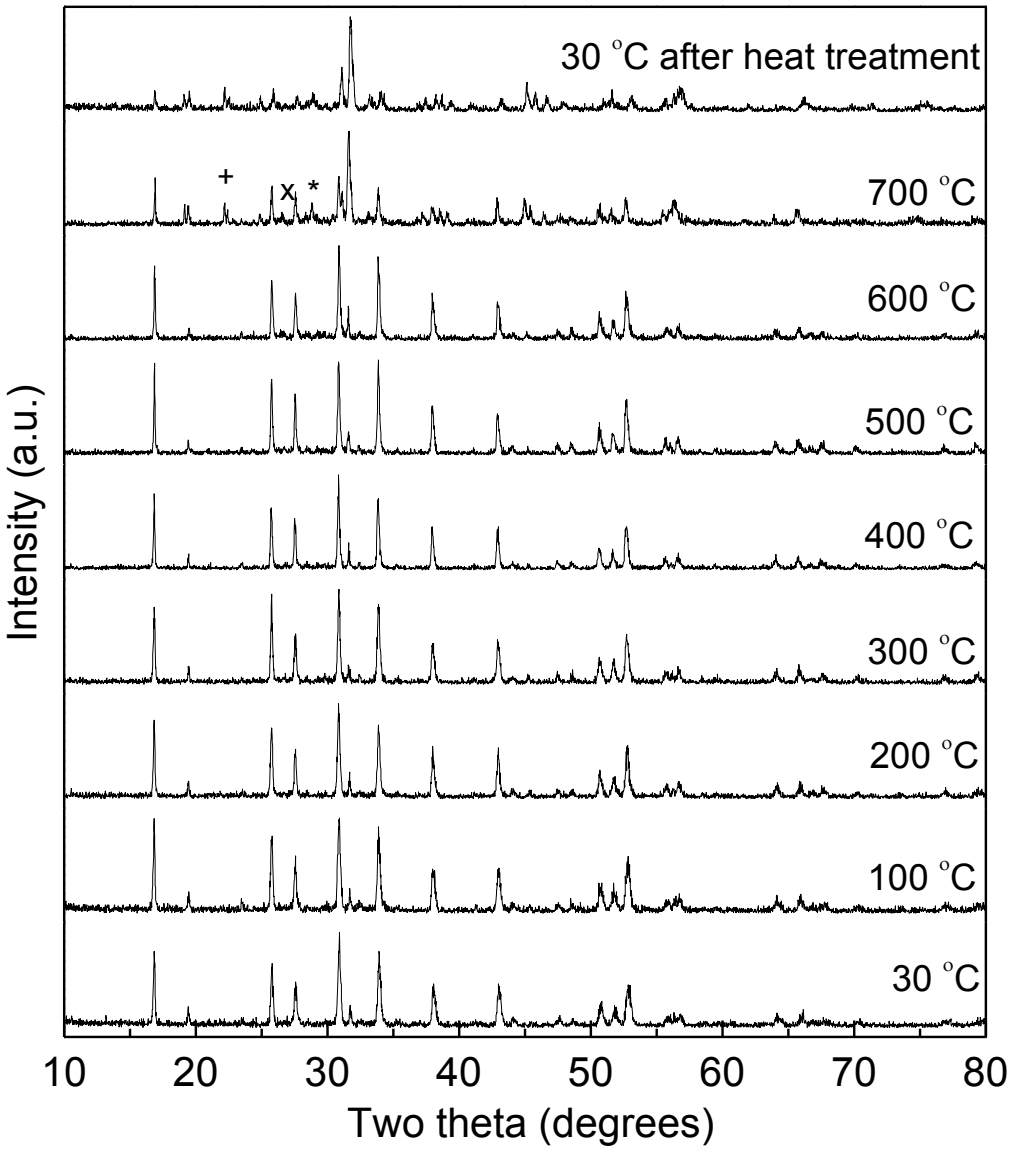

Figure 5. 24 *In-situ* PXRD showing the stability of water treated $Li_{6.5}La_3Nb_{1.25}Y_{0.75}O_{12}$ at different temperatures. The decomposed products at above 600 °C could be identified as $LiLaNb_2O_7$ (ICSD No. 00-027-1249 (*) and 01-081-1193 (x)) and $LiLa_2NbO_6$ (ICSD No. 00-040-0895 (+)).

The chemical stability and compatibility of one of the highest conducting phases, $Li_6La_3Nb_{1.5}Y_{0.5}O_{12}$, towards different Li battery components were tested. Figures 5.25 and 5.26 show the chemical stability of $Li_6La_3Nb_{1.5}Y_{0.5}O_{12}$ in the presence of high

voltage cathode materials $Li_2CoMn_3O_8$ and $Li_2FeMn_3O_8$ respectively, analyzed using *in-situ* PXRD. In both cases, a high stability up to 400 °C was observed for the garnet and after that the spinel peaks are found to be the major peaks. Perovskite peaks due to $LiLaNb_2O_7$ (ICSD No. 00-027-1249 and 01-081-1193) appeared above 400 °C and are marked in the figures.

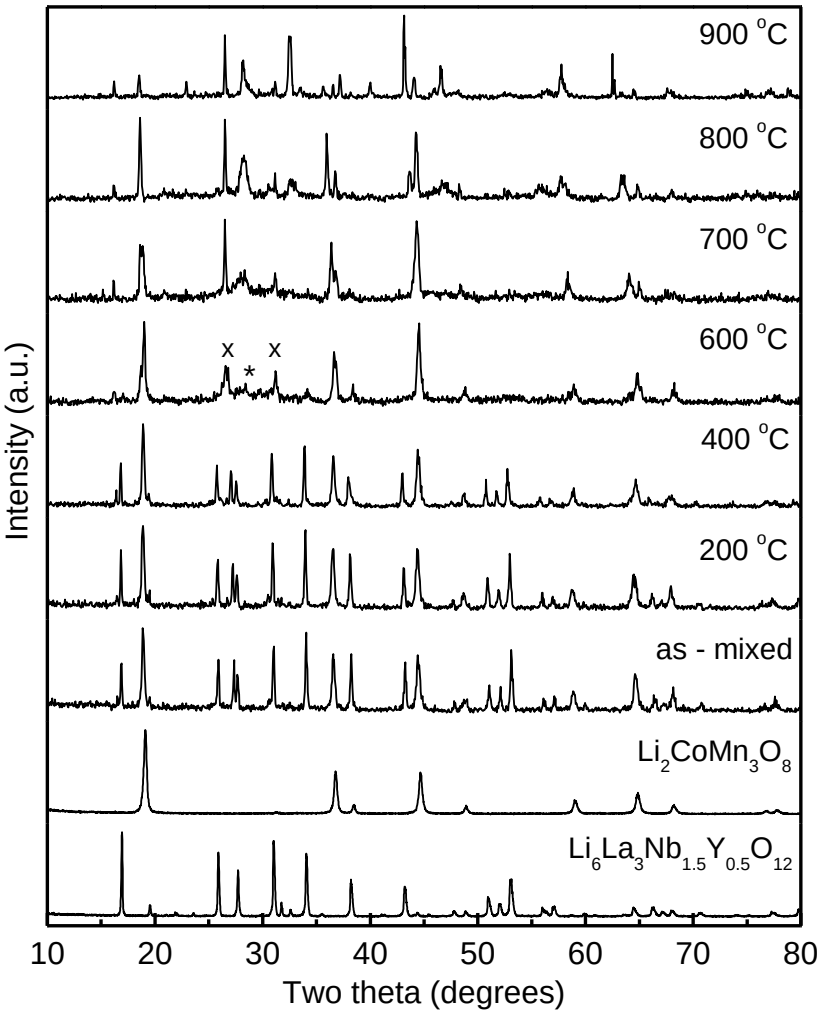

Figure 5. 25 The *in-situ* PXRD showing the stability of $Li_6La_3Nb_{1.5}Y_{0.5}O_{12}$ in the presence of high voltage cathode, $Li_2CoMn_3O_8$ at different temperatures. The electrolyte showed a high stability up to 400 °C and decayed after further increase in temperature. The impurities are identified as $LiLaNb_2O_7$ (ICSD No. 00-027-1249 (*), and 01-081-1193 (x)).

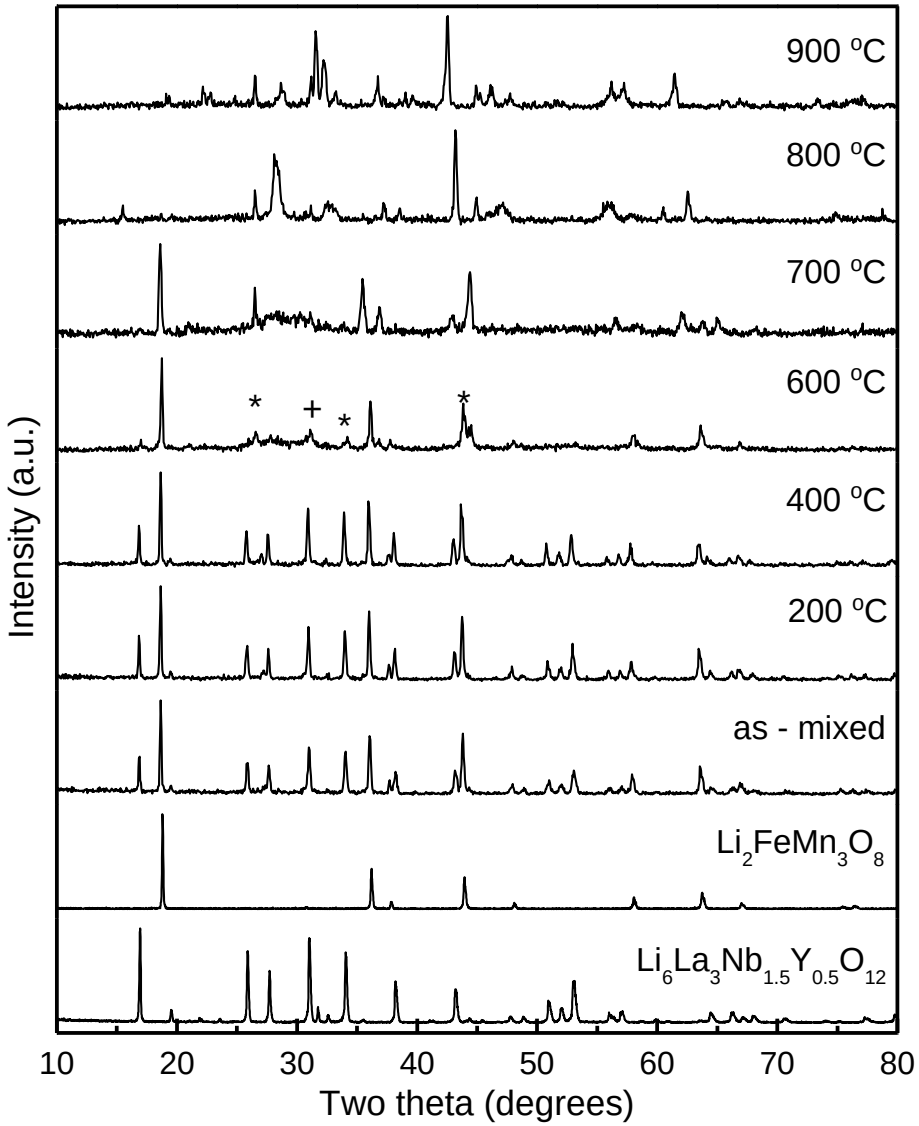

Figure 5. 26 The *in-situ* PXRD showing the stability of $Li_6La_3Nb_{1.5}Y_{0.5}O_{12}$ in the presence of high voltage cathode, $Li_2FeMn_3O_8$ at different temperatures. The electrolyte showed a high stability up to 400 °C and decayed after further increase in temperature. The impurities are identified as $LiLaNb_2O_7$ (ICSD No. 00-027-1249 (*), and $LiLa_2NbO_6$ (ICSD No. 00-040-0895 (+)).

The *in-situ* PXRD results indicating the stability of the garnet electrolyte towards the anode material (carbon) is shown in Figure 5.27. The electrolyte was inert to carbon up to 400 °C and started reacting above this temperature. Impurity peaks due to the

formation of carbonate, $Li_{0.52}La_2O_{2.52}(CO_3)_{0.74}$ (ICSD No. 01-084-1965) are marked in the pattern. The higher stabilities under the above mentioned conditions make these compounds of considerable interest for future studies on solid state electrolytes.

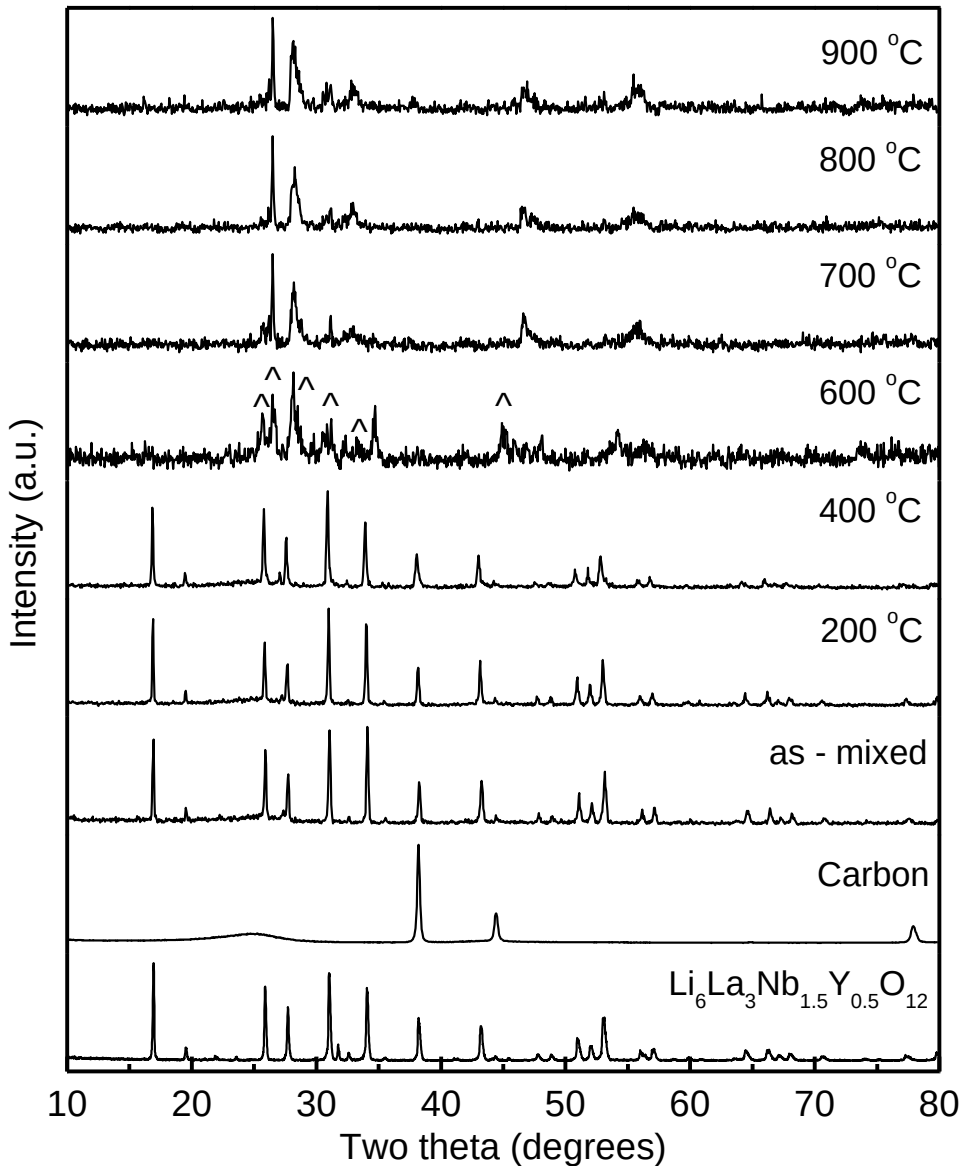

Figure 5. 27 The *in-situ* PXRD pattern showing the stability of $Li_6La_3Nb_{1.5}Y_{0.5}O_{12}$ in the presence of carbon anode at different temperatures. The garnet electrolyte showed a high stability up to 400 °C. Impurity peaks due to the formation of carbonate, $Li_{0.52}La_2O_{2.52}(CO_3)_{0.74}$ (ICSD No. 01-084-1965) are shown by (^).

5.2.6 Electron probe microanalysis (EPMA) of $Li_{5+2x}La_3Nb_{2-x}Y_xO_{12}$

Figures 5.28 and 5.29 show the maps for $Li_{5.1}La_3Nb_{1.95}Y_{0.05}O_{12}$, and $Li_6La_3Nb_{1.5}Y_{0.5}O_{12}$. The possible impurity of Al in both the cases from the synthesis process is again confirmed in this analysis.

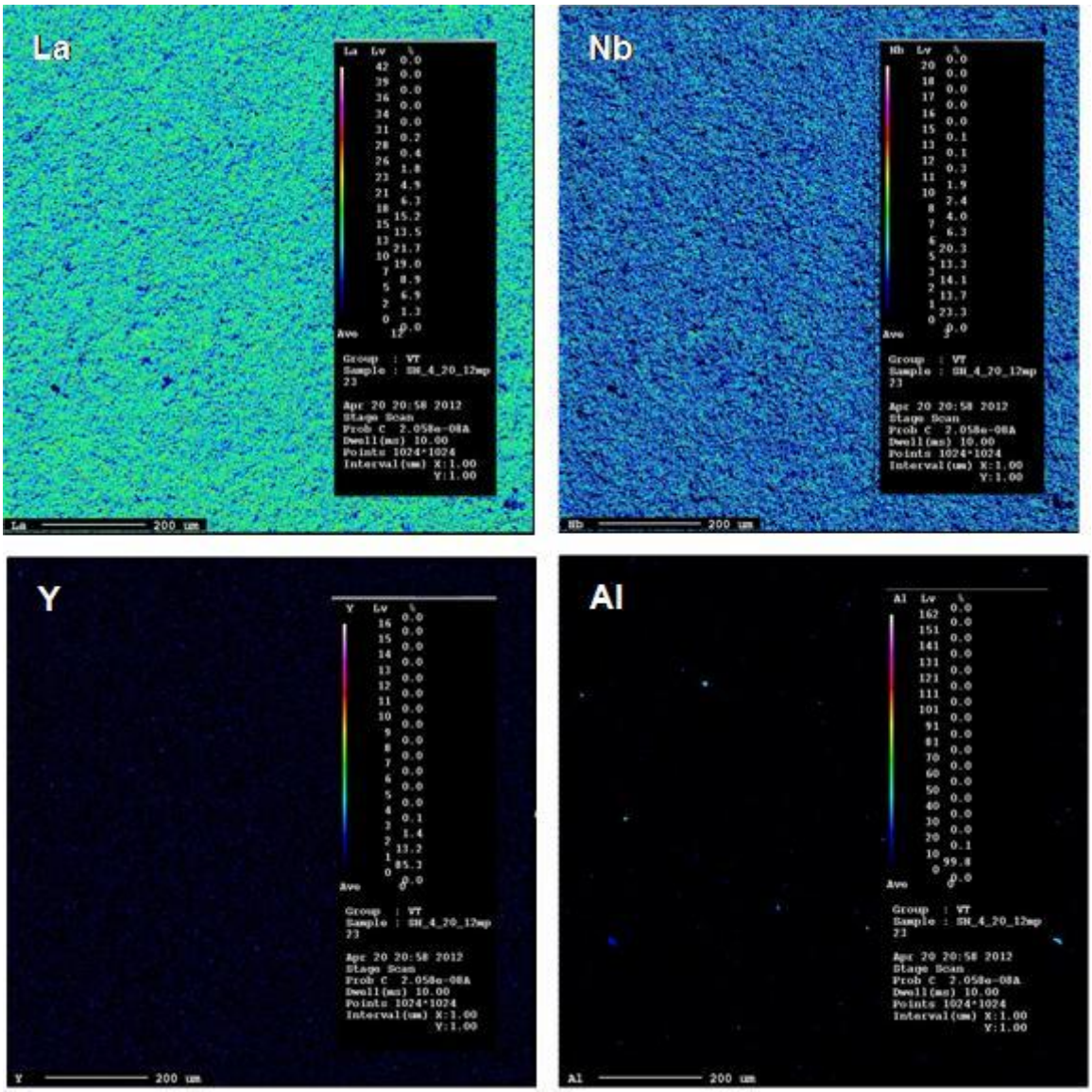

Figure 5. 28 EPMA maps of $Li_{5.1}La_3Nb_{1.95}Y_{0.05}O_{12}$. Maps due to heavy atoms La, Y, Nb, and Al are given. The presence of impurity Al is clearly visible.

Figure 5.30 shows the compatibility of $Li_6La_3Nb_{1.5}Y_{0.5}O_{12}$ and $Li_2FeMn_3O_8$ tested using EPMA studies of the pellet made from 1:1 ratio mixture after heating at 400 °C. No aggregation of impurity phase throughout the sample was observed.

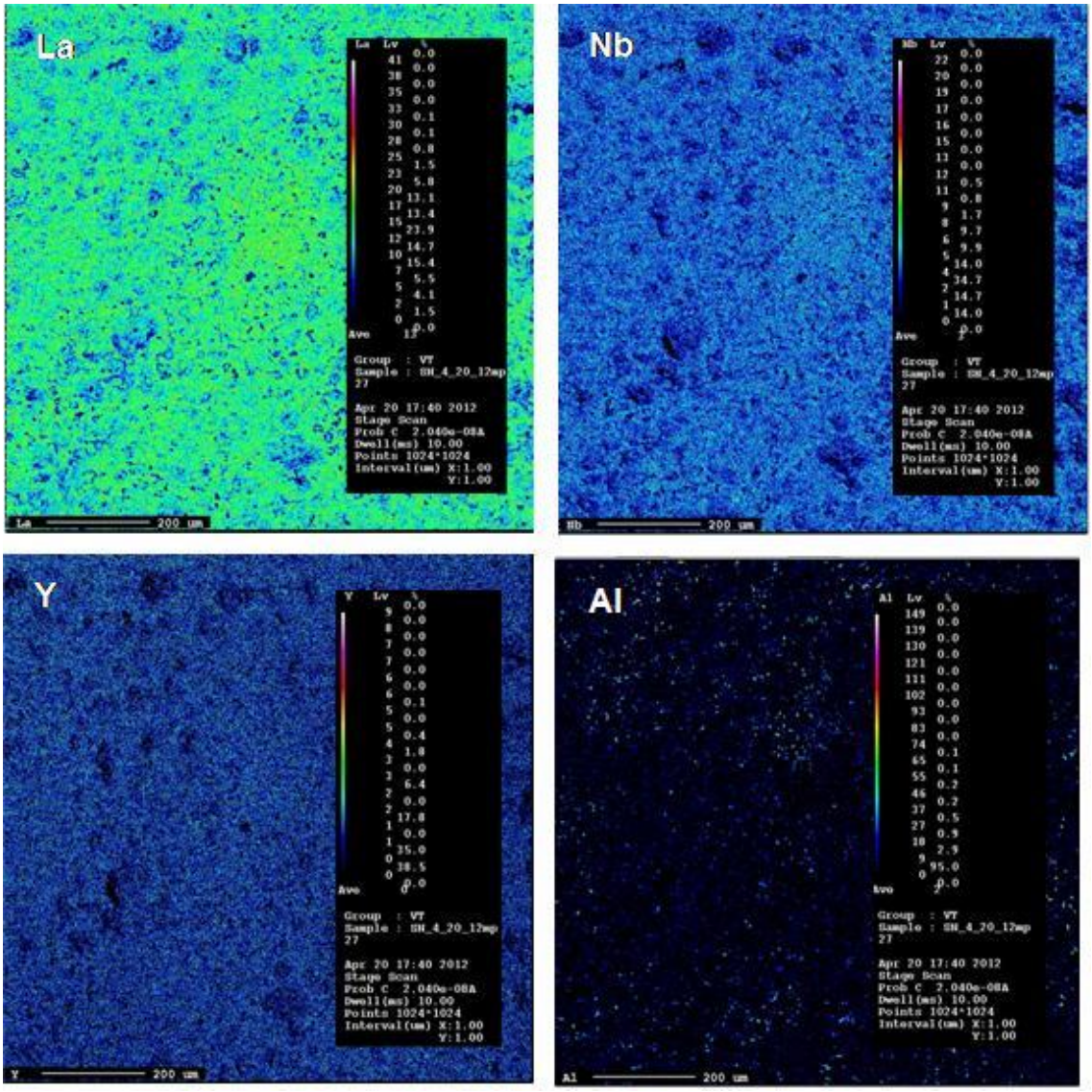

Figure 5. 29 EPMA maps of $Li_6La_3Nb_{1.5}Y_{0.5}O_{12}$. Maps due to heavy atoms La, Y, Nb, and Al are given. The presence of impurity Al is clearly visible.

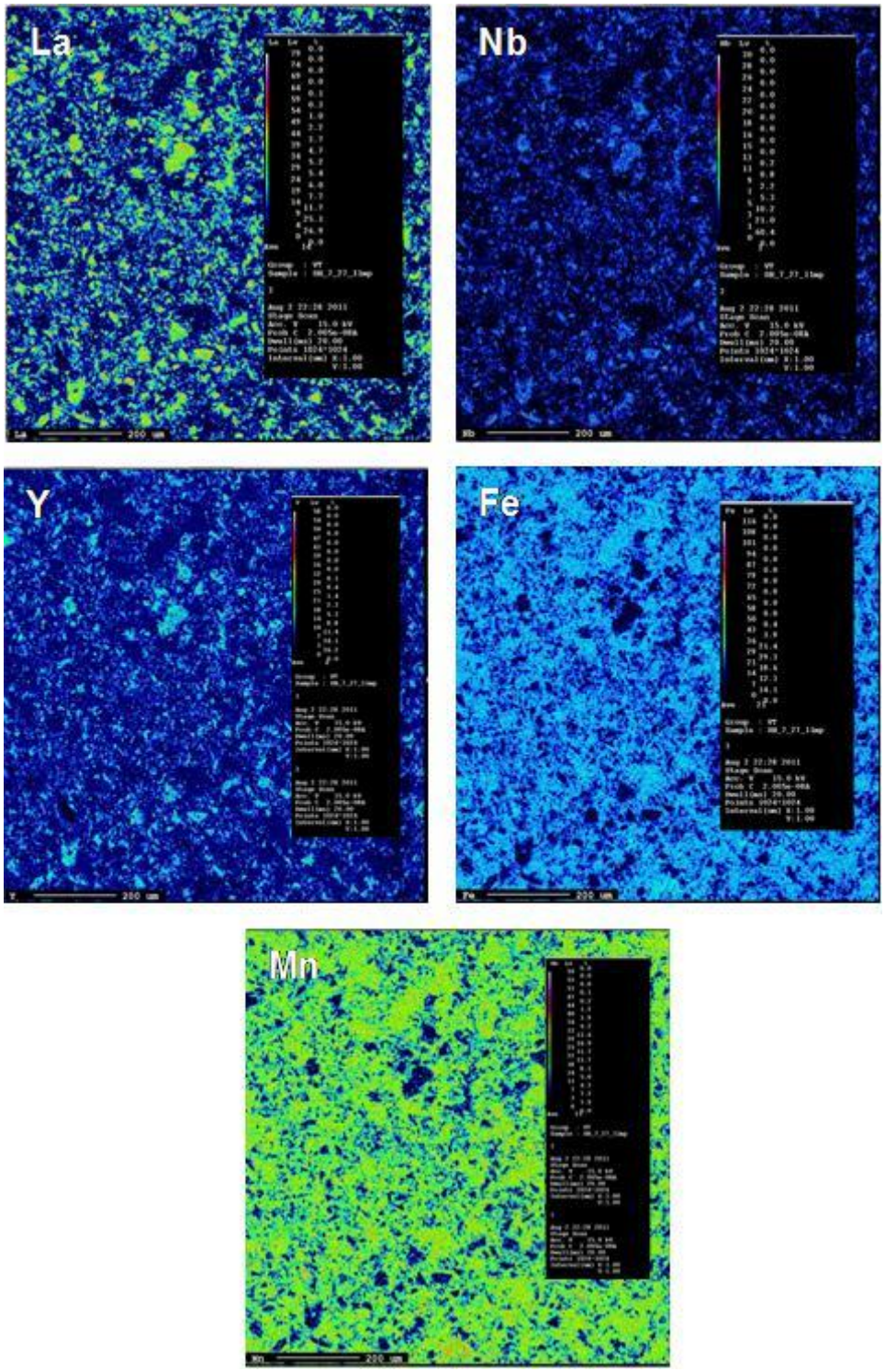

Figure 5. 30 EPMA maps of sample containing $Li_6La_3Nb_{1.5}Y_{0.5}O_{12}$ and $Li_2FeMn_3O_8$ in 1:1 wt ratio after heating at 400 °C.

5.3 Summary

The garnet-like $Li_{5+2x}La_3Nb_{2-x}Y_xO_{12}$ is found to be a promising candidate as electrolyte for future all-solid-state energy storage systems. The PXRD refinements show a cubic crystal structure with space group *Ia*-3*d*. The electrical conductivity measurements show very high σ for the higher lithium stuffed members. $Li_{6.5}La_3Nb_{1.25}Y_{0.75}O_{12}$ showed a conductivity of 10^{-4} Scm^{-1} at 24 °C which is same order of magnitude as that of the highest ranking garnet-like compound known so far, $Li_7La_3Zr_2O_{12}$. The diffusivity was found to be increasing with increase in the Li content in the formula unit. $Li_{5+2x}La_3Nb_{2-x}Y_xO_{12}$ showed a higher structural stability in water compared to parent compound**.** Also, the chemical stability of $Li_{5+2x}La_3Nb_{2-x}Y_xO_{12}$ towards high voltage cathode spinels ($Li_2MMn_3O_8$, M = Co, Fe) is very promising and a high stability up to 400 °C was observed. The advantages such as very good Li^+ conductivity and high chemical stability make $Li_{5+2x}La_3Nb_{2-x}Y_xO_{12}$ a strong candidate for future battery research.

Chapter Six: **Macroscopic and microscopic studies on the Li^+ transport properties of cubic garnet-like $Li_{6.5}La_{2.5}Ba_{0.5}ZrTaO_{12}$ by AC impedance and NMR spectroscopy**

6.1 General overview

A detailed study of the transport properties of a garnet-like electrolyte material with a nominal formula, $Li_{6.5}La_{2.5}Ba_{0.5}ZrTaO_{12}$ is described in this chapter. Several techniques such as variable-temperature ^7Li NMR spectroscopy, low-temperature AC-impedance measurements, electron microprobe analyses, and powder X-ray diffraction (PXRD) techniques are used to characterize the structural and dynamic properties. The conventional solid state method using metal oxides and salt precursors of high purity was used for the material synthesis.

The phase analysis of the garnet-type structure was studied by powder X-ray diffraction (PXRD). Electron probe microanalysis coupled with a wavelength-dispersive spectrometer showed a rather homogeneous distribution of the heavy cations, such as Ta and Zr, compared to Ba and La in $Li_{6.5}La_{2.5}Ba_{0.5}ZrTaO_{12}$. Li ion dynamics were complementarily studied using variable-temperature AC-impedance spectroscopy and ^7Li NMR measurements. The bulk (ion) conductivities probed are in very good agreement with results reported earlier illustrating the excellent reproducibility of Li transport properties of $Li_{6.5}La_{2.5}Ba_{0.5}ZrTaO_{12}$. The conductivity at lower temperature is also very promising. In particular, AC impedance and NMR results indicate that the Li transport process studied is long-range in nature. Finally, the chemical compatibility of the electrolyte $Li_{6.5}La_{2.5}Ba_{0.5}ZrTaO_{12}$ was tested with $Li_2FeMn_3O_8$, a high-voltage cathode

material. As shown by variable-temperature PXRD measurements, the garnet-type structure (bulk) was found to be stable up to 673 K.

6.2 Results and discussion[3]

6.2.1 Phase analysis

The PXRD pattern in Figure 6.1 clearly shows that $Li_{6.5}La_{2.5}Ba_{0.5}ZrTaO_{12}$ is crystallized in cubic form[1]. Table 6.1 lists the corresponding indexed PXRD data calculated from *PROSZKI* program. Most peaks could be indexed according to the cubic garnet-like parent, $Li_5La_3Nb_2O_{12}$, which crystallizes in the space group I*a*-3*d*[2-10]. For comparison, the calculated pattern is also provided[10]. The cell constant, *a*, obtained is 12.764(3) Å, which is comparable to the values reported in the literature[6-8].

[3] Narayanan, S.; Epp, V.; Wilkening, M.; Thangadurai, V. *RSC Adv.* **2012**, *2*, 2553-2561

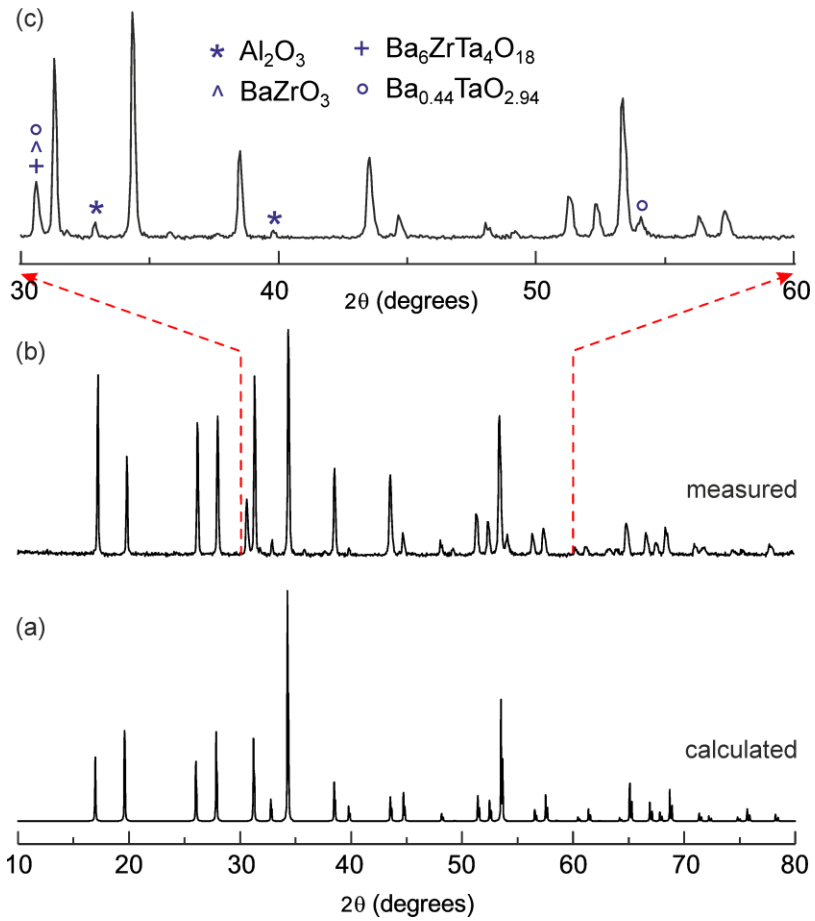

Figure 6. 1 Powder X-ray diffraction pattern of (a) the calculated PXRD pattern of cubic $Li_5La_3Nb_2O_{12}$ (*a* = 12.80654(11) Å; space group *Ia*-3*d*[10], (b) $Li_{6.5}La_{2.5}Ba_{0.5}ZrTaO_{12}$ prepared by conventional solid-state synthesis, and (c) selected range of the measured PXRD pattern showing the potential impurity phases present[1].

However, a few impurity peaks of very low intensities were also observed, which could be attributed to Al_2O_3, $Ba_6ZrTa_4O_{18}$, $BaZrO_3$, and $Ba_{0.5}TaO_3$. They are marked in the selected area PXRD spectra (Figure 6.1 (c))[1]. The major diffraction peaks of these impurity phases are summarized in Table 6.2[1].

Table 6. 1 Indexed parameters obtained from the analyses of the PXRD pattern for $Li_{6.5}La_{2.5}Ba_{0.5}ZrTaO_{12}$[1].

H	*k*	*l*	$d_{obs.}$ (Å)	$d_{cal.}$ (Å)	$I_{obs.}$ (%)
2	1	1	5.151	5.211	93
2	2	0	4.480	4.513	52
3	2	1	3.405	3.411	69
4	0	0	3.184	3.191	72
4	2	0	2.856	2.854	93
3	3	2	2.720	2.721	10
4	2	2	2.609	2.605	100
5	2	1	2.336	2.330	46
6	1	1	2.077	2.071	43
6	2	0	2.028	2.018	14
6	3	1	1.892	1.882	10
4	4	4	1.850	1.842	6
5	5	1	1.781	1.787	23
7	2	0	1.748	1.753	19
6	4	2	1.716	1.706	73
6	5	0	1.633	1.634	13
8	0	0	1.607	1.596	16
8	2	1	1.537	1.537	6
6	6	0	1.516	1.504	7
6	6	2	1.468	1.464	6
8	3	2	1.452	1.455	6
7	5	2	1.439	1.445	18
9	1	1	1.404	1.401	14
7	6	0	1.388	1.384	9
7	6	1	1.372	1.376	17
8	5	2	1.328	1.324	8

9	3	2	1.313	1.317	6
10	1	0	1.274	1.270	5
10	1	1	1.264	1.264	5
10	2	2	1.229	1.228	8

a =12.764(3) Å

Table 6. 2 Possible impurity phases that can be observed in the powder XRD pattern of $Li_{6.5}La_{2.5}Ba_{0.5}ZrTaO_{12}$ (Figure 6.1)[1].

Compound	Symmetry	Space group	JCPDS[a] Card No.	2θ (degrees)	Intensity (%)	Symbol
θ-Al_2O_3	Monoclinic	*C2/m*	01-086-1410;	32.8	100	*
		C2/m	00-023-1009;	39.8	62	*
		A2/m	00-009-0440			
$Ba_6ZrTa_4O_{18}$	Rhombo-hedral	*R*-3*m*	00-044-0563	30.6	100	+
$BaZrO_3$	Cubic	*Pm*-3*m*	01-089-2486	30.5	100	^
				43.6	54	^
$Ba_{0.44}TaO_{2.94}$	Hexagonal	*P*-62*m*	00-017-0795	30.7	100	o
				54.1	67	o

[a] Joint Committee on Powder Diffraction Standards (*JCPDS*).

It is understood that for garnet-type $Li_7La_3Zr_2O_{12}$, incorporation of Al into the structure could occur during the synthesis process and ^{27}Al MAS NMR spectroscopy confirms the presence of Al in the structure[11]. Figure 6.2 shows the ^{27}Al MAS NMR spectrum of $Li_{6.5}La_{2.5}Ba_{0.5}ZrTaO_{12}$[1]. The high-resolution NMR spectrum is composed of several lines appearing at the isotropic chemical shifts (δ_{iso}) indicated. While δ_{iso} values around 15 ppm indicate octahedrally coordinated Al ions, chemical shifts larger than 70

ppm can typically be attributed to tetrahedrally coordinated Al. Besides Al present in the various separate impurity phases mentioned above, most likely Al cations also occupy multiple sites in the garnet-type structure as well. In particular, the NMR peaks at 78 and 81 ppm might reflect Al ions in tetrahedral sites. Additional deshielding (signal located at 93 ppm) may result from cation vacancies in the direct vicinity of the Al ions. It may also be an indication of Al ions residing in dodecahedral cages present in the garnet-type structure.

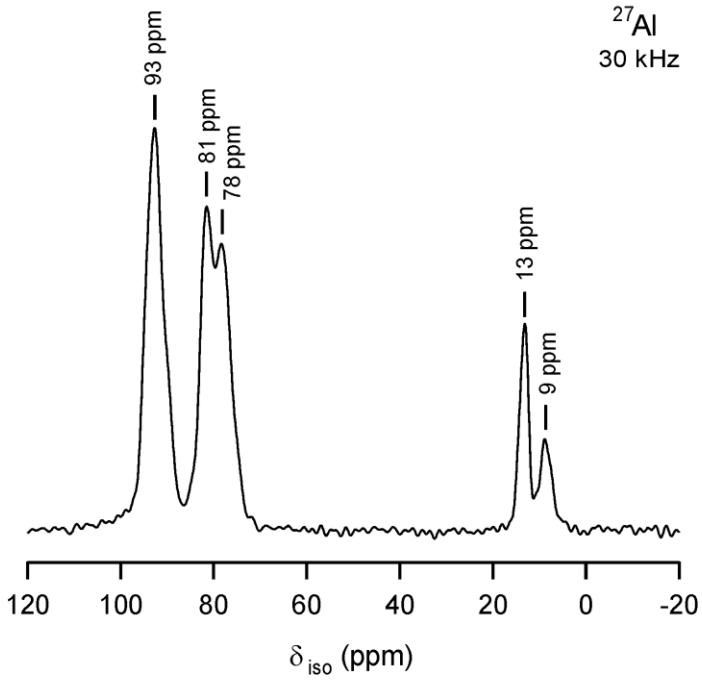

Figure 6. 2 ^{27}Al MAS NMR spectrum (306 K) of $Li_{6.5}La_{2.5}Ba_{0.5}ZrTaO_{12}$ prepared using an Al_2O_3 crucible at 1373 K. The spectrum was recorded at 14.1 T using a MAS rotation frequency of 30 kHz[1].

For comparison with known Al-containing oxides (and hydroxides), the NMR line of α-Al_2O_3 typically produces a single peak with a chemical shift value in the range

from 13 to 17 ppm, while the NMR lines of θ-Al_2O_3, which has an equal number of octahedral and tetrahedral sites, are reported to be centered at 11(1) and 80(1) ppm[12]. Note that the NMR peak of γ-AlOOH (Boehmite), which transforms into γ-Al_2O_3 (signals at 12 and 70 ppm) and α-Al_2O_3 at sufficiently high temperatures, usually appears between 5 and 9 ppm[12]. Interestingly, NMR intensities located in the 75 to 85 ppm range are also visible in the ^{27}Al NMR spectrum of Al-doped $Li_7La_3Zr_2O_{12}$, discussed in detail by Geiger et al.[11]. Elemental mapping of a large area (on the order of several hundred square micrometers) of garnet-type $Li_{6.5}La_{2.5}Ba_{0.5}ZrTaO_{12}$ prepared at 1373 K is shown in Figure 6.3[1]. Regardless of the slight Al contamination of the garnet phase (Figures 6.1 and 6.2), the electron probe microanalysis (EPMA) coupled with a wavelength-dispersive spectrometer (WDS) showed a rather homogeneous distribution of Ta and Zr ions, compared to the Ba and La ions in $Li_{6.5}La_{2.5}Ba_{0.5}ZrTaO_{12}$.

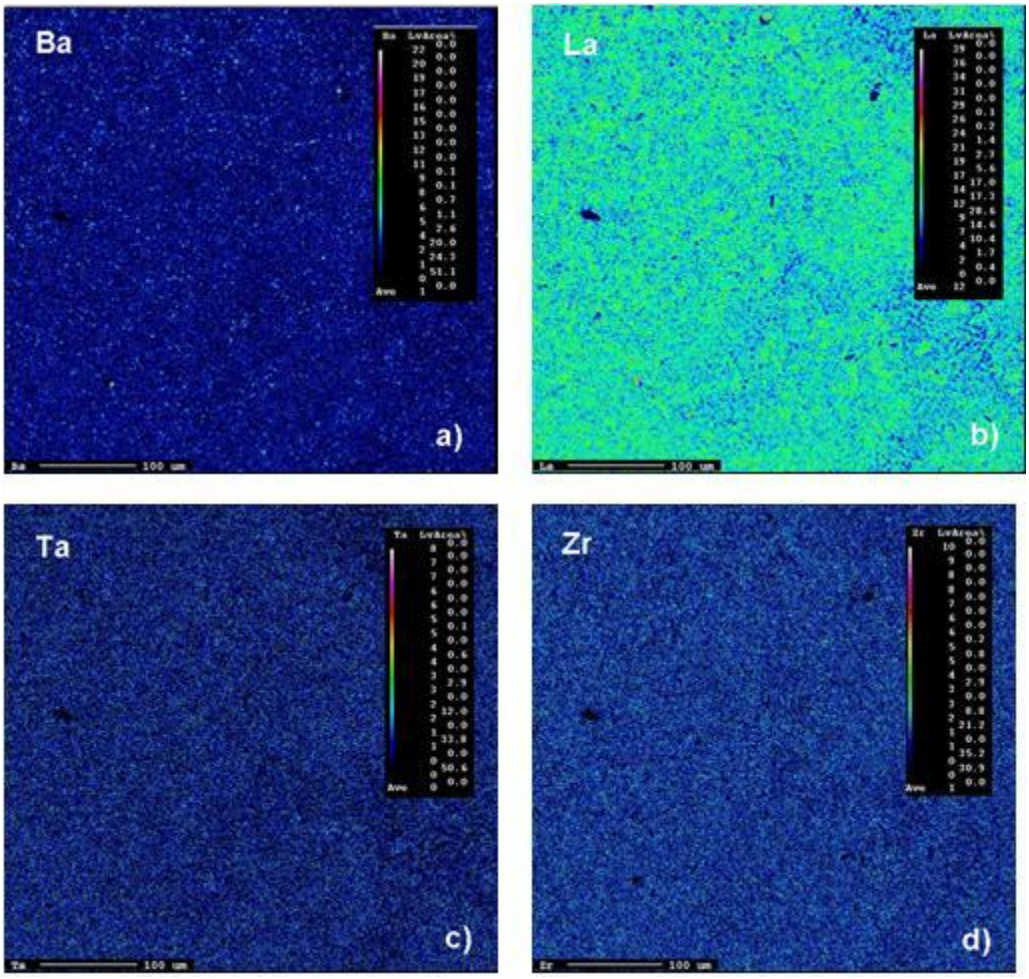

Figure 6. 3 Typical elemental mapping analysis of polycrystalline $Li_{6.5}La_{2.5}Ba_{0.5}ZrTaO_{12}$ prepared by conventional solid-state synthesis: (a) Ba, (b) La, (c) Ta and (d) Zr mapping[1].

6.2.2 Electrical properties using impedance spectroscopy

The typical AC-impedance plots (Nyquist plots) of $Li_{6.5}La_{2.5}Ba_{0.5}ZrTaO_{12}$ recorded at 230 K, 252 K and 257 K in air are shown in Figures 6.4-6.6[1]. It shows that both the bulk and grain-boundary contributions can be well resolved and appear as separate semi circles. The spike at the lower frequency side indicates electrode polarization effects. The frequency dependent data were quantitatively analyzed using a

suitable equivalent circuit with individual resistors and constant phase elements (CPEs) representing the electrical bulk, grain-boundary, and electrode responses. Figure 6.7 is the corresponding equivalent circuit used for fitting. Table 6.3 gives the resulting fitting parameters, which correspond to the solid lines in Figure 6.4-6.6[1]. Among others, these include the bulk and grain boundary resistances, R_b and R_{gb}. The complex impedance $\hat{Z}_{CPE}$ of a constant phase element can be expressed using equation [2.18][13]. CPE (or Q) has the numerical value of the admittance $1/\left|\hat{Z}\right|$ at ω = 1 rads^{-1}. Accordingly, the capacitance which can be associated with the CPE was calculated using the equation [5.1][13].

In this case, the parameter n was found to be close to one, that is $C \approx Q$. While the capacitance C for the high-frequency semicircle was on the order of 10^{-11} F, the semicircle appearing at intermediate frequencies has capacitance ranging from 10^{-9} to 10^{-10} F, as provided in Table 6.3. These values are typical for capacitances which can be ascribed to bulk and grain-boundary contributions, respectively, in ion conducting ceramic materials[14,15]. Note that the quality of the fits performed, which is expressed by the parameter χ^2, increases with increasing temperature as shown in Table 6.3[1]. As expected, the bulk resistance decreases with increasing T, clearly indicating a thermally activated electrical relaxation process.

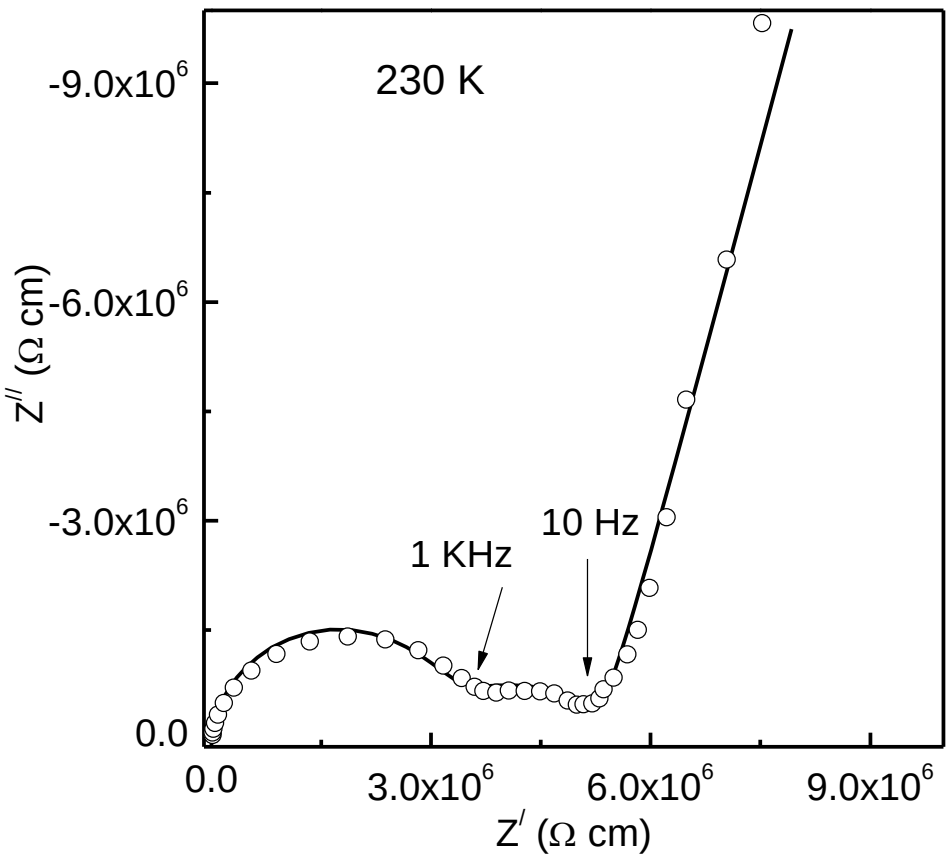

Figure 6. 4 Typical AC-impedance plot of $Li_{6.5}La_{2.5}Ba_{0.5}ZrTaO_{12}$ recorded at 230 K. Solid line and open circles represent the fitted and measured data, respectively. Bulk, grain-boundary, and electrode responses can be well separated[1].

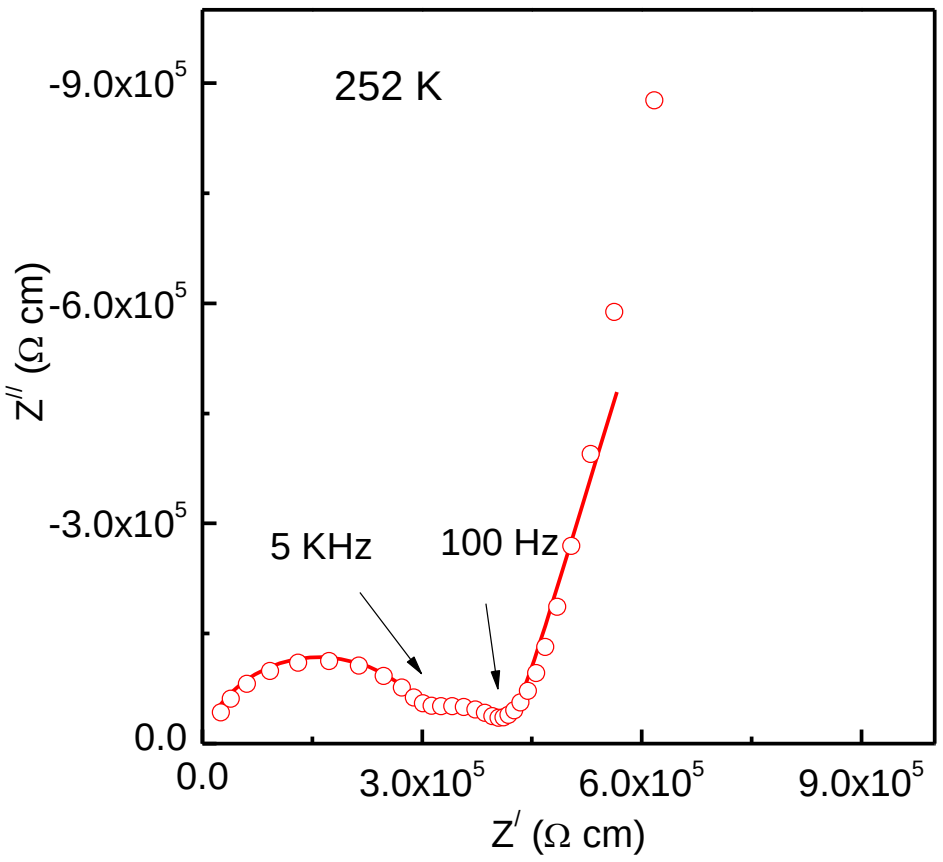

Figure 6. 5 Typical AC-impedance plot of $Li_{6.5}La_{2.5}Ba_{0.5}ZrTaO_{12}$ recorded at 252 K. Solid line and open circles represent the fitted and measured data, respectively. Bulk, grain-boundary, and electrode responses can be well separated[1].

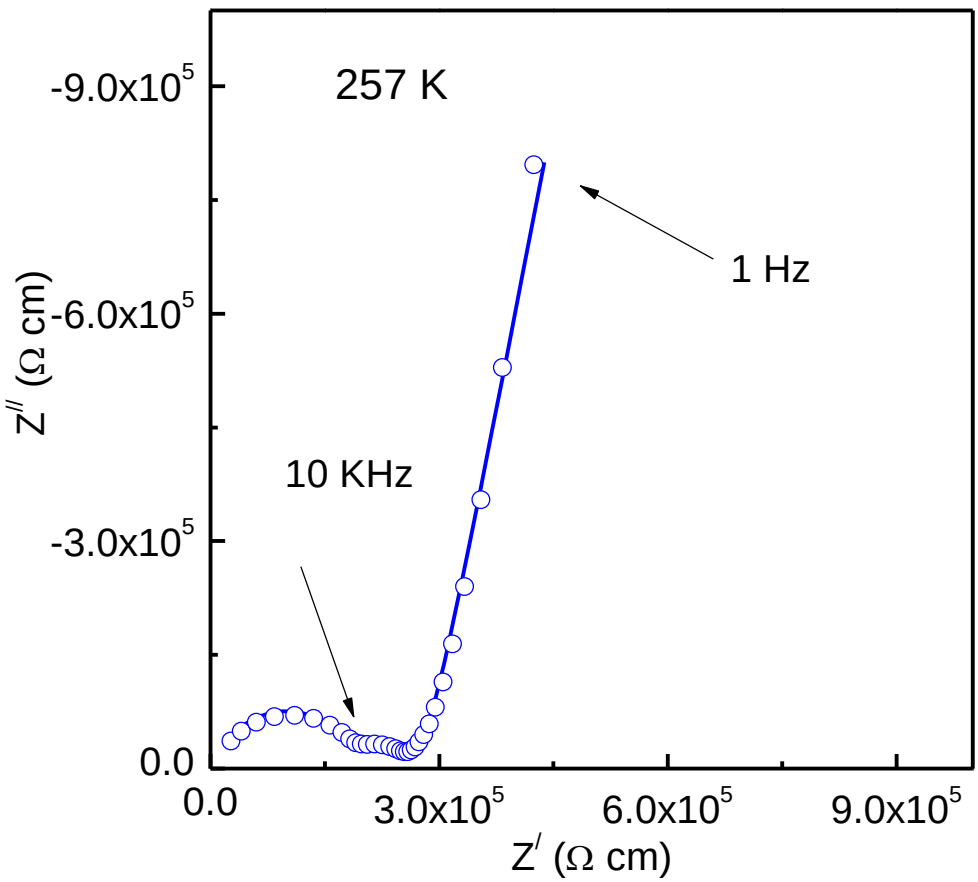

Figure 6. 6 Typical AC-impedance plot of $Li_{6.5}La_{2.5}Ba_{0.5}ZrTaO_{12}$ recorded at 257 K. Solid line and open circles represent the fitted and measured data, respectively. Bulk, grain-boundary and electrode responses can be well separated[1].

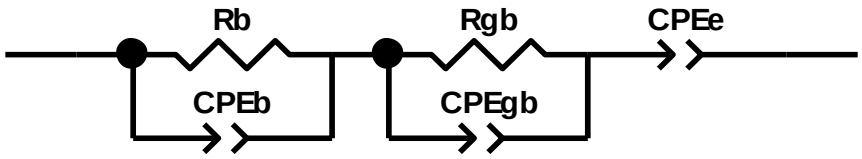

Figure 6. 7 The corresponding equivalent circuit used for fitting the impedance data provided in Figure 6.4-6.6. It includes two parallel resistor and constant phase elements and a series constant phase element[1].

Table 6. 3 Fitting results of the analysis of the AC-impedance data (Figure 6.4 to 6.6 by using suitable equivalent circuit elements (shown in Figure 6.7) [1].

T (K)	R_b (Ω)	C_b (F)	R_{gb} (Ω)	C_{gb} (F)	χ^2
230	8.95×10^5	1.50×10^{-11}	6.04×10^5	1.49×10^{-9}	3×10^{-3}
252	8.64×10^4	1.59×10^{-11}	3.18×10^4	4.55×10^{-9}	9×10^{-4}
257	3.56×10^4	2.23×10^{-11}	4.68×10^4	7.34×10^{-10}	4×10^{-4}

For comparison, typical impedance spectra, which are obtained by plotting the real part σ of the complex conductivity versus ω, are shown in Figure 6.8[1]. Depending on temperature, in the range from 10^3 to 10^6 Hz, the spectra reveal an almost frequency independent conductivity plateau. Polarization effects due to ion blocking electrodes appear when ω is smaller than approximately 10^2 Hz and temperatures ranging from 297 K to 357 K are considered (Figure 6.8). At the highest frequencies, the beginning of a dispersive AC-conductivity region can be seen, where $\sigma(\omega)$ seems to follow a power law behaviour according to equation [5.2][16-23].

In most cases, the power law exponent, p shows values between 0.6 and 0.8[16-23]. The corresponding complex plane plots are presented in Figure 6.9[1]. Arrows mark the frequency range used for the power law fits, which are shown in Figure 6.8 by solid lines. Fitting parameters are provided in Table 6.4. Since the dispersive region was only partly accessible due to experimental limitations, the power law exponents must be regarded as rough estimations. Nevertheless, the values obtained are in agreement with corresponding

results from literature, particularly with those which have been reported for structurally disordered materials[21-23].

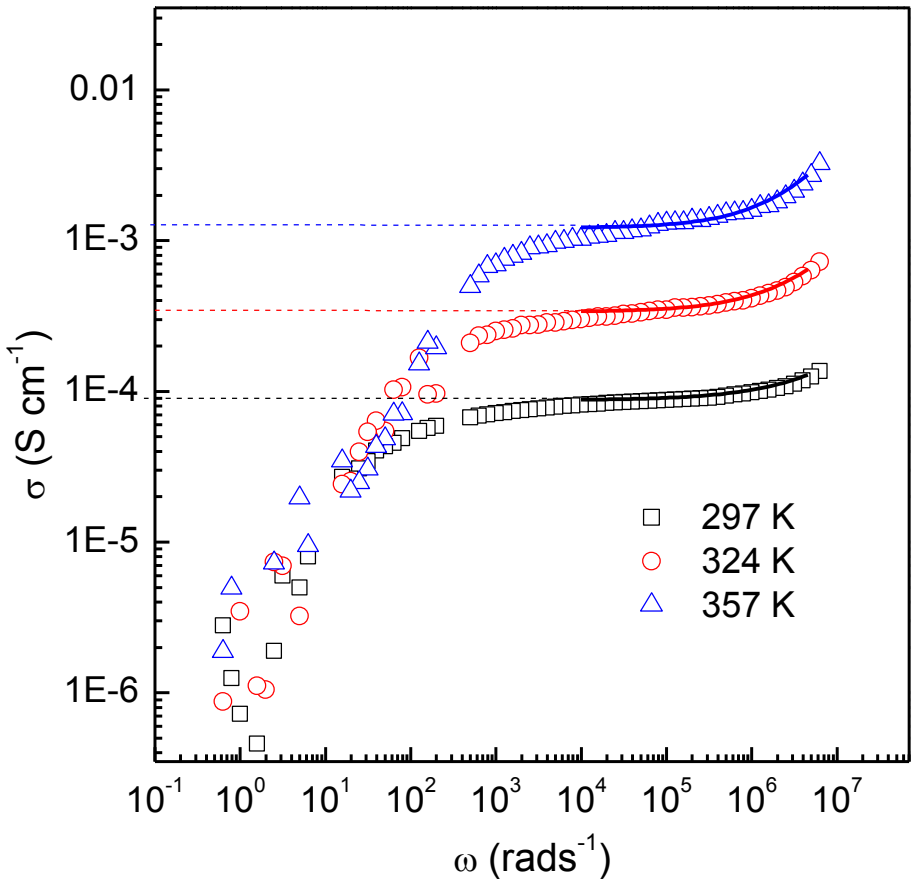

Figure 6. 8 The conductivity vs frequency plots of $Li_{6.5}La_{2.5}Ba_{0.5}ZrTaO_{12}$ measured at the temperatures indicated. Prior to the measurements, the polycrystalline sample was sintered at 1373 K in air. Solid lines represent a rough analysis of the data using power law expression, equation [5.2][1].

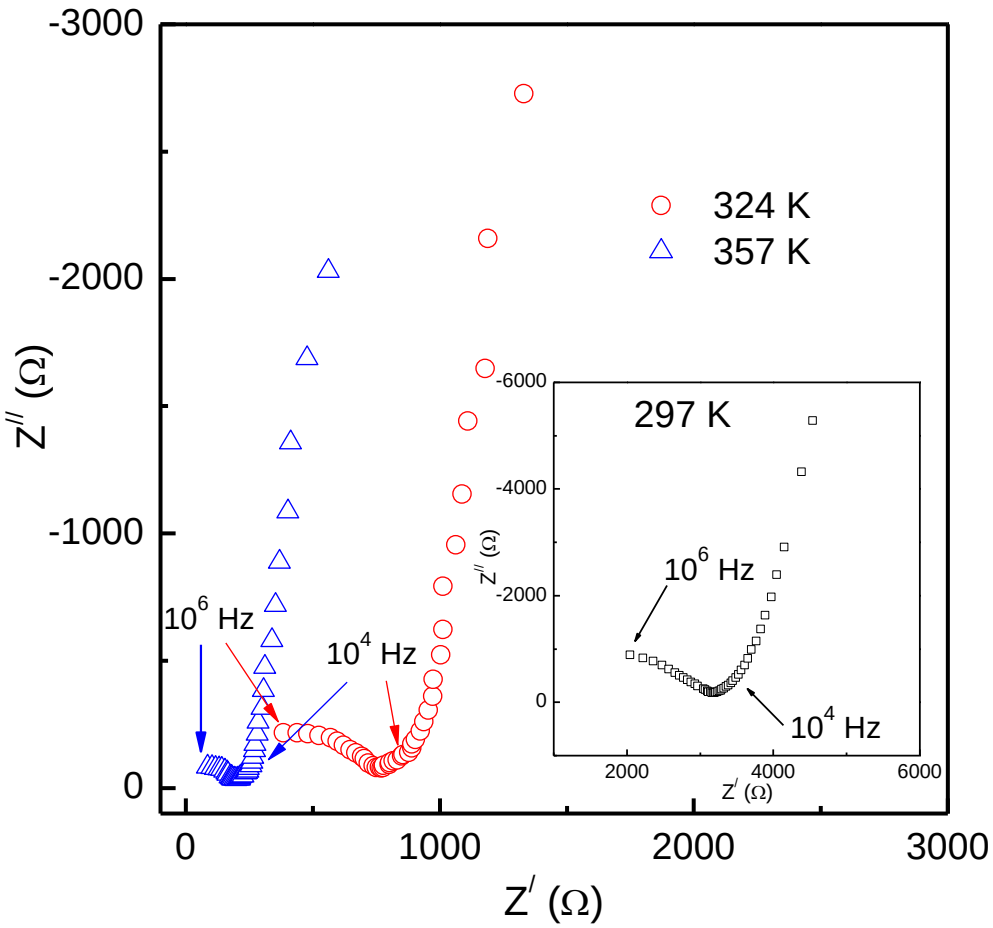

Figure 6. 9 Impedance plots of the data shown in Figure 6.8. The frequency range used for the power law fit is marked by arrows[1].

Table 6. 4 DC-conductivity values of $Li_{6.5}La_{2.5}Ba_{0.5}ZrTaO_{12}$ which were obtained from the frequency-independent plateaus (10^4 to 10^6 Hz) of the impedance spectra shown in Figure 6.8. For comparison, data from other ion conductors, partly showing very high ionic conductivity, are also listed[1].

Solid electrolyte	T (K)	σ_0 (S cm^{-1})	p	E_a (eV)	Reference
$Li_{6.5}La_{2.5}Ba_{0.5}ZrTaO_{12}$	297	9.0×10^{-5}	≈ 0.67	0.57(1) (220 to 290 K)	present
	324	3.2×10^{-4}	≈ 0.76	0.37(1) (330 to 500 K)	work
	357	1.2×10^{-3}	≈ 0.82		
Li_4SiO_4	396	4.0×10^{-8}	0.68	0.83 (333 to 453 K)	21
$Li_{0.18}La_{0.61}TiO_3$	303	1.0×10^{-4}	0.60	0.41 (370 to 523 K)	22
$Li_7La_3Zr_2O_{12}$ (tetragonal phase)	300	1.2×10^{-6}	0.77	0.52 (350 to 400 K)	31
$Li_7La_3Zr_2O_{12}$ (cubic phase)	300	1×10^{-4}	–	0.32 (290 to 573 K)	25

In the Arrhenius plot of Figure 6.10, the $\sigma(0)$ values are shown together with conductivity data, which was taken from previous impedance studies. Above 330 K, the DC-conductivities, $\sigma(0)$, obey an Arrhenius law characterized by activation energy, E_a, of approximately 0.34 eV which is consistent with results reported in the literature for other garnet-type electrolytes. Below 300 K the activation energy increases, which may indicate a change in conduction mechanism.[2-9,24-30] For comparison, the garnets $Li_7La_3Zr_2O_{12}$ (cubic modification), $Li_6BaLa_2Ta_2O_{12}$, $Li_6BaLa_2Nb_2O_{12}$, $Li_{5.5}La_3Nb_{1.75}In_{0.25}O_{12}$, and $Li_5La_3Nb_2O_{12}$ show activation energies of 0.31, 0.40, 0.44, 0.51, and 0.43 eV, respectively[4,6-8,24-30].

In order to estimate a macroscopic (solid-state) Li diffusion coefficient (D), we have converted the $\sigma(0)$ values according to the Nernst-Einstein relation, equation [4.4].

Figure 6.10 shows that the solid-state diffusion coefficients D ranging from 10^{-12} to 10^{-10} cm^2s^{-1} between 230 K and 280 K, and from 10^{-10} to 10^{-7} cm^2s^{-1} when temperatures between 320 K and 500 K. This is in good agreement with results recently reported in the literature[18].

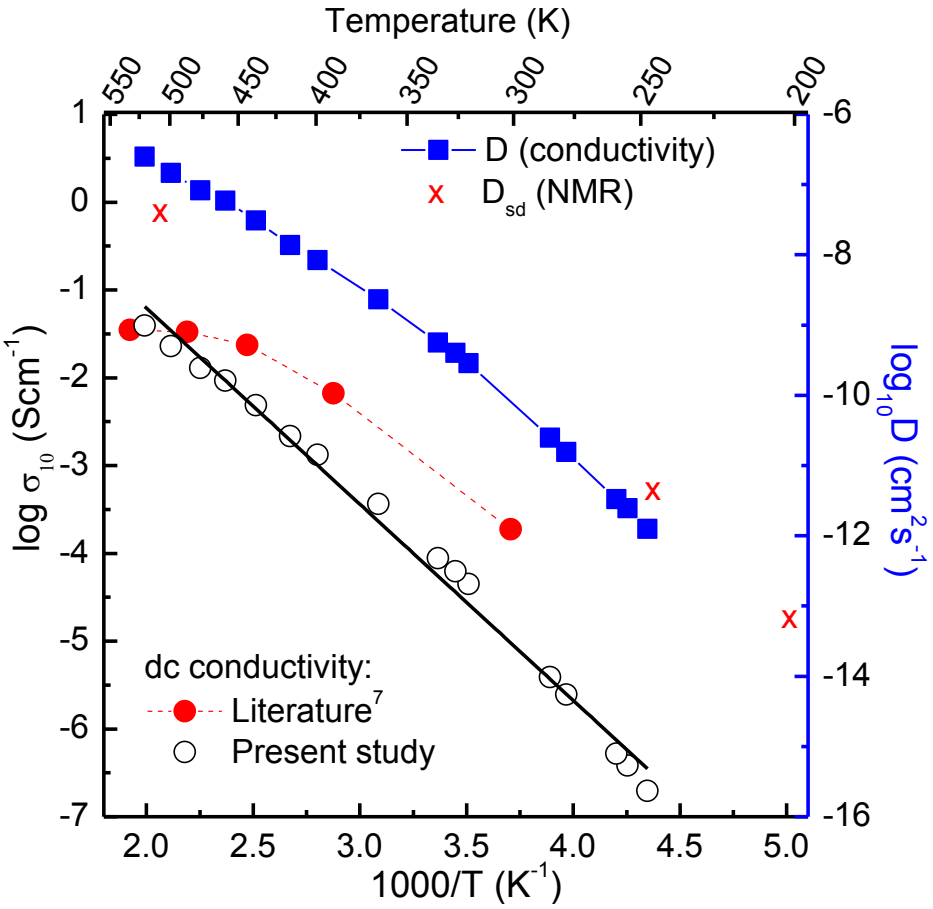

Figure 6. 10 Temperature dependence of σ_{DC} as well as D, calculated using equation [4.4] for polycrystalline $Li_{6.5}La_{2.5}Ba_{0.5}ZrTaO_{12}$. Solid lines represent fits using an Arrhenius law, $\sigma_{DC}T \propto \exp(-E_a/(k_BT))$. For comparison, self-diffusion coefficients estimated from ^{7}Li NMR spectroscopy are also included[1].

6.2.3 ^{7}Li NMR line shape measurements

For comparison with the conductivity results presented, we have recorded variable-temperature ^{7}Li MAS NMR line shapes to obtain first insight of the Li dynamics from a microscopic point of view. In general, at a sufficiently low temperature, the line width of an NMR spectrum acquired under static, that is non-rotating conditions, is dipolarly broadened due to the various Li-Li interactions present in a crystalline solid. With increasing temperature, these (homonuclear) dipole-dipole interactions are increasingly averaged due to the onset of (local) rapid Li hopping processes characterized by jump rates on the order of some kHz. By plotting the line width δ as a function of temperature T, a so-called motional narrowing (MN) curve is obtained, which can be used to roughly estimate Li diffusion parameters, such as jump rates and activation energies[32]. Starting from $\delta = \delta_{rl}$, which is the rigid-lattice line width, δ continuously decreases. In the limit of extreme narrowing, δ finally reaches δ_{en}, which is solely governed by the inhomogeneities of the external magnetic field used.

In agreement with the results from impedance spectroscopy, in the case of $Li_{6.5}La_{2.5}Ba_{0.5}ZrTaO_{12}$ motional narrowing sets in at extremely low temperatures. ^{7}Li NMR spectra, which were recorded at different temperatures, are shown in Figure 6.11, the corresponding motional narrowing curve is given in Figure 6.12[1].

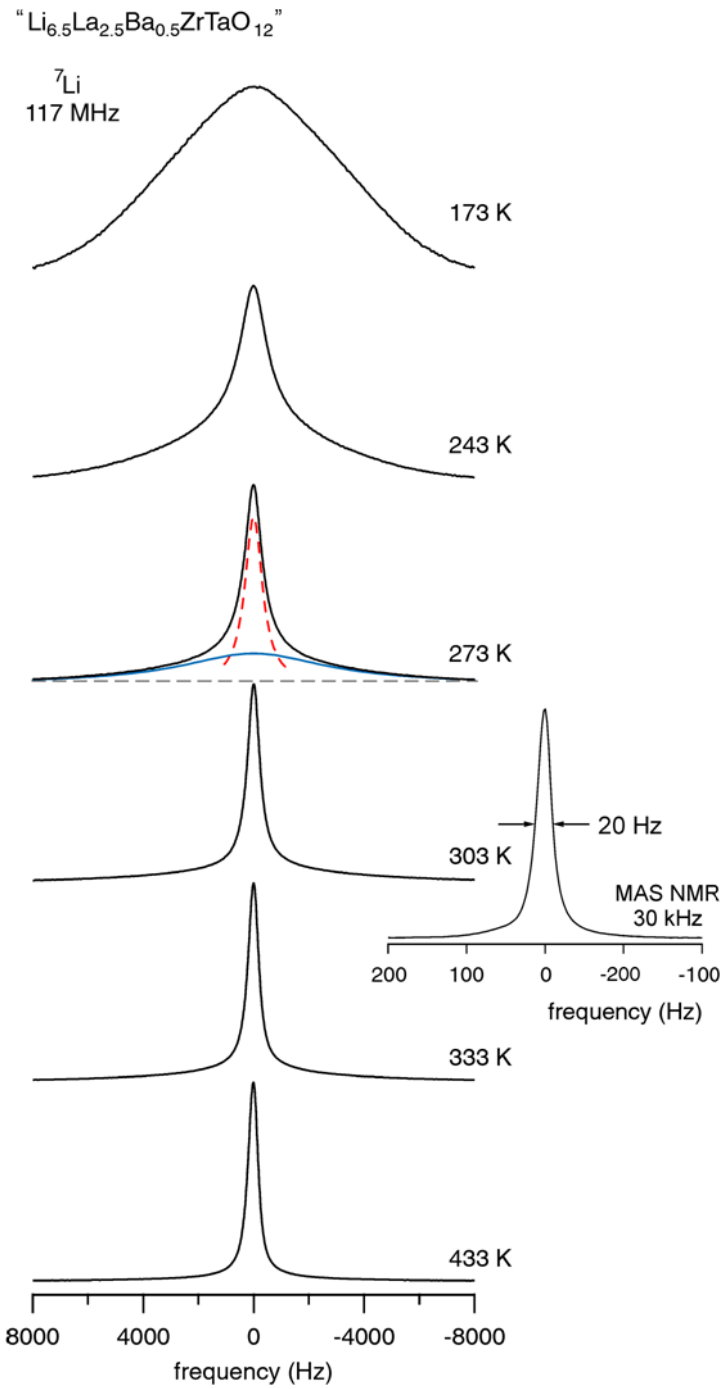

Figure 6. 11 ^{7}Li NMR spectra (117 MHz) of $Li_{6.5}La_{2.5}Ba_{0.5}ZrTaO_{12}$ recorded at various temperatures indicated. At intermediate *T*, the spectra are composed of two components reflecting fast and slow Li ions in the garnet. As an example, the spectrum recorded at 273 K has been fitted with a sum of a narrow Lorentzian (dashed line) and a broad Gaussian (solid line). The number fraction of fast Li ions turns out to be approximately 50 % at this temperature. Inset: ^{6}Li MAS NMR spectrum recorded at a spinning speed of 30 kHz and ambient bearing gas[1].

For example, in Figure 6.12, at T = 200 K ($\approx T_{onset}$), the line width (full width at half maximum) is already decreased from $\delta_{rl} \approx 8$ kHz to δ = 7 kHz. At this temperature the mean Li jump rate, $1/\tau$ is expected to be in the order of 10^3 s^{-1}. Using the well-known Einstein-Smoluchowski equation:

$$D_{sd} = d_{m^2} / (6\tau) \qquad [6.1]$$

This yields a self-diffusion coefficient of $D_{sd} \approx 7 \times 10^{-14}$ cm^2s^{-1}. Here, a mean jump distance d_m = 2 Å was used to estimate D_{sd}. The value obtained is in good agreement with those probed by impedance spectroscopy when the D values plotted in Figure 6.10 are extrapolated to lower temperatures.

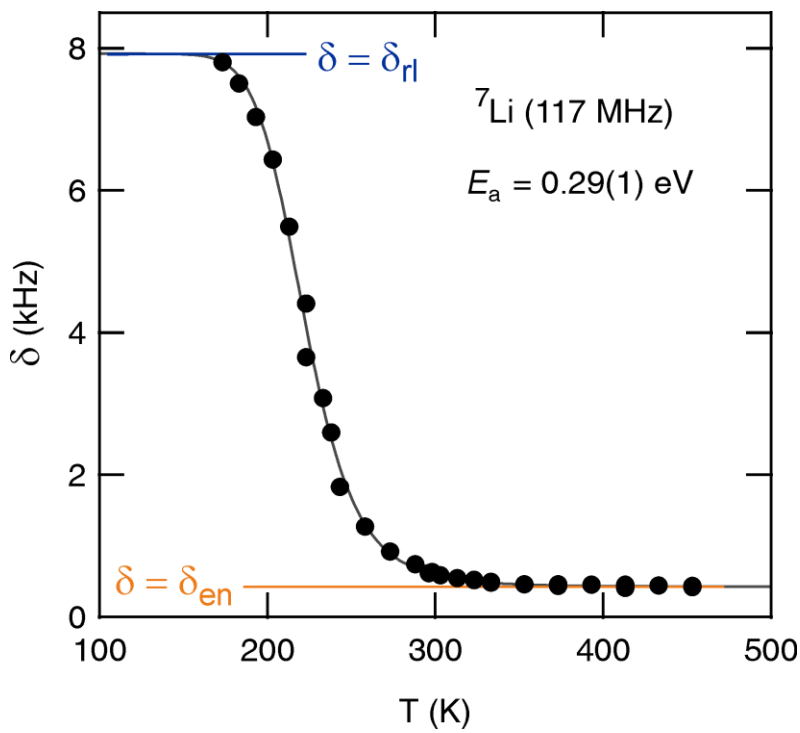

Figure 6. 12 Motional narrowing of the ^{7}Li NMR spectra (117 MHz) for $Li_{6.5}La_{2.5}Ba_{0.5}ZrTaO_{12}$. The (overall) line width δ (fwhm, full width at half maximum) is plotted as a function of temperature T. Starting from δ_{rl} being slightly larger than 8 kHz the line width is reduced to δ_{en} = 420 Hz when T is higher than 300 K. The solid line shows a fit according to the model of Hendrickson and Bray[33,34] yielding an activation energy of 0.29(1) eV[1].

The Figure 6.11 shows that at 243 K the NMR line width is significantly narrowed revealing a so-called two-component line shape. In this intermediate temperature range the spectra are composed of a broad Gaussian superimposed by a motionally narrowed Lorentzian shaped line. Such a heterogeneous line narrowing has already been observed for other crystalline garnets by Koch et al.[33] This indicates a distribution of jump rates which is present at least in the range of extremely low temperatures (T < 300 K). This may be the direct consequence of an irregularly shaped potential landscape that the hopping ions are exposed to.

In the present case, almost the full motional narrowing curve could be detected as shown in Figure 6.12. Thus, the inflexion point of the curve can be accurately determined. Here, δ reaches $\delta_{rl}/2$ when T is increased to $T = T_{infl.} = 230$ K. At this temperature the jump rate $1/\tau$ can be approximated by $1/\tau(T_{infl}) = 2\pi \times \delta_{rl}$. Using $\delta_{rl} = 8$ kHz, the corresponding self-diffusion coefficient, $D_{sd}(T_{infl}) = d^2\ 2\pi\delta_{rl}/6$, is given by $D_{sd}(230\text{ K}) \approx 3.5 \times 10^{-12}\ \text{cm}^2\text{s}^{-1}$, confirming the fast ion conduction process presented in Figure 6.10. Moreover, the expression introduced by Waugh and Fedin, $E_{a,MN}/\text{eV} = 1.617 \times 10^{-3} \cdot T_{onset}/\text{K}$, can be used to crudely estimate activation energy from a $\delta(T)$ curve. Inserting $T_{onset} = 200$ K yields $E_{a,MN} = 0.31$ eV. Almost the same value, 0.29 eV, is obtained when the motional narrowing curve is analyzed according to the model of Hendrickson and Bray[24,34,35]. Interestingly, the activation energy roughly deduced from NMR line shape measurements is lower than that directly probed by DC-conductivity measurements in the same temperature range. However, it is worth noting that changes in NMR line widths measurements are sensitive to Li dynamics taking place on a shorter

length-scale, rather than DC-conductivity measurements. The later are sensitive to long-range Li transport.

The rapid Li exchange process is also reflected by the ^{6}Li MAS NMR spectrum shown in the inset Figure 6.11, which was recorded with ambient bearing gas pressure and at a rotation frequency of 30 kHz. The spectrum is composed of a single NMR line whose line width (fwhm) amounts to no more than 20 Hz. Besides external spinning, an extremely fast Li exchange process, as probed by the static variable-temperature NMR line shape recorded, may additionally cause such a narrow NMR signal. Preliminary ^{7}Li NMR spin-lattice relaxation measurements performed at $\omega_0/2\pi$ = 117 MHz indicate that the diffusion-induced rate peak $1/T_1(1/T)$ shows up at approximately T = 480 K. According to the condition $\omega_0\tau \approx 1$, which is valid at the temperature where the peak maximum appears[12,36,37], at $T \approx 480$ K the Li jump rate is expected to be in the order of 7.3×10^8 s^{-1} which corresponds to $D_{sd} \approx 4.9 \times 10^{-8}$ cm^{2}s^{-1} (Figure 6.10).

6.2.4 Chemical stability

The chemical stability of $Li_{6.5}La_{2.5}Ba_{0.5}ZrTaO_{12}$ with temperature is studied using *in-situ* PXRD analysis as given in Figure 6.13[1]. It shows high stability even after heating at 773 K. Figure 6.14 shows the compatibility of $Li_{6.5}La_{2.5}Ba_{0.5}ZrTaO_{12}$ in water. The water treated garnet is structurally stable up to 973 K as shown in Figure 6.14.

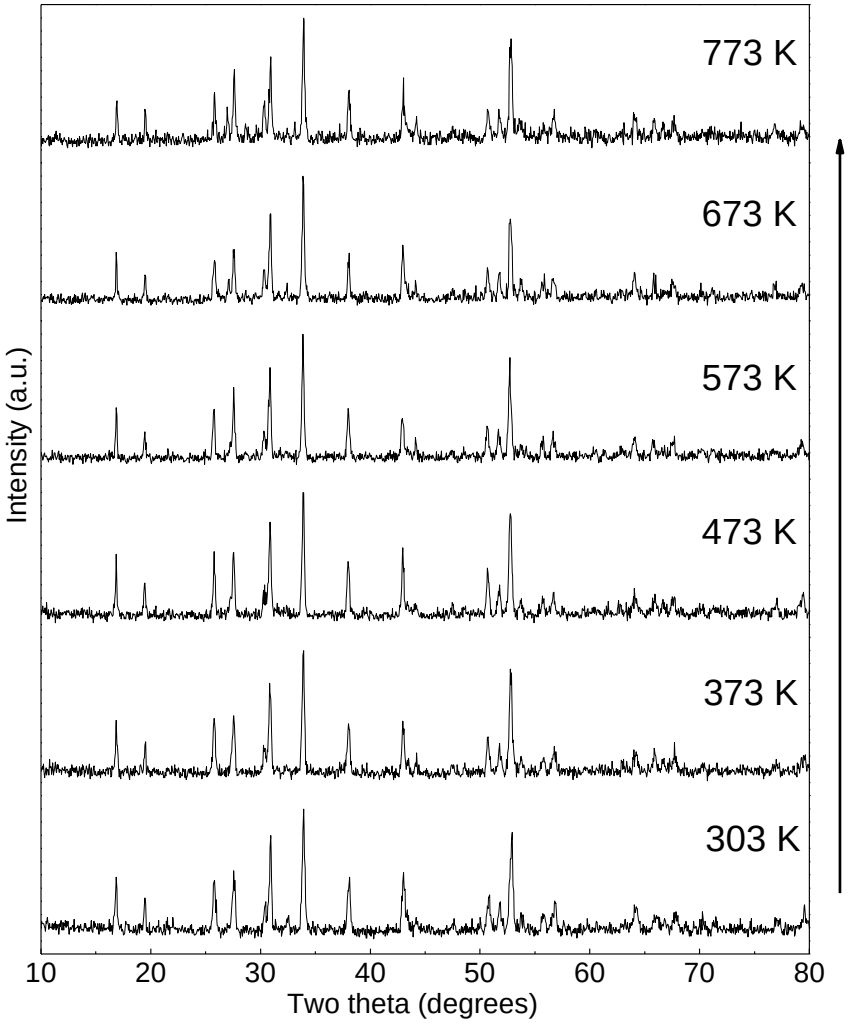

Figure 6. 13 *In-situ* PXRD pattern of $Li_{6.5}La_{2.5}Ba_{0.5}ZrTaO_{12}$ as a function of temperature. The garnet is stable during the heat treatment up to 773 K[1].

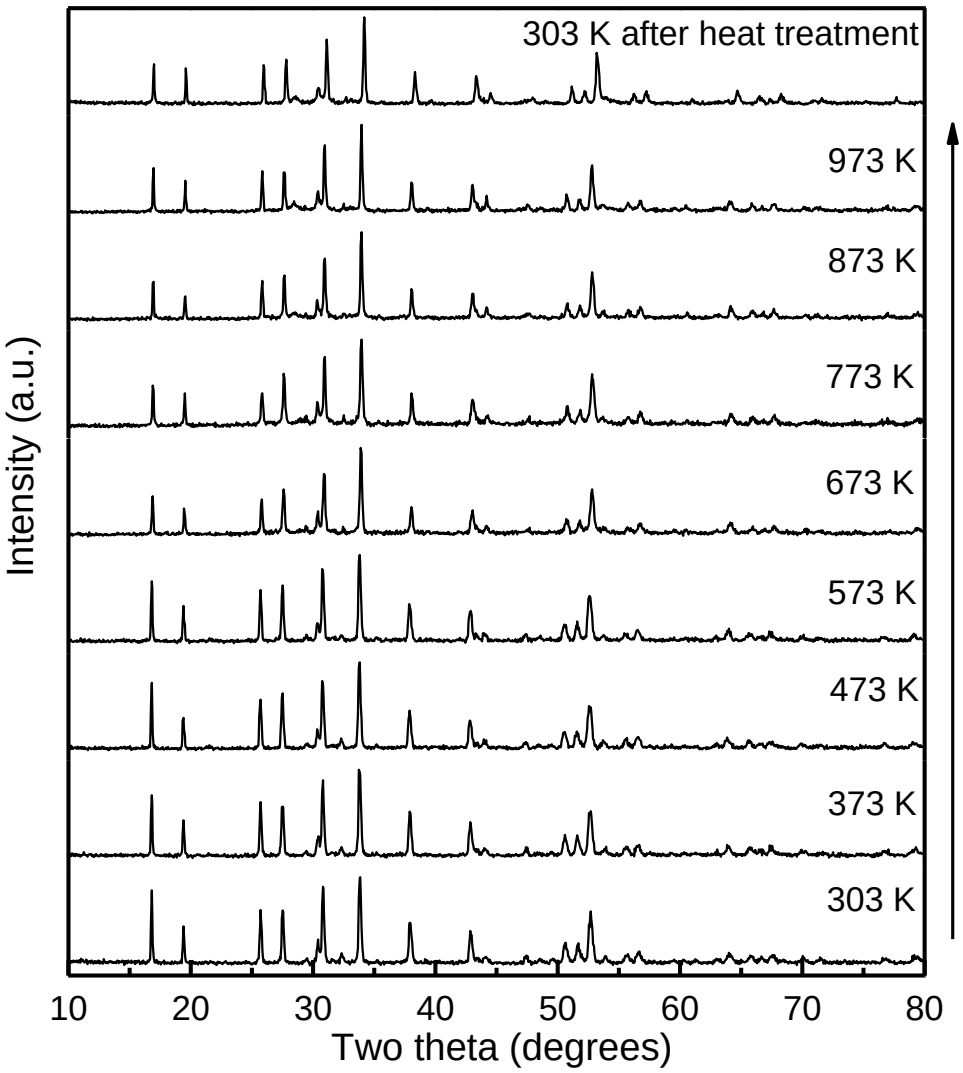

Figure 6. 14 *In-situ* PXRD pattern of water treated $Li_{6.5}La_{2.5}Ba_{0.5}ZrTaO_{12}$ as a function of temperature. The garnet structure is maintained during reaction with water and is stable with temperature up to 973 K.

The compatibility and chemical stability of $Li_{6.5}La_{2.5}Ba_{0.5}ZrTaO_{12}$ against the high-voltage cathode material $Li_2FeMn_3O_8$ was studied by heating a mixture of the two compounds at elevated temperatures. Interestingly, despite the high Li diffusivity probed, cubic $Li_{6.5}La_{2.5}Ba_{0.5}ZrTaO_{12}$ was found to be stable up to 673 K (Figure 6.15), while at 873 K the garnet seems to react with the cathode material. The corresponding PXRD

pattern is solely governed by the peaks of the spinel $Li_2FeMn_3O_8$ (Figure 6.15). The chemical stability of $Li_{6.5}La_{2.5}Ba_{0.5}ZrTaO_{12}$ in the presence of a commonly used cathode material such as $Li_2FeMn_3O_8$ makes it a promising candidate for further battery application studies.

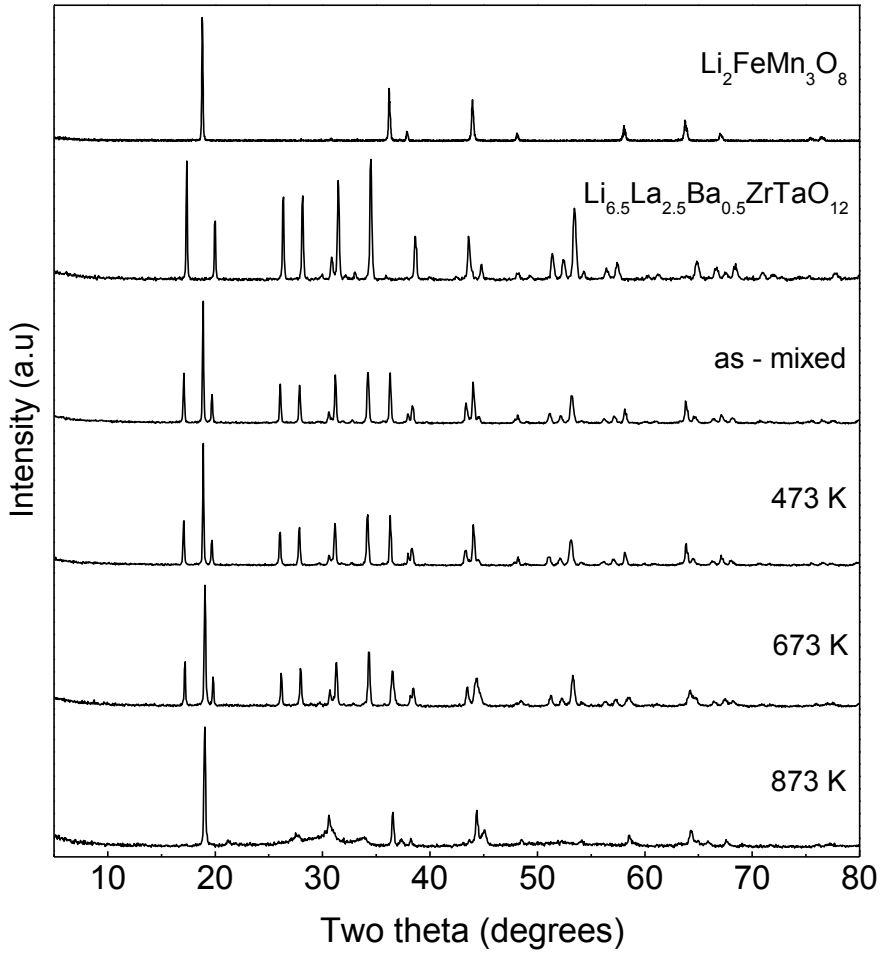

Figure 6. 15 PXRD pattern of a mixture of $Li_{6.5}La_{2.5}Ba_{0.5}ZrTaO_{12}$ and $Li_2FeMn_3O_8$ (1:1 wt. % ratio) illustrating the chemical compatibility of the garnet-like oxide with a high-voltage cathode material. The mixtures have been heated at 473 K, 673 K and 873 K for 24 h in air[1].

6.3 Summary

In summary, the garnet-type $Li_{6.5}La_{2.5}Ba_{0.5}ZrTaO_{12}$ is a very promising oxide potentially to be used as a highly conducting electrolyte in future all-solid-state lithium-ion batteries. At room temperature (300 K), the Li conductivity (σ_{DC}) characterizing long-range ion transport, is of the order of 10^{-4} Scm^{-1}. Rapid Li diffusivity was confirmed by ^{7}Li NMR line shape measurements clearly revealing that motional narrowing of the line width sets in at temperatures as low as 220 K, *i. e.*, well below ambient temperature. Hence, NMR line shape measurements indicate that σ is solely governed by ionic conductivity. Despite of the high Li^{+} conductivity of garnet-type $Li_{6.5}La_{2.5}Ba_{0.5}ZrTaO_{12}$, the oxide shows a remarkably good chemical stability when heated together with a cathode material such as $Li_2FeMn_3O_8$, making it a highly suitable candidate for applications in all-solid-state energy systems.

Chapter Seven: **Conclusions and future work**

7.1 Conclusions

7.1.1 Conclusions on the effect of Y substitution for Nb in $Li_5La_3Nb_2O_{12}$ on Li ion conductivity of garnet-like $Li_5La_3Nb_{2-x}Y_xO_{12-\delta}$

The substitution of Y for Nb in the $Li_5La_3Nb_2O_{12}$ was achieved by solid state reaction at elevated temperatures (1100 °C). A single-phase cubic garnet-type structure was found for doping levels up to x = 0.25 in $Li_5La_3Nb_{2-x}Y_xO_{12-\delta}$. Small amounts of second phase were observed at high Y doping, suggesting that the doping limit of Y is 25 %. It is clear from the microscopy studies that the doping of Y has improved the sinterability of the garnet oxide. A single peak close to 0 ppm of chemical shift was observed for all the members, as was also seen in the literature.

A similar trend to the literature was found for the AC impedance data, which shows bulk and grain-boundary contributions to the total electrical conductivity. Comparable electrical conductivity to that of the parent compound $Li_5La_3Nb_2O_{12}$ was observed for $Li_5La_3Nb_{2-x}Y_xO_{12-\delta}$ with activation energy 0.43-0.51 eV at 25-200 °C. High ionic conductivities of 1.34 x 10^{-5} and 1.44 x 10^{-5} Scm^{-1} were exhibited by x = 0.05 and 0.1 members of $Li_5La_3Nb_{2-x}Y_xO_{12-\delta}$, respectively at 23 °C, which is about an order of magnitude lower than that of the fast Li ion conducting cubic $Li_7La_3Zr_2O_{12}$. The *in-situ* PXRD shows that $Li_5La_3Nb_{1.95}Y_{0.05}O_{11.95}$ is thermally stable in the temperature range (30-325 °C) used for AC impedance measurements. The chemical reactivity of $Li_5La_3Nb_{1.95}Y_{0.05}O_{12-\delta}$ with the cathode $Li_2FeMn_3O_8$ showed that the compound is chemically compatible with the electrode by heating up to 400 °C for 24 h.

7.1.2 Conclusions on the effect of Li concentration on the ionic conductivity of garnet-like $Li_{5+2x}La_3Nb_{2-x}Y_xO_{12}$

The garnet-like $Li_{5+2x}La_3Nb_{2-x}Y_xO_{12}$ was successfully synthesized up to x = 0.75. The PXRD refinements show a cubic crystal structure with space group *Ia*-3*d* for all the members. The electrical conductivity and diffusivity increased with increased Li stuffing as expected. Similar conductivity (10^{-4} Scm^{-1} at 24 °C) to that of the highest conducting garnet-like member, $Li_7La_3Zr_2O_{12}$, was observed for $Li_6La_3Nb_{1.5}Y_{0.5}O_{12}$ and $Li_{6.5}La_3Nb_{1.25}Y_{0.75}O_{12}$. *In-situ* PXRD studies proved that $Li_{5+2x}La_3Nb_{2-x}Y_xO_{12}$ showed higher structural stability in water compared to the parent compound. A promising chemical stability with temperature, water, high voltage cathode spinels ($Li_2MMn_3O_8$, M = Co, Fe), and carbon anode was observed for $Li_{5+2x}La_3Nb_{2-x}Y_xO_{12}$. The advantages mentioned above such as very high Li^+ conductivity and high chemical stability make $Li_{5+2x}La_3Nb_{2-x}Y_xO_{12}$ a strong candidate for future battery research.

7.1.3 Conclusions on macroscopic and microscopic studies on the Li^+ transport properties of cubic garnet-like $Li_{6.5}La_{2.5}Ba_{0.5}ZrTaO_{12}$

Successful reproducibility in synthesis and properties was achieved for garnet-type $Li_{6.5}La_{2.5}Ba_{0.5}ZrTaO_{12}$. Impurity due to ^{27}Al during the synthesis step was observed in both PXRD and Al NMR analysis and is common with the garnet-like compounds synthesized via similar methods. The bulk and grain-boundary contributions to the total conductivity were revealed from AC impedance analysis. A high Li ion conductivity of the order of 10^{-4} Scm^{-1} at room temperature (300 K) was observed, which indicates a long-range transport. ^7Li NMR line shape measurements confirm rapid diffusivity and show the motional narrowing of the line width sets in at temperatures as low as 220 K,

well below ambient temperature. ^{7}Li NMR line shape measurements indicate that σ is solely governed by ionic conductivity. *In-situ* PXRD analysis indicates that $Li_{6.5}La_{2.5}Ba_{0.5}ZrTaO_{12}$ shows significant chemical stability with temperature, water, and high voltage cathode, $Li_2FeMn_3O_8$. All the above mentioned properties make $Li_{6.5}La_{2.5}Ba_{0.5}ZrTaO_{12}$ a very promising oxide to be used as highly conducting electrolyte in future all-solid-state lithium-ion batteries.

7.2 Proposed future work

More careful studies are needed to understand the exact composition of all garnet-like materials synthesized. Inductively coupled plasma (ICP) studies, transmission electron microscopy (TEM) and electron diffraction could be adopted to further understand the structure. The compatibility between electrolyte and electrode layers needs to be studied using TEM technique. For this, the samples could be prepared by applying a layer of cathode material on the electrolyte (pellet form). The weight loss in TGA needs to be quantitatively analysed using mass spectroscopy. Further research by employing different synthesis techniques such as sol-gel chemistry to tune the ionic conductivity, sintering temperature, and morphology of garnet-like oxides need to be performed. Composite approach can also be used to develop solid electrolytes with conductivity > 10^{-4} Scm^{-1} at ambient temperature. Laboratory scale battery tests can be performed with the currently developed promising garnet-like compounds mentioned in Chapter 5 and 6. Fabrication of thin films from the solid state electrolytes can contribute more to the solid state battery research.

References

Chapter 2

(1) Tarascon, J. M.; Armand, M. *Nature* **2001**, *414*, 359-367.

(2) Zu, C. -X.; Li, H. *Energy Environ. Sci*. **2011**, *4*, 2614–2624.

(3) Etacheri, V.; Marom, R.; Elazari, R.; Salitra, G.; Aurbach, D. *Energy Environ. Sci*. **2011**, *4*, 3243–3262.

(4) Scrosati, B.; Hassoun, J.; Sun, Y. -K. *Energy Environ. Sci*. **2011**, *4*, 3287–3295.

(5) Goodenough, J. B.; Kim, Y. *Chem. Mater.* **2010**, *22*, 587-603.

(6) Manthiram, A. *J. Phys. Chem. Lett.* **2011**, *2*, 176-184.

(7) Xu, X.; Bates, J. B.; Jellison G. E.; Hart, F. X.; *J. Electrochem. Soc*. **1997**, *144*, 524–532.

(8) Dunn, B.; Kamath, H.; Tarascon, J. -M. *Science* **2011**, *334*, 928-935.

(9) Nishi, Y. *Chem. Rec*. **2001**, *1*, 406–413.

(10) Ceder, G.; Chiang, Y.; Sadoway, D.; Aydinol, M.; Jang, Y.; Huang, B. *Nature* **1998**, *392*, 694-696.

(11) Nazri, G. –A.; Pistoia, G. *Lithium Batteries Science and Technology*, Kluwer Academic Publishers, **2004**.

(12) Linden, D.; Reddy, T. B. *Handbook of Batteries*, Mc-Graw-Hill, **2008**.

(13) Patil, A.; Patil, V.; Shin, D. W.; Choi, J. -W.; Paik, D. –S.; Yoon, S. –J. *Mater. Res. Bull.* **2008**, *43*, 1913-1942.

(14) Owen, J. R. *Chem. Soc. Rev.* **1997**, *26*, 259-267.

(15) Thangadurai, V.; Weppner, W. *Ionics* **2006**, *12*, 81–92.

(16) Fenton, D. E.; Parker, J. M.; Wright, P. V. *Polymer* **1973**, *14*, 589.

(17) Armand, M. B.; Chabagno, J. M.; Duclot, M. in *Second International Meeting on Solid Electrolytes*, St Andrews, Scotland, 20-22 Sept., **1978**.

(18) Armand, M. B.; Chabagno, J. M.; Duclot, M. Extended Abstract; "Poly-ethers as solid electrolytes", in P. Vashitshta, J.N. Mundy, G.K. Shenoy, *Fast ion Transport in Solids. Electrodes and Electrolytes*, North Holland Publishers, Amsterdam, **1979**.

(19) Armand, M. B. in MacCallum, J. R. and Vincent, C. A. (eds.), *Polymer Electrolyte Reviews-1*, Elsevier Applied Science, New York, **1987**.

(20) Croce, F.; Appetecchi, G. B.; Persi, L.; Scrosati, B. *Nature* **1998**, *394*, 456-458.

(21) Stephan A. M.; Nahm, K. S. *Polymer* **2006**, *47*, 5952-5964.

(22) Udomvech, A.; Kerdcharoen, T.; Osotchan, T. *Chem. Phys. Lett.* **2005**, *406*, 161–166.

(23) Coleman, J. N.; Khan, U.; Blau, W. J.; Gun'ko, Y. K. *Carbon* **2006**, *44*, 1624-1652.

(24) Tang, C.; Hackenberg, K.; Fu, Q.; Ajayan, P. M.; Ardebili, H. *Nano Lett.* **2012**, *12*, 1152-1156.

(25) Thangadurai, V.; Weppner, W. *Ionics* **2006**, *12*, 81-92.

(26) Thangadurai, V.; Weppner, W. *J. Power Sources* **2005**, *142*, 339-344.

(27) Xu, X.; Bates, J. B.; Jellison, G. E.; Hart, F. X. *J. Electrochem. Soc*. **1997**, *144*, 524-532.

(28) Kawai, H.; Kuwano, J. *J. Electrochem. Soc.* **1994**, *141*, L78-L79.

(29) Robertson, A. D.; West, A. R.; Ritchie, A .G. *Solid State Ionics* **1997**, *104*, 1-11.

(30) Inaguma, Y.; Liquan, C.; Itoh, M.; Nakamura, T.; Uchida, T.; Ikuta, H.; Wakihara, M. *Solid State Commun*. **1993**, *86*, 689-693.

(31) Adachi, G.Y.; Imanaka, N.; Aono, H. *Adv. Mater.* **1996**, *8*, 127-135.

(32) Harada, Y.; Hirakoso, Y.; Kawai, H.; Kuwano, J. *Solid State Ionics* **1999**, *121*, 245-251.

(33) Bohnke, O.; Bohnke, C.; Fourquet, J. -L. *Solid State Ionics* **1996**, *91*, 21-31.

(34) Itoh, M.; Inaguma, Y.; Jung, W. H.; Shan, L.; Nakamura, T. *Solid State Ionics* **1994**, *70/71*, 203-207.

(35) Inaguma, Y.; Matsui, Y.; Yu, J.; Shan, Y. J.; Nakamura, T.; Itoh, M. *J. Phys. Chem. Solids* **1997**, *58*, 843-852.

(36) Harada, Y.; Ishigaki, T.; Kawai, H.; Kuwano, J. *Solid State Ionics* **1998**, *108*, 407-413.

(37) Harada, Y.; Hirakoso, Y.; Kawai, H.; Kuwano, J. *Solid State Ionics* **1999**, *121*, 245-251.

(38) Li, J.; Wen, Z.; Xu, X.; Zhu, X.; *Solid State Ionics* **2005**, *176*, 2269-2273.

(39) Okumura, T.; Yokoo, K.; Fukutsuka, T.; Uchimoto, Y.; Saito, M.; Amezawa, K. *J. Power Sources* **2009**, *189*, 536-538.

(40) Okumura, T.; Ina, T.; Orikasa, Y.; Arai, H.; Uchimoto, Y.; Ogum, Z.; *J. Mater. Chem.* **2011**, *21*, 10061-10068.

(41) Stramare, S.; Thangadurai, V.; Weppner, W. *Chem. Mater.* **2003**, *15*, 3974-3990.

(42) Knauth, P. *Solid State Ionics* **2009**, *180*, 911–916.

(43) Bohnke, O. *Solid State Ionics* **2008**, *179*, 9-15.

(44) Cretin, M.; Fabry, P. *J. European Ceram. Soc.* **1999**, *19*, 2931-2940.

(45) No, H. A. *Acc. Chem. Res.* **1994**, *27*, 265-270.

(46) Kobayashi, Y.; Tabuchi, M.; Nakamura, O. *J. Power Sources* **1997**, *68*, 407-411.

(47) Aono, H.; Sugimoto, E.; Sadaoka, Y.; Imanaka, N.; Adachi, G. -Y. *J. Electrochem. Soc.* **1993**, *140*, 1827-1833.

(48) Arbi, K.; Rojo, J. M.; Sanz, J. *J. Eur. Ceram. Soc.* **2007**, *27*, 4215–4218.

(49) Pinus, I. Y.; Khoroshilov, A. V.; Gavrichev, K. S.; Tarasov, V. P.; Yaroslavtsev, A. B. *Solid State Ionics* **2012**, *212*, 112-116.

(50) Arbi, K.; Par´ıs, M. A.; Sanz, J. *Dalton Trans.* **2011**, *40*, 10195- 10202.

(51) Qui, D. T.; Hamdoune, S.; Soubeyroux, J. L.; Prince, E. *J. Solid State Chem.* **1988**, *72*, 309-315.

(52) Funke, K. *Prog. Solid State Chem.* 1993, **22**, 111-195.

(53) Losilla, E. R.; Aranda, M. A. G.; Martinez-Lara, M.; Bruque, S. *Chem. Mater.* **1997**, *9*, 1678-1685.

(54) O'Callaghan, M.P.; Lynham, D. R.; Cussen, E. J.; Chen, G. Z. *Chem. Mater.* **2006**, *18*, 4681-4689.

(55) Cussen, E. J. *Chem. Commun.* **2006**, 412-413.

(56) Thangadurai, V.; Kaack, H.; Weppner, W. J. F. *J. Am. Ceram. Soc.* **2003**, *86*, 437-440.

(57) Abbattista. F.; Vallino, M.; Mazza, D. *Mater. Res. Bull.* **1987**, *22*, 1019-1027.

(58) Mazza, D. *Mater. Lett.* **1988,** *7*, 205-207.

(59) Hyooma, H; Hayashi, K. *Mat. Res. Bull.* **1988**, *23*, 1399-1407.

(60) Murugan, R.; Thangadurai, V.; Weppner, W. *Angew. Chem. Int. Ed.* **2007**, *46*, 7778-7781.

(61) Awaka, J.; Kijima, N.; Hayakawa, H.; Akimoto, J. *J. Solid State Chem.* **2009**, *182*, 2046-2052.

(62) Percival, J.; Slater, P. R. *Solid State Commun.* **2007**, *142*, 355-357.

(63) E. J. Cussen, *J. Mater. Chem.* **2010**, *20*, 5167-5173.

(64) Thangadurai, V.; Weppner, W. *Adv. Funct. Mater.* **2005**, *15*, 107-112.

(65) O'Callaghan, M. P.; Cussen, E. J. *Chem. Commun.* **2007**, 2048-2050.

(66) Rangasamy, E.; Wolfenstine, J.; Sakamoto, J. *Solid State Ionics* **2012**, *206*, 28-32.

(67) Ramzy, A.; Thangadurai, V. *Appl. Mater. Interfaces* **2010**, *2*, 385-390.

(68) Allen, J. L.; Wolfenstine, J.; Rangasamy, E.; Sakamoto, J. *J. Power Sources* **2012**, *206*, 315-319.

(69) Thangadurai, V.; Weppner, W. *J. Solid State Chem.* **2006**, *179*, 974–984.

(70) Percival, J.; Kendrick, E.; Slater, P. *Solid State Ionics* **2008**, *179*, 1666-1669.

(71) Kim, K. H.; Iriyama, Y.; Yamamoto, K.; Kumazaki, S.; Asaka, T.; Tanabe, K.; Fisher, C. A. J.; Hirayama, T.; Murugan, R.; Ogumi, Z. *J. Power Sources* **2011**, ***196***, 764–767.

(72) Kotobuki, M.; Munakata, H.; Kanamura, K.; Sato, Y.; Yoshida, T. *J. Electrochem. Soc*. **2010**, *157*, A1076-A1079.

(73) Ohta, S.; Kobayashi, T.; Asaoka, T. *J. Power Sources* **2011**, *196*, 3342-334.

(74) Shimonishi, Y.; Toda, A.; Zhang, T.; Hirano, A.; Imanishi, N.; Yamamoto, O.; Takeda, Y. *Solid State Ionics* **2011**, *183*, 48-53.

(75) Jin, Y.; McGinn, P. J. *J. Power Sources* **2011**, *196*, 8683-8687.

(76) Geiger, C. A.; Alekseev, E.; Lazic, B.; Fisch, M.; Armbruster, T.; Langner, R.; Fechtelkord, M.; Kim, N.; Pettke, T.; Weppner, W. *Inorg. Chem.* **2011**, *50*, 1089-1097.

(77) Kuhn, A.; Narayanan, S.; Spencer, L.; Goward, G.; Thangadurai, V.; Wilkening, M. *Phy. Rev. B* **2011**, *83*, 094302-1-11.

(78) Xie, H.; Alonso, J. A.; Li, Y.; Fernndez, M. T.; Goodenough, J. B. *Chem. Mater.* **2011**, *23*, 3587–3589.

(79) Murugan, R.; Weppner, W.; Schmid-Beurmann, P.; Thangadurai, V. *Mater. Sci. Eng. B* **2007**, *143*, 14-20.

(80) Cussen, E. J.; Yip, T. W. S. *J. Solid State Chem.* **2007**, *180*, 1832-1839.

(81) O'Callaghan, M. P.; Powell, A. S.; Titman, J. J.; Chen, G. Z.; Cussen, E. J. *Chem. Mater.* **2008**, *20*, 2360-2369.

(82) Murugan, R.; Thangadurai, V. *Ionics* **2007**, *13*, 195-203.

(83) O'Callaghan, M. P.; Cussen, E. J. *Solid State Sci.* **2008**, *10*, 390-395.

(84) Murugan, R.; Thangadurai, V.; Weppner, W. *Appl. Phys. A* **2008**, *91*, 615-620.

(85) Murugan, R.; Thangadurai, V.; Weppner, W. *J. Electrochem. Soc.* **2008**, *155*, A90-A101.

(86) Adams, S.; Rao, R. P. *J. Mater. Chem.* **2012**, *22*, 1426-1434.

(87) Percival, J.; Kendrick, E.; Smith, R. I.; Slater, P. R. *Dalton Trans.* **2009**, *26*, 5177-5181.

(88) Kuhn, A.; Epp, V.; Schmidt, G.; Narayanan, S.; Thangadurai, V.; Wilkening, M. *J. Phys. Condens. Matter* **2012**, *24*, 035901/1-8.

(89) Kumazaki, S.; Iriyama, Y.; Kim, K.; Murugan, R.; Tanabe, K.; Yamamoto, K.; Hirayama, T.; Ogumi, Z. *Electrochem. Commun.* **2011**, *13*, 509-512.

(90) Ohta, S.; Kobayashi, T.; Seki, J.; Asaoka, T. *J. Power Sources* **2012**, *202*, 332-335.

(91) Guyomard, D. *New Trends in Electochemical Technology*, *1*, Gordon and Breach, Amsterdam, **2000**.

(92) Whittingham, M. S. *Chem. Rev.* **2004**, *104*, 4271-4301.

(93) Mizushima, K.; Jones, P.C.; Wiseman, P. J.; Goodenough, J. B. *Mater. Res. Bull.* **1980**, *15*, 783-789.

(94) Dahn, J. R.; Von Sacken, U.; Juzkow, M. W.; Al-Janaby, H. *J. Electrochem. Soc.* **1991**, *138*, 2207-2211.

(95) Doh, C. H.; Kim, D. H.; Kim, H. S.; Shin, H. M.; Jeong, Y.D.; Moon, S. I.; Jin, B. S.; Eom, S.W.; Kim, H. S.; Kim, K. W.; Oh, D.H.; Veluchamy, A. *J. Power Sources* **2008**, *175*, 881-885.

(96) Gao, Y.; Yakovleva, M. V.; Ebner, W. B. *Electrochem. Solid State Lett.* **1998**, *1*, 117-119.

(97) Belov, D.; Yang, M. H. *Solid State Ionics* **2008**, *179*, 1816-1821.

(98) Belov, D.; Yang, M. H. *J. Solid State Electrochem.* **2008**, *12*, 885-894.

(99) Stewart, S. G.; Srinivasan, V.; Newman, J. *J. Electrochem. Soc.* **2008**, *155*, A664-A671.

(100) Martha, S. K.; Markevich, E.; Burgel, V.; Salitra, G.; Zinigrad, E.; Markovsky, B.; Sclar, H.; Pramovich, Z.; Heik, O.; Aurbach, D.; Exnar, I.; Buqa, H.; Drezen, T.; Semrau, G.; Schmidt, M.; Kovacheva, D.; Saliyski, N. J. *Power Sources* **2009**, *189*, 288-296.

(101) Lu, C. H.; Lin, Y. K. *J. Power Sources* **2009**, *189*, 40-44.

(102) Belharouak, I.; Sun, Y. K.; Lu, W.; Amine, K. *J. Electrochem. Soc.* **2007**, *154*, A1083-A1087.

(103) Benedek, R.; Thackeray, M. M.; Yang, L. H. *Phys. Rev. B* **1997**, *56*, 10707-10710.

(104) Wu, F.; Wang, L.; Wu, C.; Bai, Y.; Wang, F. *Mater. Chem. Phys.* **2009**, *115*, 707-711.

(105) Padhi, A. K.; Nanjundaswamy, K.S.; Masquelier, C.; Okada, S. Goodenough, J. *J. Electrochem. Soc.* **1997**, *144*, 1609-1613.

(106) Ellis, B.; Perry, L. K.; Ryan, D. H.; Nazar, L. F. *J. Am. Chem. Soc.* **2006**, *128*, 11416-11422.

(107) Kawai, H.; Nagata, M.; Tukamoto, H.; West, A. R. *J. Mater. Chem.* **1998**, *8*, 837-839.

(108) Kawai, H.; Nagata, M.; Tabuchi, M.; Tukamoto, H.; West, A. R. *Chem. Mater.* **1998**, *10*, 3266-3268.

(109) Lee, E. -S.; Huq, A.; Chang, H. -Y.; Manthiram, A. *Chem. Mater.* **2012**, *24*, 600-612.

(110) Dahn, J. R.; Sleigh, A. K.; Shi, H.; Reimers, J. N.; Zhong, Q.; Way, B. M. *Electrochim. Acta* **1993**, *38*, 1179-1191.

(111) Dahn, J. R.; Zheng, T.; Liu, Y. H.; Xue, J. S. *Science* **1995**, *270*, 590-598.

(112) Nishi, Y. *J. Power Sources* **2001**, *100*, 101-106.

(113) Dipietro, B.; Patriarca, M.; Scorsati, B. *J. Power Sources* **1982**, *8*, 289-299.

(114) Selwyn, L. S.; McKinnon, W. R.; Von Sacken, U.; Jones, C. A. *Solid state Ionics* **1987**, *22*, 337-344.

(115) Ozhuku, T.; Ueda, A.; Yamamoto, N. *J. Electrochem. Soc.* **1995**, *142*, 1431-1435.

(116) Shacklette, L. W.; Toth, J. E.; Murthy, N. S.; Baughman, R. H. *J. Electrochem. Soc.* **1985**, *132*, 1529-1535.

(117) Wen, C. J.; Huggins, R. A. *J. Solid State Chem.* **1981**, *37*, 271-278.

(118) Hatchard, T. D.; Dahn, J. R. *J. Electrochem. Soc.* **2004**, *151*, A838- A842.

(119) Obrovac, M. N.; Christensen, L. *Electrochem. Solid-State Lett.* **2004**, *7*, A93-A96.

(120) Kasavajjula, U.; Wang, C.; Appleby, A. J. *J. Power Sources* **2007**, *163*, 1003-1039.

(121) Li, H.; Huang, X.; Chen, L.; Zhou, G.; Zhang, Z.; Yu, D.; Jun Mo, Y.; Pei, N. *Solid State Ionics* **2000**, *135*, 181-191.

(122) Selwyn, L. S.; McKinnon, W. R.; Von Sacken, U.; Jones, C. A. *Solid state Ionics* **1987**, *22*, 337- 344.

(123) Wu, B.; Heidelberg, A.; Boland, J. J. *Nat. Mater.* **2005**, *4*, 525-529.

(124) Yao, Y.; McDowell, M. T.; Ryu, I.; Wu, H.; Liu, N.; Hu, L.; Nix, W. D.; Cui, Y. *Nano Lett.* **2011**, *11*, 2949-2954.

(125) Dann, S. E. *Reactions and Characterization of Solids*, John Wiley and Sons, **2002**.

(126) Gunzler, H.; Gremlich, H. -U. *IR spectroscopy An Introduction*, Wiley-VCH, Weinheim, **2002**.

(127) Pavoa, D.; Lampman, G.; Kriz, G. *Introduction to Spectroscopy*, Third ed.; Nelson Thomson Learning, **2001**.

(128) Zhou, W.; Wang, Z. L. *Scanning microscopy for nanotechnology: techniques and applications*, Springer, **2007**.

(129) West, A. R. *Solid State Chemistry and its Applications*, John Wiley and Sons, **1989**.

(130) Smart, L. E.; Moore, E. A. *Solid State Chemistry an Introduction*; Third edition.; Taylor and Francis Group, **2005**.

(131) Barsoukov, E.; Macdonald, J. R. *Impedance Spectroscopy Theory, Experiment, and Applications*; 2 ed.; John Wiley and Sons, **2005**.

(132) Duer, M. J. *Introduction to Solid-State Spectroscopy*, Black well publishing, **2004**.

Chapter 3

(1) Smart, L. E.; Moore, E. A. *Solid state chemistry an introduction*, CRC, Taylor and Francis, Third edition, **2008**.

(2) West, A. R. *Solid state chemistry and its applications*, John Wiley and sons, **1991**.

(3) Thangadurai, V.; Kaack, H.; Weppner, W. J. F. *J. Am. Ceram. Soc.* **2003**, *86*, 437-440.

(4) Percival, J.; Slater, P. R. *Solid State Commun.* **2007**, *142*, 355-357.

(5) E. J. Cussen, *J. Mater. Chem.* **2010**, *20*, 5167-5173.

(6) Thangadurai, V.; Weppner, W. *Adv. Funct. Mater.* **2005**, *15*, 107-112.

(7) O'Callaghan, M. P.; Cussen, E. J. *Chem. Commun.*, **2007**, 2048-2050.

(8) Thangadurai, V.; Weppner, W. *J. Solid State Chem.* **2006**, *179*, 974-984.

(9) Narayanan, S.; Thangadurai, V. *J. Power Sources* **2011**, *196*, 8080-8090.

(10) Ramzy, A.; Thangadurai, V. *Appl. Mater. Interfaces* **2010**, *2*, 385-390.

(11) Phipps, A. M.; Hume, D. N. *J. Chem. Educ.* **1968**, *25*, 664.

(12) Narayanan, S.; Epp, V.; Wilkening, M.; Thangadurai, V. *RSC Adv.* **2012**, 2, 2553-2561.

Chapter 4

(1) Narayanan, S.; Thangadurai, V. *J. Power Sources* **2011**, *196*, 8080-8090.

(2) Narayanan, S.; Thangadurai, V. *ECS Trans.* **2011**, *35* (32), 125-131.

(3) Cussen, E. J. *Chem. Commun.* **2006**, 412-413.

(4) Awaka, J.; Kijima, N.; Hayakawa, H.; Akimoto, J. *J. Solid State Chem.* **2009**, *182*, 2046-2052.

(5) Thangadurai, V.; Weppner,W. *J. Am. Ceram. Soc.* **2005**, *88*, 411-418.

(6) Shannon, R. D. *Acta Cryst.* **1976**, *A32*, 751-767.

(7) Thangadurai, V.; Weppner, W. *J. Solid State Chem.* **2006**, *179*, 974-984.

(8) Wullen, L. V.; Echelmeyer, T.; Meyer, H. W.; Wilmer, D. *Phys. Chem. Chem. Phys.* **2007**, *9*, 3298–3303.

(9) O'Callaghan, M. P.; Powell, A. S.; Titman, J. J.; Chen, G. Z.; Cussen, E. J. *Chem. Mater.* **2008**, *20*, 2360-2369.

(10) Koch, B.; Vogel, M. *Solid State Nucl. Magn. Reson.* **2008**, *34*, 37- 43.

(11) Roof, I. P.; Smith, M. D.; Cussen, E. J.; Loye, H. C. *J. Solid State Chem*. **2009**, *182*, 295-300.

(12) Percival, J.; Kendrick, E.; Slater, P. *Solid State Ionics* **2008**, *179*, 1666-1669.

(13) O'Callaghan, M. P.; Cussen, E. J. *Chem. Commun.* **2007**, 2048-2050.

(14) Thangadurai, V.; Adams, S.; Weppner, W. *Chem. Mater.* **2004**, *16*, 2998-3006.

(15) Thangadurai, V.; Kaack, H.; Weppner, W. J. F. *J. Am. Ceram. Soc.* **2003**, *86*, 437-440.

(16) Thangadurai, V.; Weppner, W. *Adv. Funct. Mater.* **2005**, *15*, 107-112.

(17) Murugan, R.; Thangadurai, V.; Weppner, W. *Angew. Chem. Int. Ed.* **2007**, *46*, 7778-7781.

(18) Percival, J.; Kendrick, E.; Slater, P. *Mater. Res. Bull.* **2008**, *43*, 765-770.

(19) Cussen, E. J.; Yip, T. W. S.; O'Neill, G., O'Callaghan, M. P. *J. Solid State Chem.* **2011**, *184*, 470-475.

Chapter 5

(1) Thangadurai, V.; Weppner, W. *J. Am. Ceram. Soc.* **2005**, *88*, 411-418.

(2) Thangadurai, V.; Weppner, W. *Adv. Funct. Mater.* **2005**, *15*, 107-112.

(3) Murugan, R.; Thangadurai, V.; Weppner, W. *Angew. Chem. Int. Ed.* **2007**, *46*, 7778-7781.

(4) O'Callaghan, M. P.; Cussen, E. J. *Chem. Commun.* **2007**, *20*, 2048-2050.

(5) Murugan, R.; Thangadurai, V. *Ionics* **2007**, *13*, 195-203.

(6) Murugan, R.; Thangadurai, V.; Weppner, W. *Appl. Phys. A* **2008**, *91*, 615-620.

(7) Ramzy, A.; Thangadurai, V. *Appl. Mater. Interfaces* **2010**, *2*, 385-390.

(8) Narayanan, S.; Epp, V.; Wilkening, M.; Thangadurai, V. *RSC Adv.* **2012**, 2, 2553-2561.

(9) Larson, A. C.; Von Dreele, R. B. *General Structure Analysis System (GSAS), Los Alamos National Laboratory Report LAUR*, **1994**.

(10) Toby, B. H. *J. Appl. Crystallogr.* **2001,** *34*, 210-213.

(11) Cussen, E. J. *Chem. Commun.* **2006**, 412-413.

(12) Xie, H.; Alonso, J. A.; Li, Y.; Fernández-Díaz, M. T; Goodenough, J. B. *Chem. Mater.* **2011**, *23*, 3587-3589.

(13) Shannon, R. D. *Acta Cryst.* **1976**, *A32*, 751-767.

(14) O'Callaghan, M. P.; Lynham, D. R.; Cussen, E. J.; Chen, G. Z. *Chem. Mater.* **2006**, *18*, 4681-4689.

(15) Brown, I. D.; Altermatt, D. *Acta Crystallogr. B* **1985,** *41*, 244-247.

(16) Geiger, C. A.; Alekseev, E.; Lazic, B.; Fisch, M.; Armbruster, T.; Langner, R.; Fechtelkord, M.; Kim, N.; Pettke, T.; Weppner, W. *Inorg. Chem.* **2011**, *50*, 1089-1097.

(17) O'Dell, L. A., Savin, S. L. P.; Chadwick, A. V.; Smith, M. E. *Solid State Nucl. Magn. Res.* **2007**, *31*, 169-173.

(18) Koch, B.; Vogel, M. *Solid State Nucl. Magn. Reson.* **2008**, *34*, 37-43.

(19) O'Callaghan, M. P.; Cussen, E. J. *Solid State Sci.* **2008**, *10*, 390-395.

(20) Narayanan, S.; Thangadurai, V. *J. Power Sources* **2011**, *196*, 8085-8090.

(21) Ramzy, A.; Thangadurai, V. *Appl. Mater. Interfaces* **2010**, *2*, 385-390.

(22) Wullen, L. V.; Echelmeyer, T.; Meyer, H. W.; Wilmer, D. *Phys. Chem. Chem. Phys.* **2007**, *9*, 3298-3303.

(23) Wang, W.; Wang, X. -P.; Gao, Y. -X.; Yang, J. -F.; Fang, Q. -F. *Front. Mater. Sci. China* **2010**, *4*, 189-192.

(24) Li, Q.; Thangadurai, V. *Fuel Cells* **2009**, *9*, 684-698.

(25) Thangadurai, V.; Kaack, H.; Weppner, W. *J. Am. Ceram. Soc.* **2003**, *86*, 437-440.

(26) Irvine, J. T. S.; Sinclair, D. C.; West, A. R. *Adv. Mater.* **1990**, *2*, 132-138.

(27) Kuhn, A.; Narayanan, S.; Spencer, L.; Goward, G.; Thangadurai, V.; Wilkening, M. *Phy. Rev. B* **2011**, *83*, 094302-1-11.

(28) Almond, D. P.; Duncan, G. K.; West, A. R. *Solid State Ionics* **1983**, *8*, 159-164.

(29) París, M. A.; Sanz, J. *Chem. Mater.* **2000**, *12*, 1694-1701.

(30) Jonscher, A. K. *Nature* **1977**, *267*, 673-679.

(31) Jonscher, A. K. *Dielectric Relaxation in Solids*, Chelsea Dielectric Press: London, **1983**.

(32) Hodge, I. M.; Ingram, M. D.; West, A. R. *J. Amer. Ceram. Soc*. **1976**, *59*, 360-366.

(33) Thangadurai, V.; Adams, S.; Weppner, W. *Chem. Mater.* **2004**, *16*, 2998-3006.

(34) Truong, L.; Thangadurai, V. *Chem. Mater.* **2011**, *23*, 3970-3977.

Chapter 6

(1) Narayanan, S.; Epp, V.; Wilkening, M.; Thangadurai, V. *RSC Adv.* **2012**, *2*, 2553-2561.

(2) Percival, J.; Slater, P. R. *Solid State Commun.* **2007**, *142*, 355-357.

(3) Cussen, E. J. *J. Mater. Chem.* **2010**, *20*, 5167-5173.

(4) Thangadurai, V.; Weppner, W. *Adv. Funct. Mater.* **2005**, *15*, 107-112.

(5) O'Callaghan, M. P.; Cussen, E. J. *Chem. Commun.* **2007**, 2048-2050.

(6) Narayanan, S.; Thangadurai, V. *J. Power Sources* **2011**, *196*, 8085-8090.

(7) Ramzy, A.; Thangadurai, V. *Appl. Mater. Interfaces* **2010**, *2*, 385-390.

(8) Thangadurai, V.; Weppner, W. *J. Solid State Chem.* **2006**, *179*, 974-984.

(9) Percival, J.; Kendrick, E.; Slater, P. *Solid State Ionics* **2008**, *179*, 1666-1669.

(10) Cussen, E. J. *Chem. Commun.* **2006**, 412-413.

(11) Geiger, C. A.; Alekseev, E.; Lazic, B.; Fisch, M.; Armbruster, T.; Langner, R.; Fechtelkord, M.; Kim, N.; Pettke, T.; Weppner, W. *Inorg. Chem*. **2011**, *50*, 1089-1097.

(12) O'Dell, L. A., Savin, S. L. P.; Chadwick, A. V.; Smith, M. E. *Solid State Nucl. Magn. Res.* **2007**, *31*, 169-173.

(13) Li, Q.; Thangadurai, V. *Fuel Cells* **2009**, *9*, 684-698.

(14) Thangadurai, V.; Huggins, R. A.; Weppner, W. *J. Power Sources* **2002**, *108*, 64-69.

(15) Irvine, J. T. S.; Sinclair, D. C.; West, A. R. *Adv. Mater.* **1990**, *2*, 132-138.

(16) Jonscher, A. K. *Dielectric Relaxation in Solids*, Chelsea Dielectric Press: London, **1983**.

(17) Jonscher, A. K. *Nature* **1977**, *267*, 673-679.

(18) Mauritz, K. A. *Macromolecules* **1989**, *22*, 4483-4488.

(19) Pradhan, D. K.; Choudhary, R. N. P.; Samantaray, B. K. *Int. J. Electrochem. Sci.* **2008**, *3*, 597-608.

(20) París, M. A.; Sanz, J. *Chem. Mater*. **2000**, *12*, 1694-1701.

(21) Almond, D. P.; West, A. R.; Grant, R. J. *Solid State Commun.* **1982**, *44*, 1277-1280.

(22) Almond, D. P.; Duncan, G. K.; West, A. R. *Solid State Ionics* **1983**, *8*, 159-164.

(23) Hodge, I. M.; Ingram, M. D.; West, A. R. *J. Am. Ceram. Soc*. **1976**, *59*, 360-366.

(24) Thangadurai, V.; Kaack, H.; Weppner, W. *J. Am. Ceram. Soc.* **2003**, *86*, 437-440.

(25) Murugan, R.; Thangadurai, V.; Weppner, W. *Angew. Chem. Int. Ed.* **2007**, *46*, 7778-7781.

(26) Kim, K.; Iriyama, Y.; Yamamoto, K.; Kumazaki, S.; Asaka, T.; Tanabe, K.; Fisher, C. A. J.; Hirayama, T.; Murugan, R.; Ogumi, Z. *J. Power Sources* **2011**, *196*, 764-767.

(27) Kotobuki, M.; Munakata, H.; Kanamura, K.; Sato, Y.; Yoshida, T. *J. Electrochem. Soc*. **2010**, *157*, A1076-A1079.

(28) Ohta, S.; Kobayashi, T.; Asaoka, T. *J. Power Sources* **2011**, *196*, 3342-3345.

(29) Shimonishi, Y.; Toda, A.; Zhang, T.; Hirano, A.; Imanishi, N.; Yamamoto, O.; Takeda, Y. *Solid State Ionics* **2011**, *183*, 48-53.

(30) Jin, Y.; McGinn, P. J. *J. Power Sources* **2011**, *196*, 8683-8687.

(31) Kuhn, A.; Narayanan, S.; Spencer, L.; Goward, G.; Thangadurai, V.; Wilkening, M. *Phy. Rev. B* **2011**, *83*, 094302-1-11.

(32) Wilkening, M.; Epp, V.; Feldhoff, A.; Heitjans, P. *J. Phys. Chem.* C **2008**, *112*, 9291-9300.

(33) Koch B.; Vogel, M. *Solid State Nucl. Magn. Reson.* **2008**, *34*, 37-43.

(34) Hendrickson, J.; Bray, P. *J. Magn. Res.* **1973**, *9*, 341-357.

(35) Wilkening, M.; Bork, D.; Indris, S.; Heitjans, P. *Phys. Chem. Chem. Phys.* **2002**, *4*, 3246-3251.

(36) Epp, V.; Wilkening, M. *Phys. Rev. B* **2010**, *82*, 020301-1-4.

(37) Kuhn, A.; Sreeraj, P.; Pöttgen, R.; Wiemhöfer, H. -D.; Wilkening, M.; Heitjans, P. *J. Am. Chem. Soc.* **2011**, *133*, 11018-11021.

Appendix A: Indexed powder XRD patterns of $Li_5La_3Nb_{2-x}Y_xO_{12-\delta}$

Table A. 1 Indexed powder XRD patterns of $Li_5La_3Nb_{2-x}Y_xO_{12-\delta}$ (x = 0.15; 0.2).

			x = 0.15			x = 0.2		
h	*k*	*l*	$d_{obs.}$ (Å)	$d_{cal.}$ (Å)	$I_{obs.}$ (%)	$d_{obs.}$ (Å)	$d_{cal.}$ (Å)	$I_{obs.}$ (%)
2	1	1	5.169	5.198	100	5.175	5.203	100
2	2	0	4.480	4.502	18	4.490	4.506	20
3	2	1	3.398	3.403	61	3.401	3.406	69
4	0	0	3.182	3.183	48	3.184	3.186	48
4	2	0	2.849	2.847	87	2.850	2.850	88
3	3	2	2.717	2.715	7	2.714	2.717	6
4	2	2	2.602	2.599	58	2.604	2.601	69
5	2	1	2.327	2.325	33	2.502	2.499	4
6	1	1	2.072	2.066	35	2.331	2.327	39
5	4	0	2.020	1.989	4	2.073	2.067	55
6	3	1	1.885	1.877	6	2.017	1.990	5
4	4	4	1.843	1.819	6	1.885	1.879	8
7	2	0	1.772	1.749	18	1.848	1.839	7
7	2	1	1.739	1.733	15	1.772	1.750	22
7	2	2	1.708	1.686	41	1.740	1.734	16
6	5	1	1.622	1.617	10	1.710	1.688	43
7	4	0	1.599	1.579	9	1.624	1.618	11
6	5	3	1.529	1.522	4	1.599	1.581	11

7	5	2	-	-	-	1.449	1.443	4
9	0	0	1.431	1.415	10	1.430	1.416	10
7	6	0	1.396	1.381	11	-	-	-
8	4	2	-	-	-	1.395	1.382	10
7	6	1	1.380	1.373	6	1.381	1.374	5
8	5	0	1.363	1.350	7	1.365	1.351	9
9	3	2	1.320	1.313	5	1.321	1.314	7
10	3	1	1.220	1.214	6	1.222	1.215	7
			a =12.733(9) Å			*a* = 12.747(7) Å		

Table A. 2 Indexed powder XRD patterns of $Li_5La_3Nb_{2-x}Y_xO_{12-\delta}$ (x = 0.25).

			x = 0.25		
h	*k*	*l*	$d_{obs.}$ (Å)	$d_{cal.}$ (Å)	$I_{obs.}$ (%)
2	1	1	5.137	5.192	91
2	2	0	4.458	4.496	19
2	2	2	3.736	3.671	4
3	2	1	3.386	3.399	85
4	0	0	3.173	3.179	62
4	2	0	2.838	2.844	100
3	3	2	2.654	2.711	8
4	2	2	2.594	2.596	84
5	2	1	2.325	2.322	49

6	1	1	2.067	2.063	46
6	2	0	2.015	2.011	6
6	3	1	1.881	1.875	9
4	4	4	1.842	1.836	8
6	4	0	1.770	1.781	30
7	2	1	1.737	1.747	22
6	4	2	1.706	1.699	57
6	5	1	1.622	1.628	13
8	0	0	1.596	1.590	16
8	2	0	1.538	1.542	3
8	2	1	1.528	1.531	4
8	3	2	1.447	1.449	3
7	5	2	1.429	1.440	13
8	4	2	1.395	1.396	13
7	6	0	1.378	1.379	7
7	6	1	1.363	1.371	9
8	5	2	1.319	1.319	7
10	1	0	1.267	1.272	3
10	3	0	1.219	1.224	6

a =12.728(4) Å

Appendix B: Indexed powder XRD patterns of $Li_{5+2x}La_3Nb_{2-x}Y_xO_{12}$

Table B. 1 Indexed powder XRD patterns of $Li_{5+2x}La_3Nb_{2-x}Y_xO_{12}$ (x = 0.20 and 0.25) using *PROSZKI* program.

			x = 0.20			x = 0.25		
h	*k*	*l*	$d_{obs.}$ (Å)	$d_{cal.}$ (Å)	$I_{obs.}$ (%)	$d_{obs.}$ (Å)	$d_{cal.}$ (Å)	$I_{obs.}$ (%)
2	1	1	5.196	5.216	100	5.151	5.195	86
2	2	0	4.503	4.517	19	4.469	4.499	15
3	2	1	3.411	3.415	79	3.392	3.401	76
4	0	0	3.190	3.194	58	3.173	3.181	65
4	2	0	2.856	2.857	93	2.842	2.845	100
3	3	2	2.724	2.724	7	2.712	2.713	8
4	2	2	2.609	2.608	86	2.598	2.597	82
5	1	0	2.506	2.506	4	2.494	2.495	4
5	2	1	2.333	2.333	47	2.325	2.323	48
6	1	1	2.074	2.073	42	2.067	2.064	49
6	2	0	2.021	2.020	5	2.015	2.012	6
6	3	1	1.886	1.884	9	1.879	1.876	8
4	4	4	1.847	1.844	7	1.840	1.837	8
6	4	0	1.775	1.772	27	1.768	1.764	31
7	2	1	1.742	1.739	20	1.736	1.732	21
6	4	2	1.710	1.707	52	1.706	1.700	61
6	5	1	1.625	1.623	12	1.621	1.616	12
8	0	0	1.600	1.597	12	1.595	1.590	16

6	5	3	1.530	1.527	4	1.526	1.521	5
8	3	2	1.451	1.447	3	1.447	1.450	4
8	4	0	1.432	1.428	12	1.428	1.423	15
9	1	1	1.397	1.394	12	1.394	1.397	15
7	6	0	1.381	1.378	7	1.378	1.380	9
6	6	4	1.365	1.362	10	1.362	1.356	13
8	5	2	1.321	1.318	7	1.318	1.319	7
10	1	0	1.268	1.271	3	1.265	1.266	3
10	3	0	1.221	1.224	7	1.219	1.219	8
			12.776(4) Å			12.742(4) Å		

Table B. 2 Indexed powder XRD patterns of $Li_{5+2x}La_3Nb_{2-x}Y_xO_{12}$ (x = 0.50 and 0.75) using *PROSZKI* program.

			x = 0.50			x = 0.75		
h	*k*	*l*	$d_{obs.}$ (Å)	$d_{cal.}$ (Å)	$I_{obs.}$ (%)	$d_{obs.}$ (Å)	$d_{cal.}$ (Å)	$I_{obs.}$ (%)
2	1	1	5.196	5.223	100	5.181	5.220	93
2	2	0	4.503	4.523	16	4.503	4.521	16
3	2	1	3.418	3.419	88	3.418	3.417	86
4	0	0	3.195	3.198	61	3.201	3.196	59
4	2	0	2.864	2.860	97	2.865	2.859	100
3	3	2	2.728	2.727	10	2.732	2.726	8
4	2	2	2.616	2.611	96	2.620	2.610	84
5	1	0	2.513	2.509	5	2.520	2.508	5

5	2	1	2.342	2.336	54	2.345	2.334	50
6	1	1	2.081	2.075	51	2.083	2.074	42
6	2	0	2.030	2.023	6	2.045	2.025	7
6	3	0	1.894	1.886	10	1.896	1.906	8
4	4	4	1.854	1.847	9	1.856	1.846	8
6	4	0	1.781	1.774	29	1.783	1.790	24
7	2	1	1.749	1.757	22	1.749	1.756	19
6	4	2	1.717	1.710	73	1.722	1.709	55
6	5	1	1.633	1.638	14	1.637	1.637	11
8	0	0	1.607	1.599	15	1.608	1.598	13
6	5	3	1.537	1.540	6	1.538	1.539	5
8	3	2	1.457	1.458	5	1.458	1.457	5
8	4	0	1.439	1.430	16	1.443	1.448	13
9	1	1	1.404	1.404	18	1.407	1.403	14
7	6	0	1.387	1.388	8	1.389	1.387	8
6	6	4	1.371	1.364	12	1.375	1.379	9
8	5	2	1.327	1.327	8	1.329	1.326	6
10	1	0	1.275	1.273	4	1.279	1.279	3
10	3	0	1.227	1.225	8	1.230	1.230	7
			12.793(4) Å			12.809(4) Å		